Georg Winkler, BSc

Interaction effects on quantum wires with strong spin-orbit coupling

MASTER THESIS

For obtaining the academic degree
Diplom-Ingenieur

Master Programme of
Technical Physics

Graz University of Technology

Supervisor:
Ao. Univ.-Prof. Dipl.-Phys. Dr .rer .nat. Hans Gerd Evertz
Institute of Theoretical and Computational Physics

Graz, April 2014

to Alina

Abstract

Quantum wires with Rashba spin-orbit coupling and an external magnetic field exhibit a gap in one-half of the conducting modes. The other half of the modes remains gapless with a helical spin order - opposite Fermi points have opposite spin directions. Thus the system provides a spin filter. This type of system is often researched using Luttinger liquid theory, therefore lacking connections to microscopic models. DMRG studies are used as a benchmark for the validity of the Luttinger liquid description in interacting systems. Spectral densities, calculated from the real-time evolution, indicate that the helical spin order is preserved under interactions. The Luttinger liquid coefficients are extracted from correlation functions for distinguishing between the different phases of the system and obtaining phase diagrams. Breather bound states, which are predicted by the Luttinger liquid theory, are observed and the results are compared to field theoretical calculations.

Kurzfassung

Quantendrähte mit Rashba Spin-Bahn-Kopplung und einem externen magnetischen Feld weisen eine Bandlücke in einer Hälfte der zum Ladungstransport beitragenden Moden auf. Die andere Hälfte der Moden hat keine Lücke und dafür eine helikale Spinordnung - gegenüberliegende Fermipunkte weisen entgegengesetzte Spinrichtungen auf. Als direkte Folge hat das System die Eigenschaften eines Spinfilters. Diese Art von Systemen wird sehr oft im Rahmen der Theorie der Luttingerflüssigkeit behandelt, der es an Verbindung zu mikroskopischen Modellen fehlt. Mithilfe von DMRG Studien wird die Gültigkeit des Luttingerflüssigkeitsbildes in wechselwirkenden Systemen untersucht. Spektraldichten werden aus der Realzeitentwicklung des Systems bestimmt. Mit deren Hilfe können wir zeigen, dass die helikale Spinordnung im wechselwirkenden System bestehen bleibt. Die Luttingerflüssigkeitskoeffizienten werden aus den Korrelationsfunktionen extrahiert und mit deren Hilfe Phasendiagramme des Systems angefertigt. Gebundene Zustände, sogenannte Breather, welche von der Luttingerflüssigkeitstheorie vorhergesagt wurden, werden beobachtet und die Ergebnisse werden mit feldtheoretischen Berechnungen verglichen.

Contents

Chapter 1

Introduction

The development of quantum mechanics, in the beginning of the 20th century, induced not only a profound paradigm change in our understanding of the world, but also caused among others an industrial revolution that rocketed us into the 21st century. Finally, a satisfactory theory of electrons, and thus electricity, was available and it took not long until this new knowledge was put to work in the devices that lie on the foundation of our modern day electronics: the transistor and the diode.

Apart from very rare occasions, like hard disk drives, present day electronics makes use of only the charge degrees of freedom of the electron. However, during the early stages of quantum mechanics scientists soon realized that the electron also has an intrinsic magnetic moment, which was then called spin. This additional spin degrees of freedom have much shorter relaxation times and they can carry additional information. Therefore, it is a very alluring prospect to make use of them in future solid-state devices. This emerging technology, exploiting the intrinsic spin of the electron, has been named spintronics. Spintronics could be much faster and at the same time also extremely energy efficient compared to present day electronics. It is one of the technologies extensively studied, to enable the perpetual growth of computing power last past the year 2025.

The spin of the electron can be manipulated by magnetic fields, which is a little bit unpractical for the application in spintronic devices. We already have profound knowledge on how to use electrical fields for controlling the electronic state in present day electronics. As soon as a relativistic theory of the electron was available, it turned out that the spin also couples to the movement of the electron inside an electrical field. This so-called spin-orbit coupling is not only important for the understanding of many solids, but also plays a big role in proposed spintronic devices. It allows the electron spin to be manipulated by electrical fields. Therefore, understanding the physics of systems with spin-orbit coupling is of fundamental importance for future spintronic devices.

After the foundations of quantum mechanics had been set, it soon turned out that the exact solution for realistic systems, containing more than a few particles, is in most cases impossible. The number of degrees of freedom, which grows exponentially with the system size, is simply too large for our present day computers. Fortunately, approximative schemes, that can give results in the thermodynamic limit, are applicable for many systems. For those where they aren't, we are limited to experimental techniques or very small system sizes. Usually, the electronic correlation is in some way disregarded in these approximative techniques. However, correlations are one of the cornerstones of quantum mechanics and the

scale of present day electronic devices is already on the threshold where quantum mechanical correlations play a crucial role. Understanding the physics of such systems is of profound importance for the devices of the future.

The simulation of strongly correlated systems is one of the most demanding challenges in physics. Some of the most efficient algorithms have been developed for this task, like Quantum Monte Carlo methods (QMC), or especially for one-dimensional systems, the Density Matrix Renormalization Group (DMRG). Especially DMRG is the method of choice for numerically exact solutions of one-dimensional many-body systems on the verge to the thermodynamic limit. Problems with a few hundred interacting electrons are easily doable for the toy models that are gladly researched in this area.

Apart from ground state properties, the dynamics of one-dimensional quantum systems can be simulated with high efficiency in the same framework as DMRG. By looking at the time evolution after a simple excitation in the ground state of the system, one can learn nearly everything about the physical properties of the system, even away from the ground state.

Besides the numerical approach to the problem of strongly correlated systems, analytical techniques exist. The low energy properties of many one-dimensional systems have their fixed point in Tomonaga-Luttinger liquids, a class of models that can be exactly solved. During the translation of a model into the language of Luttinger liquids most of the original information is lost. It was only during the last two decades that our numerical methods, and the neccessary computing power, are sufficiently advanced to allow direct comparisons between numerical results and field theoretical Luttinger liquid calculations. The Luttinger liquid theory makes many important predictions of phenomena in one-dimensional systems. Finding the corresponding microscopic parameters of a model, that correspond to a certain Luttinger liquid, by comparisons to numerical calculations is mandatory for possible real-life applicatons.

In this work we investigate the combined effect of strong spin-orbit coupling and a weak external magnetic field on one dimensional quantum wires. It is well known what happens in the noninteracting case, especially the opening of a spin-orbit gap is of interest for possible applications in spintronic devices. However, interacting results are so far only available from the Luttinger liquid theory. We complement these results by DMRG ground state calculations and dynamical correlation functions obtained from time evolutions. The applicability of the Luttinger liquid picture are tested and its boundaries determined.

Chapter 2

The model and some theoretical background

2.1 Hamiltonian and non-interacting dispersions

The one-dimensional Hubbard model is one of the simplest models available for studying interaction effects in chains or quasi one-dimensional systems. We will use a generalisation of this model, an extended Hubbard model with an additional spin-orbit coupling and an external magnetic field. The extended Hubbard model adds nearest neighbour interactions to the system and resembles therefore a somewhat more realistic interaction. In contrast to the extended Hubbard model the 1-d Hubbard model can be solved exactly by the Bethe ansatz. The Hamiltonian, we are going to use in our work, is given below:

$$\left.\begin{aligned} H_{\mathrm{t}} &= -\sum_j \frac{t}{2}(c_j^\dagger c_{j+1} + h.c.) - (\mu - t)c_j^\dagger c_j \\ H_{\mathrm{SO}} &= -\sum_j \frac{\alpha}{2}(ic_j^\dagger \sigma^y c_{j+1} + h.c.) \\ H_{\mathrm{B}} &= \sum_j B c_j^\dagger \sigma^z c_j \end{aligned}\right\} H_0$$
$$\left.\begin{aligned} H_{\mathrm{int}} &= \sum_j [U n_{j\uparrow} n_{j\downarrow} + U' n_j n_{j+1}] \end{aligned}\right\} H_1 \tag{2.1}$$

Note that we assume implicit summation over the spin index if it is not explicitly given. The extended Hubbard model is given by the first and last line of equation (2.1) as the sum of the kinetic energy and the interaction $H_{\mathrm{ext.H.}} = H_{\mathrm{t}} + H_{\mathrm{int}}$. Albeit the extended Hubbard model cannot be solved it has already been studied very thoroughly with various numerical and approximative analytical techniques. We supplement this model with an additional magnetic field H_{B} (here only taking into account the Zeeman splitting) and the spin-orbit coupling H_{SO}. The magnetic field can be controlled relatively easy externally by the experimentators. The origin of the spin-orbit coupling is more subtle and its strength α depends strongly on the chosen material. Suitable materials with a very strong spin-orbit coupling are e.g. GaAs/AlGaAs hole quantum wires where the effect of a spin-orbit gap has been confirmed [28].

When nothing else is said we will always set $\hbar = 1$, $m = 1$ and $e = 1$. Furthermore we will always assume the hopping $t = 1$ and therefore all other parameters of the Hamiltonian are given as multiples of t. By setting t as our energy unit, we automatically set the unit of time as $\left[\frac{1}{t}\right]$.

2.1.1 Origin of the spin-orbit coupling

The spin-orbit coupling is a strictly relativistic effect. Therefore, the non-relativistic Schrödinger equation is not suitable for its derivation. It follows directly from the relativistic Dirac equation as a second order $\mathcal{O}(\frac{v^2}{c^2})$ effect. The spin-orbit Hamiltonian can be derived by an expansion in $\frac{v}{c}$ of the Dirac equation with an applied external electromagnetic field. The derivation will not be given here, it can be found in e.g. [3]. In the general three dimensional case the spin-orbit Hamiltonian (in SI-units) reads:

$$H_{\mathrm{SO}}^{\mathrm{3D}} = -\frac{e\hbar}{4m^2c^2}\boldsymbol{\sigma} \cdot [\mathbf{E} \times (\mathbf{p} - \frac{e}{c}\mathbf{A})] \tag{2.2}$$

We are going to assume always the limit of small magnetic fields $\mathbf{p} - \frac{e}{c}\mathbf{A} \approx \mathbf{p}$. Furthermore the direction of movement is restricted to one dimension (e.g. the x-axis) $\mathbf{p} = (p, 0, 0)$. Then the spin-orbit Hamiltonian reads as

$$H_{\mathrm{SO}}^{\mathrm{1D}} = (\frac{\hbar\alpha_z}{m}\sigma_z - \frac{\hbar\alpha_y}{m}\sigma_y)p, \tag{2.3}$$

with the spin-orbit coupling parameters

$$\alpha_y = \frac{4mc^2}{e}E_y \quad \text{and} \quad \alpha_z = \frac{4mc^2}{e}E_z. \tag{2.4}$$

Here α_y and α_z are assumed to be constant on the x-Axis. This is called Rashba spin-orbit coupling [29]. Assuming $\alpha_z = 0$ and using the same arguments as deriving the tight binding kinetic energy one arrives at the Rashba spin-orbit Hamiltonian H_{SO} given in equation (2.1). The additional factor $\frac{1}{2}$ has solely "cosmetic" reasons concerning the dispersion relations.

2.1.2 Diagonalisation of the non-interacting Hamiltonian

Without the magnetic field B the non-interacting Hamiltonian can be transformed to a tight-binding model with a Peierls Phase, by going from the z-Basis ($\uparrow\downarrow$) to the y-Basis ($\rightarrow\leftarrow$) using the transformations:

$$c_{j\rightarrow}^\dagger = \frac{1}{\sqrt{2}}(c_{j\uparrow}^\dagger + ic_{j\downarrow}^\dagger) \quad \text{and} \quad c_{j\leftarrow}^\dagger = \frac{1}{\sqrt{2}}(c_{j\uparrow}^\dagger - ic_{j\downarrow}^\dagger). \tag{2.5}$$

Plugging these transformations into the non-interacting Hamiltonian yields

$$\begin{aligned} H_0 = \sum_j [&(-\frac{t}{2} - i\frac{\alpha}{2})c_{j\rightarrow}^\dagger c_{j+1\rightarrow} + (-\frac{t}{2} + i\frac{\alpha}{2})c_{j+1\rightarrow}^\dagger c_{j\rightarrow} - (\mu - t)c_{j\rightarrow}^\dagger c_{j\rightarrow} + \\ &(-\frac{t}{2} + i\frac{\alpha}{2})c_{j\leftarrow}^\dagger c_{j+1\leftarrow} + (-\frac{t}{2} - i\frac{\alpha}{2})c_{j+1\leftarrow}^\dagger c_{j\leftarrow} - (\mu - t)c_{j\leftarrow}^\dagger c_{j\leftarrow} + \\ &B(c_{j\rightarrow}^\dagger c_{j\leftarrow} + c_{j\leftarrow}^\dagger c_{j\rightarrow})]. \end{aligned} \tag{2.6}$$

In this basis the spin-orbit coupling becomes a simple nearest-neighbour hopping with a complex amplitude $\pm i\frac{\alpha}{2}$. This hopping preserves the spin in $\hat{S}^y$ direction as a good quantum number. Therefore, we call the $\hat{S}^y$ direction the good quantization axis for the spin-orbit coupling. Note that the hopping amplitude is now complex and that it is the complex conjugate for the other spin directon. Therefore, the hopping can be also written as $-\frac{t}{2}\exp(i\sigma_y k_{\mathrm{SO}})$, where we introduced the spin-orbit momentum

$$k_{\mathrm{SO}} = \arctan\frac{\alpha}{t}, \tag{2.7}$$

and $\sigma_y = 1$ for the spin-$\rightarrow$ electrons and $\sigma_y = -1$ for the spin-$\leftarrow$ electrons. k_{SO} takes the place of a spin dependent Peierls phase. Although, this transformation has diagonalized the spin subspace for the spin-orbit coupling, it "broke" the magnetic field term. This becomes a hopping between the different spin directions $\leftarrow$ and $\rightarrow$. The "good quantization axis" for the magnetic field term is the $\hat{S}^z$ direction.

The Hamiltonian can be diagonalized straightforward by going to momentum space with the transformation $c^\dagger_{j\sigma} = \frac{1}{\sqrt{L}}\sum_k \exp(-ikj)a^\dagger_{k\sigma}$. It can be written compactly using the spinor $\psi^\dagger_k = (a^\dagger_{k\rightarrow},\ a^\dagger_{k\leftarrow})$

$$\begin{aligned} H_0 &= \sum_k \begin{pmatrix} a^\dagger_{k\rightarrow} & a^\dagger_{k\leftarrow} \end{pmatrix} \begin{pmatrix} \bar{\epsilon}(k+k_{\mathrm{SO}}) & B \\ B & \bar{\epsilon}(k-k_{\mathrm{SO}}) \end{pmatrix} \begin{pmatrix} a_{k\rightarrow} \\ a_{k\leftarrow} \end{pmatrix} \\ \bar{\epsilon}(k) &= -\sqrt{t^2+\alpha^2}\cos(k) - (\mu - t), \qquad k_{\mathrm{SO}} = \arctan(\frac{\alpha}{t}). \end{aligned} \tag{2.8}$$

Because of the magnetic field a final diagonalisation in the ($\rightarrow\leftarrow$) spin subspace is still to be done. The k-dependece of this transformation is nontrivial, hence the result can't be written in a very compact form and is not given here. We rather used a numerical diagonalisation of this 2×2 matrix if necessary.

We will now investigate the non-interacting dispersion relations. Because of the 2×2 matrix we will get two branches, one for each spin direction. However, the two orthogonal spin directions, residing on each branch, will be k-dependent. They take values between eigenstates of $\hat{S}^y$ and $\hat{S}^z$ and always have a zero expectation value in $\hat{S}^x$.

Figure 2.1 (a) shows the well known case of an applied magnetic field but no spin-orbit coupling. We see two braches separated in energy because of the Zeeman splitting with spin directions $\uparrow$ and $\downarrow$. Each branch is the usual cosine dispersion relation well known for the tight binding model.

Figure 2.1 (b) shows the case with applied spin-orbit coupling but no magnetic field. We know from equation (2.6) that the spin-orbit coupling can be interpreted as a spin dependent Peierls phase. Therefore each spin direction gets shifted to the left or right by k_{SO}, depending on the spin eigenstate of $\hat{S}^y$. The two branches are now separated in momentum and not in energy like before. The two orthogonal spin directions are the eigenstates of the $\hat{S}^y$ operator: $\rightarrow$ and $\leftarrow$.

Finally the effect of the combined spin-orbit coupling and magnetic field is shown in figure 2.1 (c). We keep the magnetic field small compared to the spin-orbit coupling $B \ll \alpha$. Therefore its effect is also kept relatively small and the spin-orbit coupling still dominates. One can still recognize the two shifted cosines with nearly the same spin directions as in 2.1 (b). However, at $k = 0$ and $k = \pm\pi$, where the two branches intersected before, a gap opens up. This is the so called spin-orbit gap. It is only a partial gap, or pseudogap, since

there are still ungapped modes left. From equation (2.6) we can see that the magnetic field introduces a hopping between $\rightarrow$ and $\leftarrow$ electrons. This leads to an avoided crossing at the former crossing points in the dispersion relation. It is important that the magnetic field has a component orhtogonal to the spin-orbit coupling for a gap to open up.

2.1.3 Properties of the dispersion relations

Due to the interplay between the spin-orbit coupling and the magnetic field the dispersion relation has some unusual properties. We want to explain them now in detail.

First we will look in detail at case (c) from figure 2.1. The relevant part is magnified in figure 2.2. We can see again that the two branches for the spin $\rightarrow$ and spin $\leftarrow$ electrons are shifted by $\pm k_{\mathrm{SO}}$. These shifted bands are typical for spin-orbit coupling but the equation for k_{SO} depends on the specific model. For tight-binding we have $k_{\mathrm{SO}} = \arctan \frac{\alpha}{t}$ whereas in a continuum model one would find simply $k_{\mathrm{SO}} = \frac{\alpha}{t}$. The size of the gap that opens up at $k = 0$ is directly proportional to B in the non-interacting case

$$\Delta^{\mathrm{SO}} = B. \tag{2.9}$$

The system is only inside the spin-orbit gap if the Fermi momentum k_{F} is commensurate with the spin-orbit momentum shift k_{SO}

$$k_{\mathrm{F}} = 2k_{\mathrm{SO}}. \tag{2.10}$$

Inside the spin-orbit gap the system has 2 Fermi points. If above condition is violated too much the system will have 4 Fermi points. Therefore we expect 2 and 4 Fermi point phases with very different properties. Indeed it is known that the conductance of a one dimensional system is always a multiple of the conductance quant $G_0 = \frac{e^2}{h}$ (see e.g. [15]). Each channel contributes one conductance quant to the total conductance. Therefore a quantum wire in the 4 Fermi point phase has a conductance of $G = 2G_0$, one G_0 for each spin species. In the 2 Fermi point phase only one spin species is available reducing the conductance by a factor of 2. This has been verified in conductance measurements of GaAs/AlGaAs hole quantum wires [28].

Also note that inside the spin-orbit gap the relation between k_{F} and the filling is the same as for spinless fermions

$$k_{\mathrm{F}} = n\pi. \tag{2.11}$$

This is because in both cases there is only one species of electrons below the Fermi level. This single branch is filled up until the Fermi level, its special shape has no influence on (2.11). This property will still hold under interactions.

Looking at the two opposite Fermi points inside the spin-orbit gap we see that they have orthogonal spin directions. Therefore the conductivity will be strongly spin-dependent at low energies respectively temperatures. The right Fermi point is a spin $\leftarrow$ eigenstate with a positive velocity $v_{\mathrm{F}} = \frac{\partial \epsilon(k)}{\partial k}|_{k=k_{\mathrm{F}}}$ and the left Fermi point is a spin $\rightarrow$ eigenstate with a negative velocity $-v_{\mathrm{F}} = \frac{\partial \epsilon(k)}{\partial k}|_{k=-k_{\mathrm{F}}}$. Therefore a right moving current can only contain spin $\leftarrow$ electrons and a left moving current only spin $\rightarrow$ electrons. This spin-dependent transport properties make the system interesting for applications in spintronics. Various devices using spin-orbit coupling have been proposed such as spinfilters [37] or Cooper pair splitters [30].

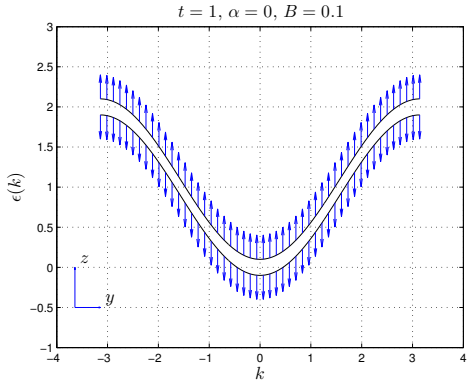

(a)

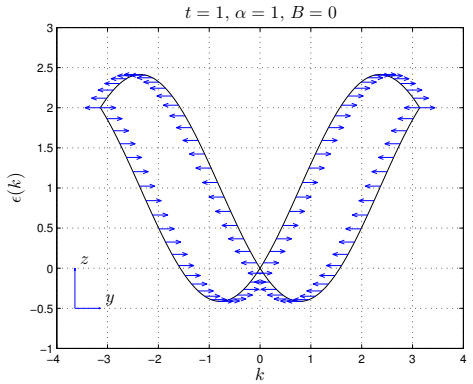

(b)

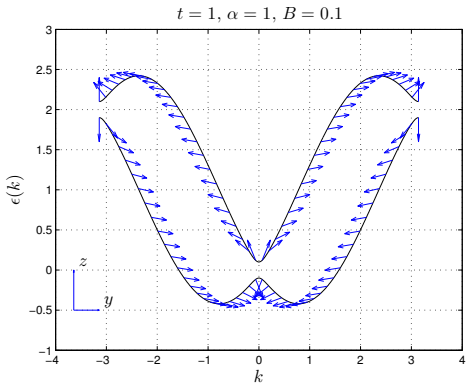

(c)

Figure 2.1: Dispersion relations calculated from equation (2.8). The upmost panel (a) shows a tight-binding model plus magnetic field. The spin degeneracy is lifted and the tight-binding band splits into two with spin directions parallel and antiparallel to the magnetic field. The middle panel (b) shows a tight-binding model plus spin-orbit coupling. Like before the spin degeneracy is lifted, but now the branches are separated in momentum k and the spin directions are parallel and antiparallel to the spin-orbit coupling. The lowest panel (c) shows the combined effect of spin-orbit coupling and magnetic field. A gap opens up at the former intersection points of the two branches.

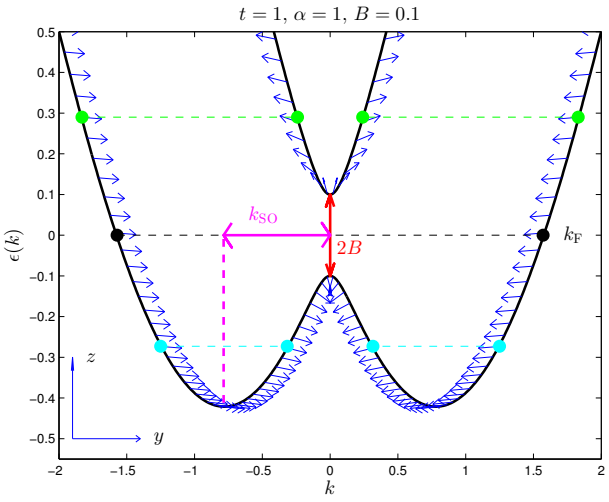

Figure 2.2: The spin-orbit gap in detail

2.1.4 Adding a cooper pairing field

An interesting addition to the Hamiltonian in equation (2.1) is an additional Cooper-pairing field Δ^{C}:

$$H_{\mathrm{C}} = \sum_j \Delta^{\mathrm{C}}(c_{j\uparrow}c_{j\downarrow} + h.c.). \tag{2.12}$$

This Hamiltonian gained a lot of attention recently because of the special topological properties and the appearance of Majorana bound states [31] [25] [36].

The noninteracting system can be solved by the same methods as before. Going to momentum space $c^\dagger_{j\sigma} = \frac{1}{\sqrt{L}}\sum_k \exp(-ikj)a^\dagger_{k\sigma}$ the noninteracting Hamiltonian now reads

$$\begin{aligned} H_0 = \sum_k [&(\tilde{\epsilon}(k) + B)a^\dagger_{k\uparrow}a_{k\uparrow} + (\tilde{\epsilon}(k) - B)a^\dagger_{k\downarrow}a_{k\downarrow} + \\ &i\alpha\sin(k)(a^\dagger_{k\downarrow}a_{k\uparrow} - a^\dagger_{k\uparrow}a_{k\downarrow}) - \Delta^{\mathrm{c}}(a_{-k\downarrow}a_{k\uparrow} + a^\dagger_{k\uparrow}a^\dagger_{-k\downarrow})] \end{aligned} \tag{2.13}$$

using $\tilde{\epsilon}(k) = -t\cos(k) - (\mu - t)$. As before the system still needs a diagonalisation in the spin-space and additionally also in the particle-hole space. The reason for this is that the Cooper pairing field breaks the conservation of the total particle number. We rewrite the Hamiltonian using Nambu spinors $\psi^\dagger_k = (a^\dagger_{k\uparrow}, a^\dagger_{k\downarrow}, a_{-k\downarrow}, -a_{-k\uparrow})$, which provide a suitable basis for this problem [21]. The Hamiltonian can now be written as a quadratic form $H = \sum_{k>0}\psi^\dagger_k\mathcal{H}\psi_k$, with

$$\mathcal{H} = \begin{pmatrix} \tilde{\epsilon}(k) + B & -i\alpha\sin(k) & -\Delta & 0 \\ i\alpha\sin(k) & \tilde{\epsilon}(k) - B & 0 & -\Delta \\ -\Delta & 0 & -\tilde{\epsilon}(k) + B & i\alpha\sin(k) \\ 0 & -\Delta & -i\alpha\sin(k) & -\tilde{\epsilon}(k) - B \end{pmatrix}. \tag{2.14}$$

However, diagonalising in the spin- and electron-hole-space has a prize. The resulting matrix has size 4×4 and therefore the dispersion relation has now 4 different branches. The

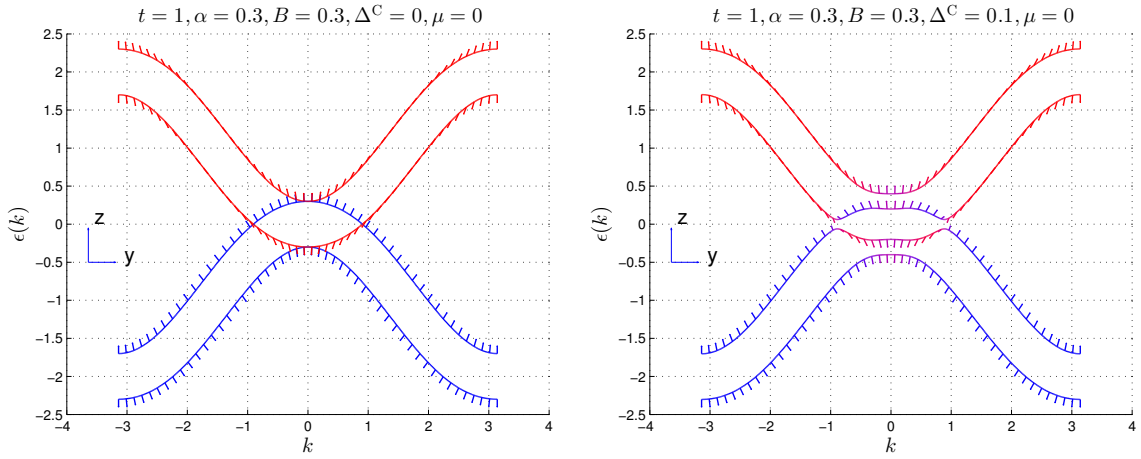

(a) (b)

Figure 2.3: Dispersion relations calculated from the matrix in equation (2.14). Because this is a 4×4 matrix the dispersion relation now has 4 different branches. The left panel (a) has a spin-orbit coupling and magnetic field of the same magnitude. The red lines are electron-like and the blue ones hole-like. The hole branches are simply the electron branches mirrored at μ. The right panel (b) has an additional Cooper-pairing field Δ^C. A gap opens up where the electron and hole branches meet at $\epsilon = \mu$.

dispersion relation with $\Delta = 0$ is plotted in fig 2.3 (a). We take the same parameters as Stoudenmire et al. in [36]. The red electron branch shows the same information as before. New is the blue hole branch, which is simply the electron branch mirrored around μ. The case with nonzero Cooper pairing field $\Delta^C = 0.1$ is shown in figure 2.3 (b). The effect of the Cooper pairing field is that it opens up a gap around the chemical potential μ. The pairing field in equation (2.12) describes a hopping between particle and hole states. Whenever the particle and hole dispersions crossed fomerly, the hopping causes an avoided crossing. As a side effect, particle and hole states begin to merge and the character of the branches are now mixed particle-hole states.

If the system has a boundary to a topologically trivial phase, zero-energy modes known as Majorana edge states fermions appear there. They are of great interest because of their possible prospect for quantum computing.

2.2 Luttinger liquid description

In more than one dimension interacting fermions are successfully described by Landau's Fermi liquid theory. It assumes an one-to-one correspondence between the free particles of the non-interacting system and the so called quasiparticles of the interacting system. Although the quasiparticles have a finite lifetime they can be labelled by the same quantum numbers as the free electrons and therefore each quasiparticle can be directly related to a free electron.

It turns out that in one dimension the Fermi-liquid theory does not apply. As soon as the interaction is turned on the elementary excitations are collective, bosonic ones bearing no resemblance to the free electrons. Surprisingly, it turned out that if you rewrite the

Hamiltonian for a special class of systems, the Tomonaga-Luttinger liquids, in terms of these collective excitations, the Hamiltonian becomes quadratic and immediatly solvable. By doing this transformation, called bosonization, the interaction vanishes magically and one arrives by a free field theory. We won't go through the tedious process of bosonization here, for that we refer the reader to [15], but an intuitive explanation shall be given. A typical interaction is usually written like this

$$H_{\text{int}} = \int dx dx' V(x - x')\rho(x)\rho(x'). \tag{2.15}$$

The bosonization process shows that the elementary excitations in one dimension are collective density fluctuations, not quasiparticles. Equation (2.15) is already quadratic in the density but not in particle excitations $c^\dagger$ or c. Therefore, after rewriting it in density fluctuations, it still stays quadratic.

However, this method is limited to Tomonaga-Luttinger liquids, or we will refer to them as simply Luttinger liquids, with the limitations that come with them. The original Tomonaga-Luttinger model has a kinetic energy given by the Hamiltonian

$$H = \sum_{k;r=R,L} v_F(\epsilon_r k - k_F) c^\dagger_{r,k} c_{r,k}, \tag{2.16}$$

where $\epsilon_R = +1$ for the right going particles and $\epsilon_L = -1$ for the left going particles. This is only the kinetic energy part, the interaction part is taken from equation (2.15). For the dispersion relation of the kinetic energy Hamiltonian see figure 2.4 (a). We see that it is a strictly linear dispersion, which is the simplifying assumption one has to make, in order for the model to be solvable. The Hamiltonian given in equation (2.15) and (2.16) represents a low energy model for spinless fermions. The cosine dispersion relation of the spinless fermions is linearized around the Fermi points, which may or may not be a good approximation.

After going through the process of bosonization the full Hamiltonian has a form looking like this

$$H_{\text{LL}} = \frac{v}{2\pi} \int \mathrm{d}x [\frac{1}{K}(\nabla\phi)^2 + K(\nabla\theta)^2], \tag{2.17}$$

where we introduced the two bosonic fields ϕ and θ and the two Luttinger liquid parameters v and K. The fields are such that $\rho(x) = -\frac{\nabla\phi(x)}{\pi}$ measures the electron density fluctuations in the system and $\frac{\nabla\theta}{\pi}$ is canonically conjugate to ϕ. They have bosonic commutation relations

$$[\phi(x), \frac{\nabla\theta}{\pi}] = i\delta(x - x'). \tag{2.18}$$

The Luttinger liquid parameter v is simply the Fermi velocity, although it is renormalized from the value v_F in equation (2.16) due to the interactions. The second one K is the Luttinger liquid coefficient and it encodes (also) the interactions. This is a model for low energies and large system sizes only. All terms that are irrelevant in the renormalization group sense are thrown away. Therefore, only one parameter K encoding the interaction survives. Generally it holds that $K = 1$ in the non-interacting case, whereas $K > 1$ for attractive interactions and $K < 1$ for repulsive interactions. However, it is usually not possible to relate K in a simple way to the specific interaction. We will treat this problem later.

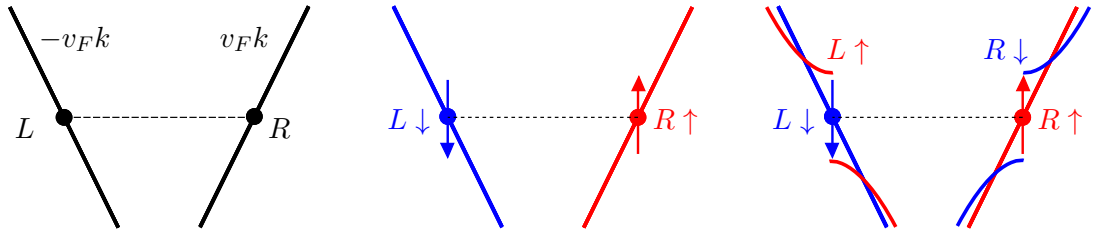

(a) Spinless Fermions (b) Helical LL (c) Spiral LL

Figure 2.4: Dispersion relations for the different Luttinger liquid models. Spin ↑ modes are marked red and spin ↓ modes blue.

Spinful Luttinger liquids can be described by the sum of two independent Hamiltonians looking exactly like in equation (2.17), one for the charge degrees of freedom and one for the spin degrees of freedom,

$$H = \sum_{\nu=\rho,\sigma} \frac{v_\nu}{2\pi} \int \mathrm{d}x [\frac{1}{K_\nu} (\nabla \phi_\nu)^2 + K_\nu (\nabla \theta_\nu)^2]. \tag{2.19}$$

This phenomenom is called spin-charge separation in one dimension. Each of these Hamiltonians has two parameters K_ρ and v_ρ for the charge Hamiltonian and K_σ and v_σ for the spin Hamiltonian. The statements for K above translate directly to K_ρ. Note also that $K_\rho = 0$ would indicate a charge gap, the system is then no Luttinger liquid anymore. For spin-isotropic or non-interacting systems we expect always $K_\sigma = 1$. Our model Hamiltonian is not isotropic and hence $K_\sigma \geq 1$. $K_\sigma < 1$ would indicate a spin gap.

Inside the spin-orbit gap, in the 2 Fermi point phase, our system bears a lot resemblances to spinless fermions. Each Fermi point has only one species (spin-direction) of particles available. Therefore, we expect to see some similarities here. However, Luttinger liquid physics has better models available and we will discuss them below. An overview and comparison of these different Luttinger liquids has also been given by Braunecker et al. [4].

2.2.1 Helical Luttinger liquid

Helical liqids appear at the edge of quantum spin Hall systems [43] [44] but they also give an approximative descripton of our system inside the 2 Fermi point phase. The key property of opposite spin directions at opposite Fermi points is incorporated into them, see the dispersion relation in figure 2.4 (b). They can be described by the same spinless fermions Hamiltonian, albeit with a different definition of the fields Φ and Θ,

$$\begin{aligned} H_{\mathrm{HLL}} &= \frac{v}{2\pi} \int \mathrm{d}x [\frac{1}{K_{\mathrm{HLL}}} (\nabla \Phi)^2 + K_{\mathrm{HLL}} (\nabla \Theta)^2], \\ \Phi &= \frac{\phi_{R\uparrow} + \phi_{L\downarrow}}{\sqrt{2}}, \ \Theta = \frac{\theta_{R\uparrow} - \theta_{L\downarrow}}{\sqrt{2}}, \end{aligned} \tag{2.20}$$

with $\phi_{R\uparrow}$ denoting the right-movers (which can only have spin ↑ in a helical liquid) and $\phi_{L\downarrow}$ the left-movers (with spin ↓). We already see that the spin index is obselete here because it is fixed by the direction of movement. That this is essentially the same Hamiltonian as spinless fermions underscores again the deep relation between our system and spinless fermions.

In helical liquids one species of electrons vanishes completely, like for spinless fermions. Real metals always have two spin directions and therefore at least two species of particles in them. Therefore the helical liquids can only appear as edge states, the bulk must have at least two species of particles.

2.2.2 Spiral Luttinger liquid

An even better low energy description of our system is given by the spiral Luttinger liquid. Originally it was invented for a different type of system: A Luttinger liquid with an embedded lattice of nuclear spins. The hyperfine interactions between the nuclear and the electron spins trigger a strong feedback reaction leading also to the opening of an partial gap (or pseudogap) like the spin-orbit gap [7] [6]. The nuclear spins adopt a spiral order causing a helical Overhauser magnetic field. This helical magnetic field is responsible for the opening of a gap in one half of the conduction modes.

The dispersion relation is illustrated in figure 2.4 (c). Like in the helical Luttinger liquid the spins have opposite spin directions at opposite Fermi points, but additionally the system has also gapped modes. Later, it turned out that the same low energy description can be applied to systems with strong spin-orbit coupling and an external magnetic field (and no nuclear spins) [5]. Indeed the two microscopic models are connected by a gauge transformation. Transforming the basis by

$$\psi(r) \to e^{i\sigma_y k_{\mathrm{SO}} r}\psi, \tag{2.21}$$

in our model, yields the model with the nuclear spins. However, strictly speaking this is only true if the commensurability condition for the Fermi momentum $k_{\mathrm{F}} = 2k_{\mathrm{SO}}$ is fullfilled. Then the Fermi level is exactly in the middle of the gap, which is always true for the other model. The model Hamiltonian can be written as

$$\begin{aligned} H_{\mathrm{SLL}} =& H_+ + H_- + H_{\mathrm{mix}}, \\ H_+ =& \frac{v_+}{2\pi}\int \mathrm{d}x[(\nabla\phi_+)^2 + (\nabla\theta_+)^2] + \frac{B_{\mathrm{eff}}}{a}\int \mathrm{d}x\cos(\sqrt{2K}\phi_+), \\ H_- =& \frac{v_-}{2\pi}\int \mathrm{d}x[(\nabla\phi_-)^2 + (\nabla\theta_-)^2], \\ H_{\mathrm{mix}} =& \frac{v_\rho - v_\sigma}{2\pi K}\sqrt{\frac{K_\rho}{K_\sigma}}\int \mathrm{d}x[(\nabla\theta_+)(\nabla\theta_-) - (\nabla\phi_+)(\nabla\phi_-)], \end{aligned} \tag{2.22}$$

with

$$\begin{aligned} v_+ &= (v_\rho K_\rho + v_\sigma K_\sigma^{-1})/K, \\ v_- &= (v_\rho K_\sigma^- 1 + v_\sigma K_\rho)/K, \end{aligned} \tag{2.23}$$

and

$$K = K_\rho + K_\sigma^{-1}. \tag{2.24}$$

The field B_{eff} in equation (2.22) represents the helical Overhauser magnetic field. The fields $\phi_\pm$ and $\theta_\pm$ are related to the charge and spin boson fields by

$$
\begin{aligned}
\phi_\sigma &= \frac{1}{\sqrt{K}}\left[K_\rho\phi_+ - \sqrt{\frac{K_\rho}{K_\sigma}}\phi_-\right],\\
\theta_\sigma &= \frac{1}{\sqrt{K}}\left[\frac{1}{K_\sigma}\phi_+ + \sqrt{\frac{K_\rho}{K_\sigma}}\phi_-\right],\\
\theta_\rho &= \frac{1}{\sqrt{K}}\left[\theta_+ - \frac{1}{\sqrt{K_\rho K_\sigma}}\theta_-\right],\\
\theta_\sigma &= \frac{1}{\sqrt{K}}\left[\theta_+ + \sqrt{K_\rho K_\sigma}\theta_-\right].
\end{aligned}
\tag{2.25}
$$

In equation (2.22) H_- is a helical Luttinger liquid Hamiltonian like in equation (2.20). It describes the gappless modes with their helical spin properties at the Fermi points. Additionally to the helical Luttinger liquid, there are the gapped modes described by the Hamiltonian H_+. A relevant sine-Gordon field is responsible for the opening of a gap in these modes. Without H_{mix} the Hamiltonian is simply a sum of these two independent parts. Note that the Mott insulator is described by the same Hamiltonian if H_+ are the charge degrees of freedom and H_- the spin degrees of freedom. The only difference is in the definition of the fields ϕ_+ and ϕ_-. As a consequence the gap opens in a superposition of charge and spin degrees of freedom. Neglecting H_{mix} the model can be solved with standard Luttinger liquid techniques. However, H_{mix} vanishes only if $v_\rho = v_\sigma$ which is only true for the non-interacting system. Most of the works on spiral Luttinger liquids drop H_{mix} (e.g [4] or [34]). Some also include H_{mix} and treat the cosine only in a harmonic approximation (e.g. [22]). This approximation is only valid for energies much smaller or much larger than the gap.

This Luttinger liquid model is very useful for getting an idea about what happens when the interactions are turned on. One important result is that the size of the gap (in our case the spin-orbit gap) is significantly enhanced [6] [5],

$$
\Delta^{\text{SO}} = B^*_{(\text{eff})} = B_{(\text{eff})}\left(\frac{\xi}{a}\right)^{1-\frac{K}{2}}, \tag{2.26}
$$

with $K = K_\rho + K_\sigma^{-1}$ as in equation (2.24) and ξ the correlation length of the gapped modes. In our system repulsive interactions lead to Luttinger liquid coefficients $K_\rho < 1$ and $K_\sigma > 1$ and thus Δ^{SO} is increased, as we will confirm later.

Breather Bound States

At first, it may seem that as long as the energy is smaller than Δ^{SO}, the spiral Luttinger liquid has the same physics as the helical Luttinger liquid. However, this is only true in the noninteracting system. As soon as the interactions are turned on, the gapped modes begin to influence the gapless modes and particularly also inside of the spin-orbit gap.

H_+ in equation (2.22) is a sine-Gordon model, which physics are very well studied. The excitations in the sine-Gordon model are solitons and antisolitons with the mass of the spin-orbit gap Δ^{SO}. For repulsive interactions additional soliton-antisoliton bound states, which are also called breather bound states, appear with the masses [34]

$$
\Delta_n = 2\Delta^{\text{SO}}\sin\left(\frac{n\pi K}{8-2K}\right), \tag{2.27}
$$

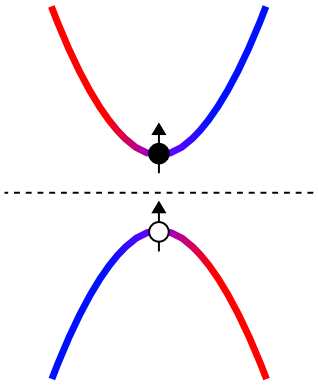

Figure 2.5: The gapped modes in our model. Breathers are bound states consisting of a particle excitation (soliton) on the upper branch and a hole excitation (antisoliton) on the lower branch. The spin $\leftarrow$ eigenstates are marked red and the spin $\rightarrow$ eigenstates in blue. At the minimum, respectiviely the maximum, of the gapped modes, the spin eigenstates are spin $\uparrow$ and $\downarrow$.

with $n = 1, \ldots, N$ and $N = \text{int}(\frac{4}{K} - 1)$ different breathers. They are called breathers because of the periodic oscillations in their time evolution. Later on we will observe these oscillations.

In our model the breathers correspond to bound states of a particle excitation (soliton) and a hole excitation (antisoliton) on the gapped modes. See figure 2.5 for an illustration. They are charge neutral but carry a positive $\hat{S}^z$ magnetization. The additional electron and the hole are bound together through the interaction. Theiy oscillate back and forth around their "center of mass", which can be observed in the time evolution. Plainest, the back and fourth oscillation can be seen in the current density j. Therefore breathers have a strong signal in the optical conductivity, which is related to the imaginary part of the current-current correlation function by

$$\begin{aligned} \sigma(\omega > 0) &= \frac{\text{Im}(\chi(\omega > 0))}{\omega}, \\ \chi(t) &= \frac{1}{L} \sum_i \langle j_i(t) j_0 \rangle \end{aligned} \tag{2.28}$$

As we will see they dominate the optical conductivity for repulsive interactions. Their energies lie inside the spin-orbit gap, therefore this is one example on how the gapped modes influence the system at energies smaller than the gap.

We already mentioned above that the Hamiltonian 2.22 can also be used to describe the Mott insulator, which has breather bound states too. They are known under the name Wannier-Mott exciton there.

2.2.3 Mott insulator

A Mott insulator is an insulating state driven by the interplay between the interactions and the lattice. Luttinger liquid physics is usually done in the continuum not considering a lattice. The lattice can be incorporated by including umklapp scattering processes. The momentum

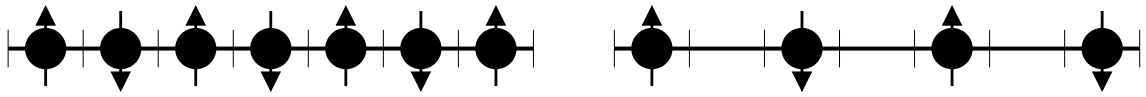

(a) Half-filling, U (b) Quarter-filling, U, U'

Figure 2.6: Mott insulators in one dimension.

on a lattice needs only to be conserved modulo a vector of the reciprocal lattice. This would lead to unimportant oscillating terms except when the filling is commensurate with the lattice. Then the oscillations can cancel and the umklapp terms may become relevant [15].

The Mott insulator at half filling can be easily understood. If the repulsive on-site interaction is bigger than the kinetic energy, then it is favorable to localize each particle rather than spreading it out in plane wave states, which have uniform density. See also figure 2.6 (a) for an illustration. Since a hopping would cost an energy of the order of the interaction U the system is an insulator. Note that the Mott transition only affects the charge degrees of freedom and leaves the spin degrees of freedom totally unaffected.

The same can also happen for a quarter-filled system. Here nearest-neighbour sites are left out because they would cost an energy of the order of U', see figure 2.6 (b). Obviously, this only works out with finite range interactions.

A renormalization group analysis yields the critical value of K_ρ, where the Mott transition occurs [15],

$$K_\rho^* = \frac{1}{n^2}, \tag{2.29}$$

with n the commensurability of the filling with the lattice, e.g. $n = 1$ for half-filling and $n = 2$ for quarter-filling and so forth. Therefore, the half-filled Mott transition occurs as soon as repulsive interactions are turned on. The quarter-filled Mott insulator has the critical value $K_\rho = 0.25$. It needs very strong interactions for a system to become a quarter-filled Mott insulator. The extended Hubbard model at quarter filling is one of the simplest models where it occurs. The phase diagram has been calculated in e.g. [10].

Chapter 3

Technical background

The numerical results in this work are all obtained by Matrix Product States (MPS) methods. We will give a short introduction to MPS and the methods used in this work. MPS are a very favorable representation of quantum states for physically interesting 1D quantum systems (extensions to higher dimensions also exist). After the great success of the Density Matrix Renormalization Group (DMRG) [40] it was pointed out by Östlund and Rommer [26] that DMRG in fact creates a MPS, which were first introduced in a different context as valence bound states (AKLT-state).

A thorough introduction to MPS, and also MPS methods, can be found in the review by Schollwöck [32]. The introduction to MPS in section 3.1 follows very closely the master thesis by Valentin Zauner [45].

After the introduction we will turn our focus on MPS methods. Firstly, we will discuss ground state determination using MPS, namely the DMRG algorithm. The section 3.2.1 about MPO's follows the master thesis of Martin Ganahl [13] and the section 3.2.2 about the finite size DMRG algorithm follows closely the review by Schollwöck [32].

Then we will focus on the time evolution using MPS, namely the TEBD algorithm. This section 3.3 again follows very closely the master thesis by Valentin Zauner [45].

Last but not least, applications of the above algorithms are presented for calculating spectral densities and Luttinger liquid coefficients.

3.1 Matrix Product States (MPS)

The key feature of MPS is their ability to describe one-dimensional quantum states and their features by a product of locally defined matrices of relatively small dimension, with high precision. Consider a general one-dimensional quantum system with L lattice sites, open boundary conditions and local Hilbert spaces $\{|\sigma_i\rangle\}$ of dimension d on each site. In a Hubbard type model we would have $d = 4$ and the σ_i could stand for the local states $|\ \rangle$, $|\uparrow\rangle$, $|\downarrow\rangle$ and $|\uparrow\downarrow\rangle$ respectively. The name σ_i is choosen for the local state because MPS representations had their first applications in spin chains. A general pure state on this system can be written in terms of the local bases as

$$|\psi\rangle = \sum_{\sigma_1 \ldots \sigma_L} c_{\sigma_1 \ldots \sigma_L} |\sigma_1 \ldots \sigma_L\rangle , \tag{3.1}$$

where we have in general d^L independent, delocalized expansion coefficients $c_{\sigma_1 \ldots \sigma_l}$. Now

we want to find a local description of this state, while keeping its quantum mechanical, non-local features. It is indeed possible to decompose the coefficients of (3.1) into a product of site dependent matrices of the following form

$$c_{\sigma_1 \ldots \sigma_L} = M^{\sigma_1} M^{\sigma_2} \ldots M^{\sigma_{L-1}} M^{\sigma_L}. \tag{3.2}$$

This is achieved by a subsequent decomposition of $c_{\sigma_1 \ldots \sigma_L}$. The variables σ_i are now merely a labeling for the matrices M. Each phyiscal site i has a set of d MPS matrices for each value of σ_i. The coefficients $c_{\sigma_1 \ldots \sigma_L}$ can be obtained by simply evaluating the corresponding matrix product.

3.1.1 Singular Value Decomposition (SVD)

MPS methods make extensive use of the singular value decomposition (SVD). The SVD is a factorization of a real or complex matrix with dimensions $m \times n$ into a product of two matrices and a diagonal matrix of the form

$$M = UDV^\dagger, \qquad\qquad M_{ij} = \sum_{k=1}^{N} U_{ik} D_k V^\dagger_{kj}, \tag{3.3}$$

where $N = \min(n, m)$. U is a $m \times N$ matrix, containing the orthonormal left singular vectors of M as its columns and V is a $n \times N$ matrix containing the right singular vectors of M as its columns. D is a diagonal $N \times N$ matrix with the N singular values d_k of M as its diagonal elements, which are real and non negative. For future applications it will be useful to think of D with its singular values in descending order, i.e. $d_1 \geq d_2 \geq \ldots$.

If $m < n$, U is an unitary square matrix of dimension $m \times m$, hence $U^\dagger U = UU^\dagger = \mathbb{1}$, whereas V is a $n \times m$ matrix with $V^\dagger V = \mathbb{1}$ only.

If $n < m$, V is an unitary square matrix of dimension $n \times n$, with $V^\dagger V = VV^\dagger = \mathbb{1}$, whereas U is a $m \times n$ matrix with $U^\dagger U = \mathbb{1}$ only.

3.1.2 Decomposition of arbitrary quantum states into MPS

The SVD can be used to obtain the matrices M^{σ_i} from the coefficients $c_{\sigma_1 \ldots \sigma_L}$. First start by reshaping $c_{\sigma_1 \ldots \sigma_L}$ into a $d \times d^{L-1}$ matrix and subject it to an SVD

$$c_{\sigma_1 \ldots \sigma_L} = \psi_{(\sigma_1)(\sigma_2 \ldots \sigma_L)} \overset{\text{SVD}}{=} \sum_{a_1=1}^{d} U_{(\sigma_1)a1} \lambda^{(1)}_{a_1} V_{a_1(\sigma_2 \ldots \sigma_L)}. \tag{3.4}$$

The $d \times d$ matrix $U_{(\sigma_1)a_1}$ will be reshaped into $A^{\sigma_1}_{a_1}$ and we call it the left boundary matrix. The index σ_1 is a physical index whereas the index a_1 will be called auxiliary index. Next we incorporate $\lambda^{(1)}_{a_1}$ into $V^\dagger_{a_1(\sigma_2 \ldots \sigma_L)}$ and reshape to a new matrix $\psi_{(a_1\sigma_1)(\sigma_3 \ldots \sigma_L)} = \lambda^{(1)}_{a_1} V^\dagger_{a_1(\sigma_2 \ldots \sigma_L)}$ of dimension $d^2 \times d^{L-2}$. Thus we have

$$c_{\sigma_1 \ldots \sigma_L} = \sum_{a_1=1}^{d} A^{\sigma_1}_{a_1} \psi_{(a_1\sigma_1)(\sigma_3 \ldots \sigma_L)}. \tag{3.5}$$

Next we decompose $\psi_{(a_1\sigma_1)(\sigma_3 \ldots \sigma_L)}$ via SVD

$$\psi_{(a_1\sigma_1)(\sigma_3\ldots\sigma_L)} = \sum_{a_2=1}^{d^2} U_{(a_1\sigma_2)a_2}\lambda^{(2)}_{a_2}V^{\dagger}_{a_2(\sigma_3\ldots\sigma_L)} \tag{3.6}$$

and again reshape $U_{(a_1\sigma_2)a_2}$ to $A^{\sigma_2}_{a_1a_2}$. Again we can combine $\psi_{(a_2\sigma_3)(\sigma_4\ldots\sigma_L)} = \lambda^{(2)}_{a_2}V^{\dagger}_{a_2(\sigma_3\ldots\sigma_L)}$ and finally get

$$c_{\sigma_1\ldots\sigma_L} = \sum_{a_1=1}^{d}\sum_{a_2=1}^{d^2} A^{\sigma_1}_{a_1}A^{\sigma_2}_{a_1a_2}\psi_{(a_2\sigma_3)(\sigma_4\ldots\sigma_L)}. \tag{3.7}$$

We will proceed in this fashion until we reach the last step

$$c_{\sigma_1\ldots\sigma_L} = \sum_{a_1a_2\ldots a_{L-1}} A^{\sigma_1}_{a_1}A^{\sigma_2}_{a_1a_2}\ldots A^{\sigma_{L-1}}_{a_{L-2}a_{L-1}}\lambda^{(L-1)}_{a_{L-1}}V^{\dagger}_{a_{L-1}\sigma_L} \tag{3.8}$$

where we will reshape one last time and form a column vector $\psi_{(a_{L-1}\sigma_L)} = \lambda^{(L-1)}_{a_{L-1}}V^{\dagger}_{a_{L-1}\sigma_L}$, which will be subjected to one more SVD

$$\psi_{(a_{L-1}\sigma_L)} = U_{(a_{L-1}\sigma_L)}\lambda^{(L)}V^{*}, \tag{3.9}$$

with U a column vector. $\lambda^{(L)}$, V^{*} are scalars and their product gives the norm $N = \sqrt{\langle\psi|\psi\rangle}$. If they are omitted the state is automatically normalized. One last time we will reshape $A^{\sigma_L}_{a_{L-1}} = U_{(a_{L-1}\sigma_L)}$ which is now a column vector. The normalized state can finally be written as

$$|\psi\rangle = \sum_{\{\sigma\}} A^{\sigma_1}A^{\sigma_2}\ldots A^{\sigma_{L-1}}A^{\sigma_L}\,|\sigma_1\ldots\sigma_L\rangle\,. \tag{3.10}$$

A similar MPS representation can be obtained by starting from the right end. This way we will get a MPS of the form

$$|\psi\rangle = \sum_{\{\sigma\}} B^{\sigma_1}B^{\sigma_2}\ldots B^{\sigma_{L-1}}B^{\sigma_L}\,|\sigma_1\ldots\sigma_L\rangle\,. \tag{3.11}$$

Since the matrices A^{σ_l} and B^{σ_l} arise from a SVD they automatically fulfill left- and right-normalization conditions

$$\sum_{\sigma_l} A^{\sigma_l\dagger}A^{\sigma_l} = \mathbb{1}, \tag{3.12}$$

$$\sum_{\sigma_l} B^{\sigma_l}B^{\sigma_l\dagger} = \mathbb{1}. \tag{3.13}$$

(3.10) is therefore called a left-normalized (or left-canonized) MPS and (3.11) is called a right-normalized (or right-canonized) MPS.

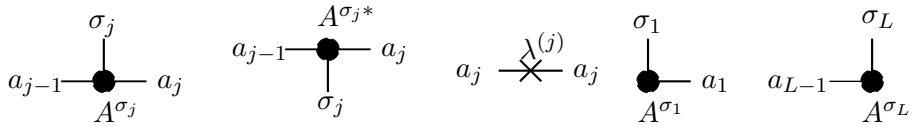

Figure 3.1: Graphical representation of MPS matrices. Matrices are represented by circles and indices by lines. Vertical lines represent physical indices of corresponding sites, horizontal lines represent auxiliary indixes connecting adjacent site. Complex conjugate matrices are depicted by an upside down version. Singular Values are represented by crosses. They are diagonal matrices, therefore the left and right index is the same. The boundary matrices have only one auxiliary index. All graphical representations equally hold for B matrices as well.

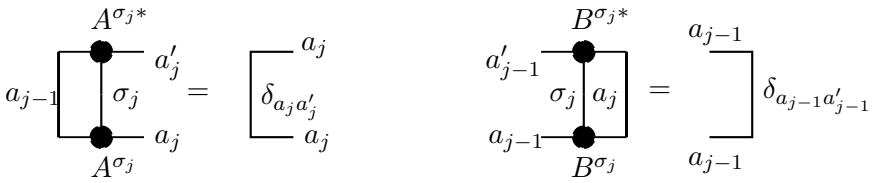

Figure 3.2: Graphical representation of the left and right normalization conditions (3.12) and (3.13). Each of them produces a Kronecker delta.

3.1.3 Schmidt Decomposition

The two representations (3.10) and (3.11) can be combined to form a mixed-canonical state. For this we would perform the left-canonized decomposition up to a certain site l and then perform the right-canonized decomposition on the remaining matrix $\psi_{(a_{l-1}\sigma_l)(\sigma_{l+1}\dots\sigma_L)}$ from the right up to site $l+1$

$$c_{\sigma_1\dots\sigma_L} = \sum_{a_1 a_2 \dots a_{L-1}} A^{\sigma_1}_{a_1} \dots A^{\sigma_{l-1}}_{a_{l-2}a_{l-1}} \psi^{\sigma_l\sigma_{l+1}}_{a_{l-1}a_{l+1}} B^{\sigma_{l+2}}_{a_{l+1}a_{l+2}} \dots B^{\sigma_L}_{a_{L-1}}. \tag{3.14}$$

Where we introduced the 2-site wave function $\psi^{\sigma_l\sigma_{l+1}}_{a_{l-1}a_{l+1}}$. Alternatively, one can decompose this wavefunction via SVD $\psi^{\sigma_l\sigma_{l+1}}_{a_l a_{l+1}} = A^{\sigma_l}_{a_{l-1}a_l}\lambda^{(l)}B^{\sigma_{l+1}}_{a_l a_{l+1}}$. We can now write the mixed canocical representations

$$|\psi\rangle = \sum_{\{\sigma\}} A^{\sigma_1}A^{\sigma_2}\dots A^{\sigma_{l-1}}\psi^{\sigma_l\sigma_{l+1}}B^{\sigma_{l+2}}\dots B^{\sigma_{L-1}}B^{\sigma_L}\,|\sigma_1\dots\sigma_L\rangle\,, \tag{3.15}$$

$$|\psi\rangle = \sum_{\{\sigma\}} A^{\sigma_1}A^{\sigma_2}\dots A^{\sigma_{l-1}}A^{\sigma_l}\lambda^{(l)}B^{\sigma_{l+1}}B^{\sigma_{l+2}}\dots B^{\sigma_{L-1}}B^{\sigma_L}\,|\sigma_1\dots\sigma_L\rangle\,. \tag{3.16}$$

$$\tag{3.17}$$

The mixed canonical representation corresponds to a Schmidt decomposition of $|\psi\rangle$ at bond l, $l+1$. Consider a general splitting of a state in terms of basis states defined on two sublattices, which are the two parts of the lattice left and right of bond l, $l+1$

$$|\psi\rangle = \sum_{ij} C_{ij}\,|\psi^L_i\rangle\,|\psi^R_j\rangle\,, \tag{3.18}$$

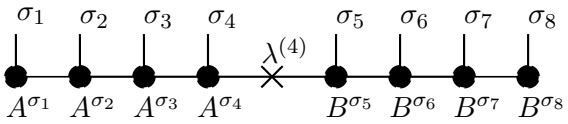

Figure 3.3: Graphical representaion of an 8 site mixed canonical MPS. Whenever two lines of different matrices are connected, there is an implicit sum over these indices. All auxiliary indices a_j are summed over and only the physical indices σ_j survive. One set of physical indices corresponds to one coefficient $c_{\sigma_1 \ldots \sigma_L}$.

where $\{|\psi_i^L\rangle\}$ and $\{|\psi_j^R\rangle\}$ are orthonormal basis sets defined on the sublattice L containing sites $[1, \ldots, l]$ and sublattice R containing sites $[l+1, \ldots, L]$.

In a Schmidt decomposition the two basis sets are choosen in such a way that that the expansion coefficient matrix only contains diagonal elements. This can be achieved by performing a SVD of the expansion coefficient matrix $C_{ij} = U_{ik}\lambda_k V_{kj}^\dagger$. Matrices U and V correspond to basis transormations onto new orthonormal basis sets on both sublattices $|\phi_k^L\rangle = \sum_i U_{ik} |\psi_i^L\rangle$ and $|\phi_k^R\rangle = \sum_i V_{jk}^* |\psi_j^R\rangle$ such that

$$|\psi\rangle = \sum_k \lambda_k |\phi_k^L\rangle |\phi_k^R\rangle . \tag{3.19}$$

(3.19) is then the Schmidt decomposition, the weights λ_k are called Schmidt values and the vectors $\{|\phi_k^L\rangle\}$ and $\{|\phi_k^R\rangle\}$ are called left and right Schmidt vectors. It can be shown that the mixed canonical representation (3.16) indeed corresponds to such a Schmidt decomposition with $\lambda^{(l)}$ the Schmidt values. Furthermore, the reduced density matrices can be easily obtained for blocks L and R using the Schmidt decomposition

$$\hat{\rho}_L^{(l)} = \mathrm{Tr}_R |\psi\rangle \langle\psi| = \sum_k \lambda_k^2 |\phi_k^L\rangle \langle\phi_k^L| , \tag{3.20}$$

$$\hat{\rho}_R^{(l)} = \mathrm{Tr}_L |\psi\rangle \langle\psi| = \sum_k \lambda_k^2 |\phi_k^R\rangle \langle\phi_k^R| . \tag{3.21}$$

The singular values λ_k fulfill the necessary constraint $\sum_k \lambda_k^2 = 1$ for a statistical operator, if the state is normalized. This also means that they quantify the bipartite entanglement entropy between blocks L and R via the von Neumann entropy

$$S_{LR} = -\mathrm{Tr}\hat{\rho}_L \log_2 \hat{\rho}_L = -\mathrm{Tr}\hat{\rho}_R \log_2 \hat{\rho}_R = -\sum_k \lambda_k^2 \log_2 \lambda_k^2 . \tag{3.22}$$

3.1.4 Canonical Representation

A different representation of MPS, which focus lies more on the Schmidt decomposition, is used in the TEBD algorithm. The aim of this representation is to easily access all possible Schmidt decomposition at all bonds at all times. The mixed canonical MPS allows only access to the Schmidt decomposition at site l, $l+1$. By slightly modifying the dedomposition procedure from section 3.1.2 we can expose all Schmidt decompositions at all bonds simultaniously.

We have to do the same decomposition procedure as in section 3.1.2. Starting again with (3.4), but now we define

$$A^{\sigma_1}_{a_1} = \Gamma^{\sigma_1}_{a_1}. \tag{3.23}$$

Then we keep proceeding, but remember all the $\lambda^{(l)}$ matrices. For $l = 2 \dots L$ the relation between the A and the Γ matrices is

$$A^{\sigma_l}_{a_{l-1}a_l} = \lambda^{(l-1)}_{a_{l-1}} \Gamma^{\sigma_l}_{a_{l-1}a_l} \tag{3.24}$$

For decomposing from the right we can make the analog definitions

$$B^{\sigma_L}_{a_{L-1}} = \Gamma^{\sigma_L}_{a_{L-1}}, \tag{3.25}$$

$$B^{\sigma_l}_{a_{l-1}a_l} = \Gamma^{\sigma_l}_{a_{l-1}a_l} \lambda^{(l)}_{a_l}. \tag{3.26}$$

Either way we can replace all A and B matrices and write in matrix notation

$$|\psi\rangle = \sum_{\{\sigma\}} \Gamma^{\sigma_1} \lambda^{(1)} \Gamma^{\sigma_2} \lambda^{(2)} \Gamma^{\sigma_3} \dots \Gamma^{\sigma_{L-1}} \lambda^{(L-1)} \Gamma^{\sigma_L} |\sigma_1 \dots \sigma_L\rangle . \tag{3.27}$$

Since there is no distinction between left- or right- canonization anymore, this form is called the canonical representation of a MPS. The Schmidt decomposition of all bonds can be easily accessed now

$$|\psi\rangle = \sum_{a_l} \lambda^{(l)}_{a_l} |a^L_l\rangle |a^R_l\rangle , \tag{3.28}$$

with the Schmidt vectors

$$|a^L_l\rangle = \sum_{\sigma_1 \dots \sigma_l} (\Gamma^{\sigma_1} \lambda^{(1)} \Gamma^{\sigma_2} \dots \lambda^{(l-1)} \Gamma^{\sigma_l})_{a_l} |\sigma_1 \dots \sigma_l\rangle , \tag{3.29}$$

$$|a^R_l\rangle = \sum_{\sigma_{l+1} \dots \sigma_L} (\Gamma^{\sigma_{l+1}} \lambda^{(l+1)} \dots \lambda^{(L-1)} \Gamma^{\sigma_L})_{a_l} |\sigma_{l+1} \dots \sigma_L\rangle . \tag{3.30}$$

By comparison to the normalization conditions for the A and B matrices, the normalization conditions for the canonical representation yields

$$\sum_{\sigma_l} \Gamma^{\sigma_l \dagger} (\lambda^{(l-1)})^2 \Gamma^{\sigma_l} = \mathbb{1}, \tag{3.31}$$

$$\sum_{\sigma_l} \Gamma^{\sigma_l} (\lambda^{(l)})^2 \Gamma^{\sigma_l \dagger} = \mathbb{1}, \tag{3.32}$$

defining $\lambda^{(0)} = \lambda^{(L)} = 1$.

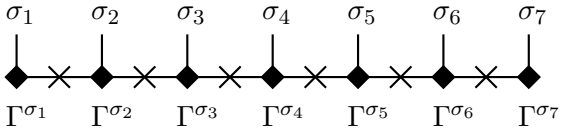

Figure 3.4: Graphical representaion of a MPS in the canonical representation. The Γ matrices are depicted as small filled diamonds. The Schmidt values are again represented by the crosses.

3.1.5 Compression of a MPS

Every state can be exactly decomposed into a MPS without any loss of information. However, the basis sets grow exponentially in dimension the further one goes into the center of the chain. The Hilbert spaces of $\{|a_l^L\rangle\}$ and $\{|a_l^R\rangle\}$ are of dimension d^l and d^{L-l} respectively. This is not useful for a practical representation of a quantum state. Therefore, a maximum dimension m for the MPS matrices is introduced. All matrices of larger size are cutted to that maximum dimension. This procedure is called truncation and the truncated MPS matrices will then generally be a collection of d matrices of dimension $m \times m$. By doing this the derived MPS will generally only be an approximation to the original state. Note that the normalization conditions (3.12), (3.13), (3.31) and (3.32) still hold for the truncated matrices.

For getting the best possible approximation of the original state it is important to use the optimal truncation procedure. The procedure is straight forward using the decomposition via SVD. After each SVD we only use the first m left and right singular vectors, corresponding to the m largest Schmidt values. This means that we will only use the first m columns of U and the first m rows of $V^\dagger$ and discard the rest. The sum over the discarded Schmidt values, the discarded weight, gives a first order approximation about the error one introduces by the truncation. Memory efforts now scale linearly with system size, as opposed to exponentially. Fortunately it turns out that due to the entanglement nature of one-dimensional systems, truncated MPS are still a very good approximation. We will see that the DMRG algorithm already provides an optimally compressed MPS.

3.1.6 Norms and Expectation Values

Due to the normalization conditions for MPS matrices norms and local expectation values can be evaluated very efficiently. Consider an MPS in the mixed-canonical form (3.16). Its norm $\langle\psi|\psi\rangle$ can be written as

$$\langle\psi|\psi\rangle = \sum_{\{\sigma\}} (B^{\sigma_L\dagger} \dots B^{\sigma_l\dagger} \lambda^{(l)} A^{\sigma_l\dagger} \dots A^{\sigma_1\dagger})(A^{\sigma_1} \dots A^{\sigma_l} \lambda^{(l)} B^{\sigma_{l+1}} \dots B^{\sigma_L}). \tag{3.33}$$

By sequentially using the normalization conditions (3.12) and (3.13) the norm simplifies to

$$\langle\psi|\psi\rangle = \sum_{a_l} (\lambda_{a_l}^{(l)})^2. \tag{3.34}$$

If the state is properly normalized the eigenvalues of the reduced density operators (which $\lambda^{(l)}$ is exactly) should sum up to one.

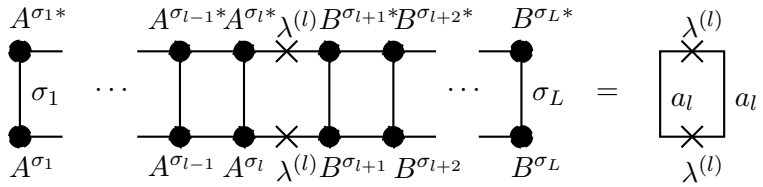

Figure 3.5: Graphical representation for the calculation of the norm of a MPS state. By exploiting the normalization conditions of the MPS matrices (see figure 3.2) sequentially from the outside, one finds that all that is left is the sum over the square of the Schmidt values.

The above result can be readily extended to expectation values of local operators

$$\hat{O}_l = \sum_{\sigma_l' \sigma_l} O^{\sigma_l' \sigma_l} \left|\sigma_l'\right\rangle \left\langle\sigma_l\right| . \tag{3.35}$$

Evaluating the expectation value for a state in a mixed-canonical MPS form

$$\begin{aligned} \langle \hat{O}_l \rangle &= \langle\psi| \hat{O}_l |\psi\rangle \\ &= \sum_{\{\sigma\}} (B^{\sigma_L \dagger} \dots B^{\sigma_l \dagger} \lambda^{(l)} A^{\sigma_l \dagger} \dots A^{\sigma_1 \dagger}) O^{\sigma_l' \sigma_l} (A^{\sigma_1} \dots A^{\sigma_l} \lambda^{(l)} B^{\sigma_{l+1}} \dots B^{\sigma_L}). \end{aligned} \tag{3.36}$$

Again by rearranging and exploiting the normalization conditions one can evaluate the expectation value efficiently

$$\langle \hat{O}_l \rangle = \sum_{\sigma_l' \sigma_l} O^{\sigma_l' \sigma_l} \mathrm{Tr}(M^{\sigma_l' \dagger} M^{\sigma_l}) \tag{3.37}$$

where we defined the center Matrix $M^{\sigma_l} = A^{\sigma_l} \lambda^{(l)}$. The canonical representation of a MPS is especially useful in this context since the mixed representation is readily available for all sites. We can equally write

$$M^{\sigma_l} = A^{\sigma_l} \lambda^{(l)} = \lambda^{(l-1)} B^{\sigma_l} = \lambda^{(l-1)} \Gamma^{\sigma_l} \lambda^{(l)}. \tag{3.38}$$

Therefore one needs only the MPS matrices at the site j and the adjacent Schmidt values instead of d^L general coefficients in the case of states like (3.1)!

Quite generally, this scheme can be extended to two and multiple site operators and also correlations. Furthermore, overlaps between different MPS states and the application of operators on MPS states are also calculated with the techniques introduced here. The interested reader will find anything one needs to know about MPS in the review by Schollwöck [32].

3.2 The Density Matrix Renormalization Group (DMRG)

DMRG is by far the most powerful and successful method for determining ground states and the first excited states of one-dimensional strongly correlated systems. It is a variational method, its general principle is to find a state $|\psi\rangle$ in a certain class of ansatz states (mixed-canonical MPS in the case of DMRG) that minimize the energy expectation value

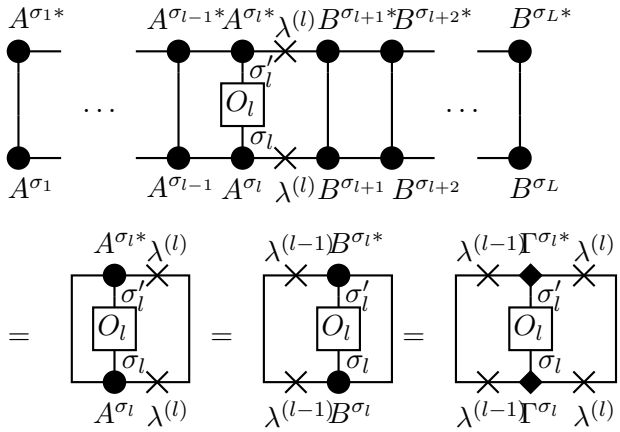

Figure 3.6: Graphical representation of the expectation value $\langle \hat{O}_l \rangle$ of a local operator. The lower panel shows the possible outcomes after the application of the normalization conditions.

$$E = \frac{\langle \psi | H | \psi \rangle}{\langle \psi | \psi \rangle}. \tag{3.39}$$

As the name suggests, DMRG has its roots in renormalization group methods [41]. Its original form relies on constructing an underlying system site by site by subsequent reduced basis transformations, projecting onto important degrees of freedom. A renormalized Hilbert space of the underlying system is generated step by step, which will be of significantly lower dimension.

In every step DMRG projects onto a (generally fixed) number of states, which are the most prominent eigenstates of the reduced density matrix of the system of current size. After L steps one is left with an effective Hamiltonian for the underlying L site system, but with significantly reduced Hilbert space dimension. The ground state (and the first few excited states) of this Hamiltonian can then be effciently determined by an iterative eigensolver e.g. the Lanczos method. There are two versions of DMRG, the infinite size DMRG and finite size DMRG. In this work only the latter is used. As before details can be found in [32]. But before we can start we have to cast the Hamiltonian into the same language as the MPS state.

3.2.1 Matrix Product Operators (MPO)

In the same way as we defined MPS we can also define a Matrix Product Operator (MPO). As the MPS lives on a product Hilbert space of local Hilbert spaces the MPO lives on a product operator space of local operator spaces.

We write the MPO with the matrices $W^{\sigma\sigma'}$ just like the M^{σ} from (3.2), with the only difference that as representations of operators they need both outgoing and ingoing physical states:

$$\hat{O} = \sum_{\{\sigma\}\{\sigma'\}} W^{\sigma_1 \sigma_1'} W^{\sigma_2 \sigma_2'} \dots W^{\sigma_{L-1} \sigma_{L-1}'} W^{\sigma_L \sigma_L'} |\sigma_1 \dots \sigma_L\rangle \langle \sigma_1' \dots \sigma_L'| \tag{3.40}$$

As with the MPS it can be shown that any Operator can be written in the MPO language. Applying a MPO on a MPS is straight forward

$$\begin{aligned}\hat{O}\,|\psi\rangle &= \sum_{\{\sigma\}\{\sigma'\}} (W^{\sigma_1\sigma_1'}W^{\sigma_2\sigma_2'}\dots)(M^{\sigma_1'}M^{\sigma_2'}\dots)\,|\sigma_1\sigma_2\dots\rangle \\ &= \sum_{\{\sigma\}} \underbrace{\left(\sum_{\sigma_1'} W^{\sigma_1\sigma_1'}M^{\sigma_1'}\right)}_{\tilde{M}^{\sigma_1}} \underbrace{\left(\sum_{\sigma_2'} W^{\sigma_2\sigma_2'}M^{\sigma_2'}\right)}_{\tilde{M}^{\sigma_2}} \dots |\sigma_1\sigma_2\dots\rangle\,. \end{aligned} \tag{3.41}$$

Note that we did not write out the indices:

$$\tilde{M}^{\sigma_l}_{(b_{l-1}a_{l-1})(b_la_l)} = \sum_{\sigma_1'} W^{\sigma_1\sigma_1'}_{b_{l-1}b_l} M^{\sigma_1'}_{a_{l-1}a_l}. \tag{3.42}$$

The indices of the MPO matrices W are called b_i and they should never be confused with the indices of the MPS matrices a_i. The former ones act in operator space, whereas the latter ones act in Hilbert space.

Like the MPS an MPO can be obtained by a sequential decomposition procedure. However, in most cases this is not necessary as we will see below. An example for writing one and two site operators will be given for open boundary conditions. The type of operators given below appear very often in Hamiltonians for strongly correlated systems

$$\hat{O}^{[1]} = \sum_{l=1}^{L} \hat{O}_l \tag{3.43}$$

$$\hat{O}^{[2]} = \sum_{l=1}^{L-1} \hat{O}_{l,l+1} = \sum_{l=1}^{L-1} \hat{A}_l\hat{B}_{l+1} \tag{3.44}$$

The representation of the first one as a MPO is as follows

$$W^{(l)} = \begin{cases} \begin{pmatrix} O_1 & \mathbb{1} \end{pmatrix} & \text{left boundary, } l=1 \\ \begin{pmatrix} \mathbb{1} & 0 \\ O_l & \mathbb{1} \end{pmatrix} & \text{bulk, } 1<l<L \\ \begin{pmatrix} \mathbb{1} \\ O_L \end{pmatrix} & \text{right boundary, } l=L. \end{cases} \tag{3.45}$$

The two site operators can be written like below

$$W^{(l)} = \begin{cases} \begin{pmatrix} 0 & A_1 & \mathbb{1} \end{pmatrix} & \text{left boundary, } l=1 \\ \begin{pmatrix} \mathbb{1} & 0 & 0 \\ A_l & 0 & 0 \\ 0 & B_l & \mathbb{1} \end{pmatrix} & \text{bulk, } 1<l<L \\ \begin{pmatrix} \mathbb{1} \\ B_L \\ 0 \end{pmatrix} & \text{right boundary, } l=L. \end{cases} \tag{3.46}$$

Note that we omitted the hat on the Operators. This indicates that O_l, A_l and B_l are the $d \times d$ dimensional matrix representations of the operators $\hat{O}_l$, $\hat{A}_l$ and $\hat{B}_l$. Additionally,

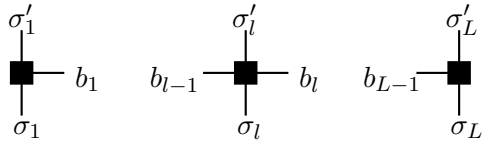

Figure 3.7: Graphical representation of the MPO matrices on the very left site, sites in between and the rightmost site. They are represented by small filled squares. Note that MPO matrices have auxiliary indices b_l which are not to be confused with the MPS auxiliary indices.

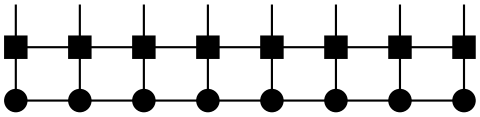

Figure 3.8: Graphical representation of the application of a MPO on a MPS state.

there are the auxiliary indices with dimension 2 for one site operators and 3 for the two site operators. That these MPOs have the correct form can be immediatly tested by evaluating the matrix product

$$\hat{O} = \prod_{l=1}^{L} W^{(l)}. \tag{3.47}$$

3.2.2 Finite size DMRG

Now that we have our Hamiltonian in MPO language we can start our quest to minimize (3.39). The most efficient way is a variational search in the MPS space. Note that there are other MPS methods, like imaginary time evolution, but DMRG outperforms them by far.

In order to minimize (3.39), we introduce a Lagrangian multiplier λ, and extremize

$$\langle\psi| H |\psi\rangle - \lambda\langle\psi|\psi\rangle \tag{3.48}$$

so that in the end ψ will be the ground state and λ the ground state energy (see also figure 3.9). The trick of the DMRG algorithm is now to keep all MPS matrices fixed and consider only the matrices on sites l and $l+1$ as variables, thus the two site wave function $\psi^{\sigma_l\sigma_{l+1}}_{a_{l-1}a_{l+1}}$. In our implementation of the DMRG algorithm the two site wavefunction is minimized, but it would be also possible to minimize only a single site matrix. However, this single-site DMRG is much more prone to get stuck in a local minimum than the two-site DMRG algorithm. Although, a DMRG sweep in the two-site algorithm needs more computer time it compensates that by converging much faster and is generally more reliable.

After the extremization of (3.48), with respect to $\psi^{\sigma_l\sigma_{l+1}}$, we end up with a generalized eigenvalue problem. We don't give the formulas here but rather refer to the much more lucid graphical representation in figure 3.10. The graphical representation can be converted into equations right away if needed. It is a little bit inconvenient that we have to solve a generalized eigenvalue problem and not a simple eigenvalue problem. Here comes the magic of MPS matrices into play. By choosing a mixed canonical representation of our MPS such that all matrices left of l are left orthonormalized A matrices and all sites right of $l+1$

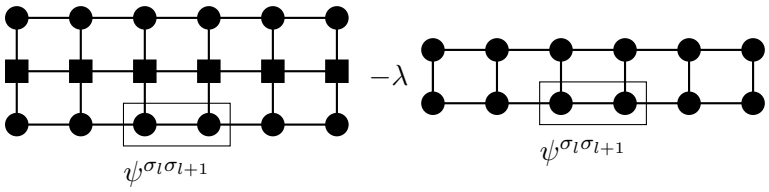

Figure 3.9: Graphical representation of equation (3.48). The two site wave function in which we want to extremize is indicated by the square.

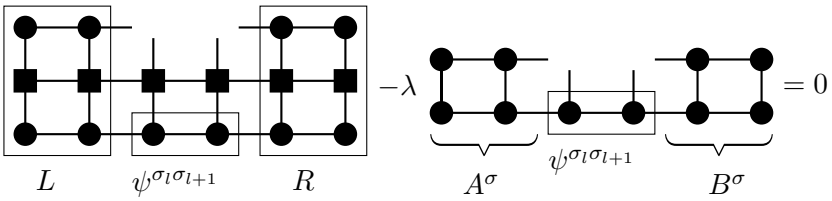

Figure 3.10: Graphical representation of the extremum of equation (3.48). This is a generalized eigenvalue problem for the two site wave function $\psi^{\sigma_l\sigma_{l+1}}$. The MPS is in a mixed canonical representation, namely all MPS matrices left of l are left orthonormalized A matrices and all sites right of $l+1$ are right orthonormalized B matrices. The left expression has the L and R expressions marked.

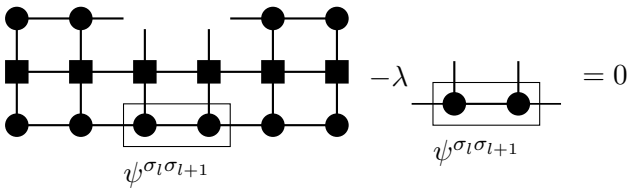

Figure 3.11: The same as figure 3.10, but after the application of the normalization conditions. We arrived at a simple eigenproblem.

are right orthonormalized B matrices the problem can be further simplified. After applying the normalization conditions (3.12) and (3.13) we arrive at a simple eigenvalue problem in figure 3.11. This can be solved by an iterative ground state search. The left L- and right R-expressions indicated in figure 3.10 don't have to be calculated for each DMRG step. They can be efficiently evaluated iteratively and then stored in advance for each site l.

Finally we can give the optimal finite size DMRG algorithm:

1. As DMRG is an iterative method a suitable starting point should be choosen. In many cases the infinite size DMRG algorithm can provide a good inital MPS state which is then further optimized by the finite size DMRG. However, any starting MPS is suitable, one just has to take care that the initial state is in the same symmetry sector as the ground state. In most cases a simple product state is a good enough starting point. Furthermore, the DMRG algorithm makes extensive use of the orthonormalization conditions of the MPS matrices. In the version presented here it is mandatory that one starts with a right normalized initial state consisting only of B matrices.

2. Calculate the R-expressions for all site positions from $L-2$ trough 1 iteratively. Store $R_{a_{l+1}b_{l+1}a'_{l+1}}$ for each position.

3. *Right sweep:* Starting from site $l=1$ through site $L-2$, sweep through the lattice to the right as follows: construct the two-site wave function from B^{σ_l} and $B^{\sigma_{l+1}}$. Solve the standard eigenproblem by an iterative eigensolver for $\psi^{\sigma_l\sigma_{l+1}}$. Since it is an iterative process its current value is a good starting point. Once the solution is obtained, use the SVD to decompose the eigenvector $\tilde{\psi}^{\sigma_l\sigma_{l+1}}$ into two MPS matrices A^{σ_l} and $B^{\sigma_{l+1}}$ to maintain the desired normalization structure. During this step the auxiliary matrix dimension will grow. Use truncation if it gets bigger than the maximum matrix dimension m. The two-site wave function constructed from $A^{\sigma_{l+1}}$ and $B^{\sigma_{l+2}}$ will be the starting guess for the eigensolver for the next site. Build iteratively the L expression by adding one more site. Move on by one site, $l \to l+1$, and repeat.

4. *Left sweep:* Starting from site $l=L-1$ through site 2, sweep through the lattice now to the left doing the same steps as above. Now you have to build the R expressions iteratively.

5. Sweep through the lattice until convergence is achieved. Convergence is achieved if energy converges. The variance of the state $\langle\psi| H^2 |\psi\rangle - (\langle\psi| H |\psi\rangle)^2)$ is also a good test for convergence. It should approach 0 as close as possible.

The algorithm is sketched in figure 3.12 with the matrices labeled by a subscript index i to label the number of updates. The two site wavefunction is denoted by $\psi^{[2]}$.

3.3 Time evolution with MPS

The time evolution of quantum states is of central interest in quantum mechanics, both real-time evolution and also imaginary-time evolution for the use in statistical mechanics (with β as the imaginary-time). The time evolution was actually one of the first applications of MPS. The TEBD algorithm, first proposed by Vidal [39], allows accurate extraction of the time evolution. Shortly thereafter, it was applied on DMRG matrices in the tDMRG method [8].

$$
\begin{aligned}
&\underbrace{B_0 B_0}_{\psi^{[2]}} B_0 B_0 B_0 B_0 \\
\overset{\text{diag}}{\to} &\tilde{\psi}^{[2]} B_0 B_0 B_0 B_0 \overset{\text{SVD}}{\to} A_1 \underbrace{B_1 B_0}_{\psi^{[2]}} B_0 B_0 B_0 \\
\overset{\text{diag}}{\to} &A_1 \tilde{\psi}^{[2]} B_0 B_0 B_0 \overset{\text{SVD}}{\to} A_1 A_1 \underbrace{B_1 B_0}_{\psi^{[2]}} B_0 B_0 \\
\overset{\text{diag}}{\to} &A_1 A_1 \tilde{\psi}^{[2]} B_0 B_0 \overset{\text{SVD}}{\to} A_1 A_1 A_1 \underbrace{B_1 B_0}_{\psi^{[2]}} B_0 \\
\overset{\text{diag}}{\to} &A_1 A_1 A_1 \tilde{\psi}^{[2]} B_0 \overset{\text{SVD}}{\to} A_1 A_1 A_1 A_1 \underbrace{B_1 B_0}_{\psi^{[2]}} \\
\overset{\text{diag}}{\to} &A_1 A_1 A_1 A_1 \tilde{\psi}^{[2]} \overset{\text{SVD}}{\to} A_1 A_1 A_1 \underbrace{A_1 B_1}_{\psi^{[2]}} B_1 \\
\overset{\text{diag}}{\to} &A_1 A_1 A_1 \tilde{\psi}^{[2]} B_1 \overset{\text{SVD}}{\to} A_1 A_1 \underbrace{A_1 B_2}_{\psi^{[2]}} B_2 B_1 \\
\overset{\text{diag}}{\to} &A_1 A_1 \tilde{\psi}^{[2]} B_2 B_1 \overset{\text{SVD}}{\to} A_1 \underbrace{A_1 B_2}_{\psi^{[2]}} B_2 B_2 B_1
\end{aligned}
$$

Figure 3.12: Two site DMRG algorithm

Although both implementations are mathematically equivalent, they differ in their numerical implementation. The TEBD algorithm makes use of the canonical MPS representation and allows for a efficient parallelization. Both methods rely on the Suzuki-Trotter decomposition and both methods constantly adapt the reduced Hilbert-space to optimally approximate the true time dependent quantum state. Therefore they are adaptive MPS time evolution methods.

3.3.1 The Suzuki-Trotter Decomposition

As it is well known from basic quantum mechanics lectures, the time evolution of quantum mechanical states is governed by the time dependent Schrödinger equation

$$i\frac{\partial}{\partial t}\left|\psi(t)\right\rangle = H\left|\psi(t)\right\rangle, \tag{3.49}$$

with $|\psi(t)\rangle$ the time dependent state of the system and H the Hamiltonian. The time evolution operator $\hat{U}$ is the formal solution of the Schrödinger equation

$$i\frac{\partial}{\partial t}\hat{U}(t) = H\hat{U}(t) \tag{3.50}$$

and can be written

$$\hat{U} = \hat{T}e^{-i\int_0^t H(t')dt'}, \tag{3.51}$$

$$\left|\psi(t)\right\rangle = \hat{U}(t)\left|\psi(0)\right\rangle \tag{3.52}$$

with $\hat{T}$ the time ordering operator, which is important if $[H(t), H(t')] \neq 0$. In the following we will assume a time-independent Hamiltonian. In this case the integration is trivial

$$\hat{U}(t) = e^{-itH} \tag{3.53}$$

The time evolution can be split up into an arbitrary amount of sequential time evolutions of smaller time intervals, e.g. in N equally spaced intervals τ

$$\hat{U}(t) = e^{-itH} = e^{-i\tau H} = \hat{U}(\tau)^N, \tag{3.54}$$

with $N = \frac{t}{\tau}$.

Now we want to consider one-dimensional Hamiltonians on a L-site lattice, with L even, consisting of nearest neighbor couplings only. Therefore, H is of the following form

$$H = \sum_j \hat{h}_{j,j+1}, \tag{3.55}$$

with $\hat{h}_{j,j+1}$ the two-site Hamiltonians. In general, these two-site Hamiltonians will not commute with one another. Therefore, a straight forward decomposition of (3.53) in a product of exponentials containing only the two-site Hamiltonians is not possible. However, the first order Suzuki-Trotter decomposition allows for an approximate decomposition

$$\hat{U}(\tau) = e^{-i\tau H} = e^{-i\tau H_o}e^{-i\tau H_e} + \mathcal{O}(\tau^2) \tag{3.56}$$

with $H = H_o + H_e$ and H_o containing only the odd bonds and H_e only the even bonds

$$H_o = \sum_{j=1}^{\frac{L}{2}} \hat{h}_{2j-1,2j}, \tag{3.57}$$

$$H_e = \sum_{j=1}^{\frac{L}{2}} \hat{h}_{2j,2j+1}. \tag{3.58}$$

Because we have to apply $\hat{U}(\tau)$ $N = \frac{t}{\tau}$ times to perform the time evolution until time t, the final approximation error becomes

$$\hat{U}(t) = \hat{U}(\tau)^N = (e^{-i\tau H_o} e^{-i\tau H_e})^N + \mathcal{O}(\tau). \tag{3.59}$$

The advantage of this Suzuki-Trotter decomposition is that all two-site Hamiltonians in H_o and H_e only commute with each other respectively. Therefore, they can be exactly decomposed into a product of two-site time evolution operators

$$\hat{U}_o(\tau) = e^{-i\tau H_o} = \bigotimes_{j=1}^{\frac{L}{2}} e^{-i\tau \hat{h}_{2j-1,2j}} = \bigotimes_{j=1}^{\frac{L}{2}} \hat{u}_{2j-1,2j}(\tau), \tag{3.60}$$

$$\hat{U}_e(\tau) = e^{-i\tau H_e} = \bigotimes_{j=1}^{\frac{L}{2}-1} e^{-i\tau \hat{h}_{2j,2j+1}} = \bigotimes_{j=1}^{\frac{L}{2}-1} \hat{u}_{2j,2j+1}(\tau), \tag{3.61}$$

with the two-site time evolution operator $\hat{u}_{j,j+1}(\tau)$. As can be seen from equation (3.59) the error is of first order in τ, hence first order Suzuki-Trotter decomposition. With only very little additional effort one can use the second order Suzuki-Trotter decomposition

$$\hat{U}(\tau) = e^{-i\tau H} = e^{-i\frac{\tau}{2} H_o} e^{-i\tau H_e} e^{-i\frac{\tau}{2} H_o} + \mathcal{O}(\tau^3). \tag{3.62}$$

In a time evolution the operator $\hat{U}(\tau)$ has to be applied many times. The intermediate time steps technically become first order, since $\hat{U}_o(\frac{\tau}{2})\hat{U}_o(\frac{\tau}{2}) = \hat{U}_o(\tau)$. Therefore the $\frac{\tau}{2}$ timesteps only have to be applied in the beginning and in the end. We automatically have a second order Suzuki-Trotter decomposition with only a very slight variation of the first order algorithm. Occasionally measurements are carried out at timesteps t_{meas}. One has to take care at these timesteps and perform one $\frac{\tau}{2}$ odd update then measure and then another $\frac{\tau}{2}$ odd update after measuring.

In the following, only first and second order Suzuki-Trotter updates are considered.

3.3.2 Time Evolving Block Decimation (TEBD)

The Time Evolving Block Decimation (TEBD) algorithm was first proposed by Vidal in 2003 [39]. It also introduced the canonical representation of MPS, since its focus lies on easy access on all possible Schmidt decompositions. The algorithm generally provides a method for updating a finite size MPS after applying one- or two-site operators on it. Its main use is, however, the real and imaginary time evolution of quantum states in MPS form.

The time evolution operator $\hat{U}(\tau)$ is sequentially applied N times for calculating the time evolution up to time t. Intermediate measurements can be carried out at as desired. For first order Suzuki-Trotter decomposition (which can be easily adapted to second order, see above), one Trotter time step consists of first applying $\hat{U}_o(t)$ to all odd bonds and then $\hat{U}_e(t)$ to all even bonds. The algorithm runs as follows:

1. Start with odd bonds and set $j = 1$.

2. To apply $\hat{u}_{j,j+1}$ to bond j, $j+1$ construct the two-site wave function like in section 3.1.3

$$\psi^{\sigma_j\sigma_{j+1}} = \lambda^{(j-1)}\Gamma^{\sigma_j}\lambda^{(j)}\Gamma^{\sigma_{j+1}}\lambda^{(j+1)}, \tag{3.63}$$

   using the definitions $\lambda^{(0)} = \lambda^{(L)} = 1$ as before.

3. Apply the two-site operator $\hat{u}_{j,j+1}$, with the matrix representation $u^{\sigma_j\sigma_{j+1}}_{\sigma'_j\sigma'_{j+1}}$, on the two-site wave function $\psi^{\sigma_j\sigma_{j+1}}$ to get

$$\tilde{\psi}^{\sigma_j\sigma_{j+1}} = \sum_{\sigma'_j\sigma'_{j+1}} u^{\sigma_j\sigma_{j+1}}_{\sigma'_j\sigma'_{j+1}}\psi^{\sigma_j\sigma_{j+1}}. \tag{3.64}$$

   See also figure 3.13.

4. Applying an unitary two-site operator on neighboring sites j, $j+1$ only requires updating the connecting Schmidt values $\lambda^{(j)}$ and the matrices on both sites Γ^{σ_j} and $\Gamma^{\sigma_{j+1}}$. Therefore, we extract the updated versions $\tilde{\lambda}^{(j)}$, $\tilde{F}^{\sigma_j}$ and $\tilde{F}^{\sigma_{j+1}}$ while keeping the old $\lambda^{(j-1)}$ and $\lambda^{(j+1)}$. We restore the Schmidt decomposition via SVD at the current bonds

$$\tilde{\psi}^{\sigma_j\sigma_{j+1}} = U^{\sigma_j}\tilde{\lambda}^{(j)}V^{\sigma_{j+1}\dagger}. \tag{3.65}$$

   Then $\tilde{\Gamma}^{\sigma_j}$ and $\tilde{\Gamma}^{\sigma_{j+1}}$ are extracted by dividing out the old Schmidt values $\lambda^{(j-1)}$ and $\lambda^{(j+1)}$

$$\tilde{\Gamma}^{\sigma_j} = (\lambda^{(j-1)})^{-1}U^{\sigma_j} \tag{3.66}$$

$$\tilde{\Gamma}^{\sigma_{j+1}} = V^{\sigma_{j+1}\dagger}(\lambda^{(j+1)})^{-1}. \tag{3.67}$$

   On the technical side, due to numerical inaccuracies this is actually done by computing the pseudoinverse of $\lambda^{(j-1)}$ respectively $\lambda^{(j+1)}$. This concludes the update for the current bond j, $j+1$. Move on to $j \to j+2$.

5. Repeat steps (2) to (4) while $j < N$ for all odd bonds.

6. After updating all odd bonds, switch to even bonds by setting $j = 2$ and repeating steps (2) to (4) while $j < N$ for all even bonds. This concludes one full Trotter time step. Repeat N times and measure as desired.

The graphical scheme of one Trotter step of the TEBD algorithm is outlined in figure 3.14.

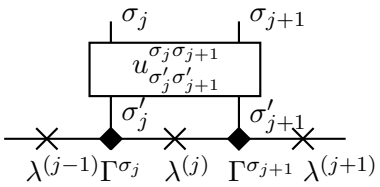

Figure 3.13: Application of $\hat{u}_{j,j+1}$ onto $\psi^{\sigma_j\sigma_{j+1}}$ during TEBD update.

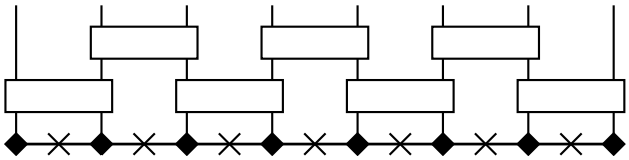

Figure 3.14: One full Trotter step.

3.4 Dynamical correlation functions

Green's functions belong to the most important tools available in many-body theory. They allow the classification of many-body systems and the calculation of expectation values via the KUBO formula. Furthermore, many important physical quantities, like the magnetical susceptibility, electrical conductivity or the dieelectric function, can be expressed as Green's function. Last but not least, some Green's functions are also directly accessible via spectroscopy experiments. A thorough introduction into the Green's function formalism can be found in e.g. [24].

Among the most important Green's functions are the retarded Green's function

$$G^{\text{ret}}_{AB}(t-t') = -i\Theta(t-t')\langle[A(t), B(t')]_{-\epsilon}\rangle, \tag{3.68}$$

and the spectral density

$$S_{AB}(t-t') = \frac{1}{2\pi}\langle[A(t), B(t')]_{-\epsilon}\rangle, \tag{3.69}$$

where A and B are arbitrary operators and $\Theta(t)$ is the Heaviside step function. The system we are considering is time-translational invariant therefore we can set without loss of generality $t' = 0$. Green's functions give the same information wether one uses commutators or anticommutators. For applications in fermionic systems it is advantagous to use the anticommutator versions of Green's functions. Therefore, we always set $\epsilon = -1$ in our applications. In the very common case that $S_{AB}(\omega)$ is real, the retarted Green's function and the spectral density are related simply by

$$-\pi S_{AB}(\omega) = \text{Im}G^{\text{ret}}_{AB}(\omega). \tag{3.70}$$

For our applications we will often have that $A^\dagger = B$ and hence above identity is true. The retarted Green's function and the spectral density are also related otherwise and their informative content is essentially equivalent. Therefore, we will focus on the spectral density only. We will discuss now on how to obtain the spectral density from the tools we already have available, that are DMRG and TEBD.

There are different ways of obtaining the spectral density using MPS. Some of the most prominent methods are the correction vector method [20], DDMRG [18] and Chebeychev expansion [17]. However, these methods have the disadvantage that each k-value, and for the correction vector and DDMRG method also each ω-value, has to be calculated separately with DMRG-like effort. Many separate runs are necessary for obtaining the entire spectrum. Obtaining the spectrum from the time evolution all k- and ω-values are calculated simultaniously from one (respectively four) time evolutions.

3.4.1 Spectral densities from TEBD

Equation (3.69) can be calculated straight forward from the time evolution. For the following discussion we will concentrate on the important case that the operators A and B are particle creation and annihilation operators i.e. $S_{aa^\dagger}$. We will call this special spectral density simply the spectrum. The spectrum can be directly compared to the noninteracting dispersion relations in figure 2.1. In the noninteracting case $S_{aa^\dagger}$ gives exactly the dispersions relations. We can expand the anticommutator in (3.69)

$$S_{aa^\dagger}(t) = \frac{1}{2\pi}\Big(\langle a(t)a^\dagger(0)\rangle + \langle a^\dagger(0)a(t)\rangle\Big) = \tilde{S}_{aa^\dagger}(t) + \tilde{S}_{a^\dagger a}(-t) \tag{3.71}$$

where we defined $\tilde{S}_{AB}(t) = \frac{1}{2\pi}\langle A(t)B(0)\rangle$. We will refer to $\tilde{S}_{aa^\dagger}$ as the electron part of the spectrum because it gives the electron excitations i.e. the part of the spectrum above the Fermi energy. Analogous we refer to $\tilde{S}_{a^\dagger a}$ as the hole part of the spectrum because the annihilation operator creates a hole in the system and it gives the part below the Fermi energy. Very often the Green's functions $G^{>}_{AB}(t)$ and $G^{<}_{AB}(t)$ are introduced for this purpose. They are related to $\tilde{S}_{AB}(t)$ by

$$\begin{aligned} G^{>}_{AB}(t) &= \langle A(t)B(0)\rangle = 2\pi\tilde{S}_{AB}(t), \\ G^{<}_{AB}(t) &= \langle B(0)A(t)\rangle = 2\pi\tilde{S}_{BA}(-t). \end{aligned} \tag{3.72}$$

We are more interested in the spectrum in the k, ω space. We can go there from real-space by a Fourier transform

$$\tilde{S}_{aa^\dagger}(k,\omega) = \sum_{j=-\infty}^{\infty} \exp(-ikj) \int_{-\infty}^{\infty} dt \exp(i\omega t)\tilde{S}_{cc^\dagger}(j,t) \tag{3.73}$$

with

$$\tilde{S}_{cc^\dagger}(j,t) = \frac{1}{2\pi}\langle 0| c_j(t)c_0^\dagger(0)|0\rangle = \frac{1}{2\pi}\langle 0| e^{iHt}c_j(0)e^{-iHt}c_0^\dagger(0)|0\rangle . \tag{3.74}$$

The operator $c_0^\dagger$ is applied in the middle of the system whereas c_j is applied on the j-th site. The steps for calculating (3.74) are as follows:

1. Obtain the ground state $|0\rangle$ of the system by DMRG.
2. Apply the operator $c_0^\dagger$ on the ground state $|0\rangle$

$$|\phi(0)\rangle = c_0^\dagger|0\rangle . \tag{3.75}$$

3. Do the real-time evolution using the TEBD algorithm

$$|\phi(t)\rangle = e^{-iHt}\,|\phi(0)\rangle\,. \tag{3.76}$$

4. The spectral function is obtained after a regular time interval Δt by calculating the overlap

$$\tilde{S}_{cc^\dagger}(j,t) = \langle 0|\, e^{iHt} c_j(0)\,|\phi(t)\rangle\,. \tag{3.77}$$

Since $\langle 0|$ is an eigenstate of e^{iHt} we can replace H by the eigenenergy E and simplify

$$\tilde{S}_{cc^\dagger}(j,t) = e^{iEt}\,\langle 0|\, c_j(0)\,|\phi(t)\rangle\,. \tag{3.78}$$

All of these steps can be implemented using the MPS language easily. From (3.73) it is clear that we also need $\tilde{S}_{cc^\dagger}(j,t)$ for negative times t. Fortunately, positive and negative times can be easily related. We start by taking the complex conjugate of the spectral density

$$\begin{aligned}\Big(\tilde{S}_{AB}(t)\Big)^* &= \frac{1}{2\pi}\Big(\langle e^{iHt}A(0)e^{-iHt}B(0)\rangle\Big)^* \\ &= \frac{1}{2\pi}\langle B^\dagger(0)e^{iHt}A^\dagger(0)e^{-iHt}\rangle \\ &= \frac{1}{2\pi}\langle e^{-iHt}B^\dagger(0)e^{iHt}A^\dagger(0)\rangle = \tilde{S}_{B^\dagger A^\dagger}(-t).\end{aligned} \tag{3.79}$$

In the case $A^\dagger = B$ this simply means that

$$\tilde{S}_{AB}(-t) = \Big(\tilde{S}_{AB}(t)\Big)^*, \qquad A^\dagger = B. \tag{3.80}$$

Therefore, it is not necessary to do a time evolution to negative times t.

For calculating the spectrum $S_{aa^\dagger}(k,\omega)$ for a spinless system we need two time evolutions: $\tilde{S}_{cc^\dagger}(j,t)$ and $\tilde{S}_{c^\dagger c}(j,t)$. In a system with spin degrees of freedom the spectrum can be calculated for each spin species separately and then added up in the end. In spin symmetric cases $S_{a_\uparrow a_\uparrow^\dagger}(k,\omega)$ and $S_{a_\downarrow a_\downarrow^\dagger}(k,\omega)$ give the same result. However, for the Hamiltonian (2.1) this is not the case and therefore we have to calculate both spin species. For the entire spectrum generally four time evolutions are needed

$$S_{\mathrm{tot}}(j,t) = \tilde{S}_{c_\uparrow c_\uparrow^\dagger}(j,t) + \tilde{S}_{c_\uparrow^\dagger c_\uparrow}(j,-t) + \tilde{S}_{c_\downarrow c_\downarrow^\dagger}(j,t) + \tilde{S}_{c_\downarrow^\dagger c_\downarrow}(j,-t). \tag{3.81}$$

By also calculating the off-diagonal elements $S_{c_\uparrow c_\downarrow^\dagger}(j,t)$ and $S_{c_\downarrow c_\uparrow^\dagger}(j,t)$ the spectral function for arbitrary spin directions can be calculated. The transformation is given below for the spin directions that are of interest to us:

$$
\begin{aligned}
S_{a_\uparrow a_\uparrow^\dagger} &= S_{a_\uparrow a_\uparrow^\dagger} \\
S_{a_\downarrow a_\downarrow^\dagger} &= S_{a_\downarrow a_\downarrow^\dagger} \\
S_{a_\rightarrow a_\rightarrow^\dagger} &= \frac{1}{2}(S_{a_\uparrow a_\uparrow^\dagger} + S_{a_\downarrow a_\downarrow^\dagger} + iS_{a_\uparrow a_\downarrow^\dagger} - iS_{a_\downarrow a_\uparrow^\dagger}) \\
S_{a_\leftarrow a_\leftarrow^\dagger} &= \frac{1}{2}(S_{a_\uparrow a_\uparrow^\dagger} + S_{a_\downarrow a_\downarrow^\dagger} - iS_{a_\uparrow a_\downarrow^\dagger} + iS_{a_\downarrow a_\uparrow^\dagger}) \\
S_{a_+ a_+^\dagger} &= \frac{1}{2}(S_{a_\uparrow a_\uparrow^\dagger} + S_{a_\downarrow a_\downarrow^\dagger} + S_{a_\uparrow a_\downarrow^\dagger} + S_{a_\downarrow a_\uparrow^\dagger}) \\
S_{a_- a_-^\dagger} &= \frac{1}{2}(S_{a_\uparrow a_\uparrow^\dagger} + S_{a_\downarrow a_\downarrow^\dagger} - S_{a_\uparrow a_\downarrow^\dagger} - S_{a_\downarrow a_\uparrow^\dagger})
\end{aligned}
\tag{3.82}
$$

where + and − are the eigenstates of the σ_x operator.

We will now try to apply this method on a noninteracting problem. The result is well known then, specifically we try to recreate figure 2.1 (c). Using above scheme the real time evolution is given in figure 3.15 (a). The absolute value of $S_{\text{tot}}(j,t)$ is given. We can already see two problems arising.

Firstly, the maximum time $t_{\max}$ is limited by the system size. If the time evolution reaches the boundary of the system it will be influenced by boundary effects. Therefore, one has to abort the simulation before it reaches the boundary. The result will still have the boundary effects from the ground state itself, although. Furthermore, $t_{\max}$ is also limited by computer time. Especially for strongly interacting systems the entanglement grows very fast with the time evolution calling for very high matrix dimensions m. Long time evolutions then simply get unfeasible.

The second problem arises from the Fourier transform. At the maximum simulation time $t_{\max}$ the simulated $S_{\text{tot}}(j,t)$ suddenly drops to zero. Sudden jumps usually result in a lot of ringing artefacts, known as Gibbs oscillations, after the Fourier transform. Therefore, a suitable window function should be used. The drawback of the window function is that it throws away calculated data and the result after the Fourier transform is significantly broadened. We used a Dolph-Chebyshev window with 100 dB of sidelobe attenuation for our application. Using this window function there is practically no ringing but the broadening is significant as one can see in figure 3.15 (b). The spin-orbit gap of size $\Delta^{\text{SO}} = B = 0.1$ is not at all discernible from a system with $\Delta^{\text{SO}} = B = 0$.

3.4.2 Linear prediction

This poor energy resolution is the main reason why so many alternative approaches to this problem have been developed. The method of extracting the spectra from the time evolution basically stayed a proof of concept without real applications. This changed in 2008, when White et. al proposed to use linear prediction for extrapolating the time series [42]. Later on this technique was applied to finite temperature simulations [2] and also found application in [27] and [35]. Applying this technique we can significantly improve our spectrum in figure 3.15 (c), where we used linear prediction for extrapolating the data until $\tilde{t}_{\max} = 11t_{\max}$. Also the spin-orbit gap is now resolved, although the spectrum has more broadening near the gap than elsewhere. One would expect a constant broadening because the exact spectrum consists only of Dirac delta peaks for noninteracting systems. The following presentation of linear prediction follows closely Martin Ganahl et al. [14].

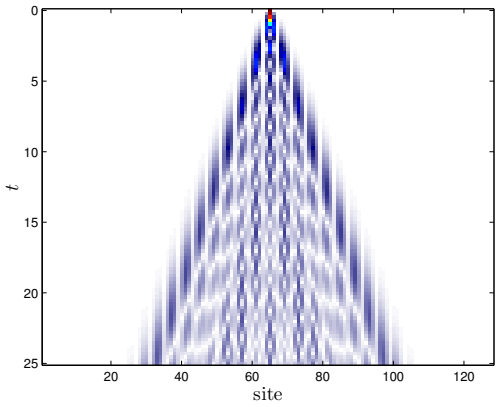

(a) $||S_{\mathrm{tot}}(j,t)||$

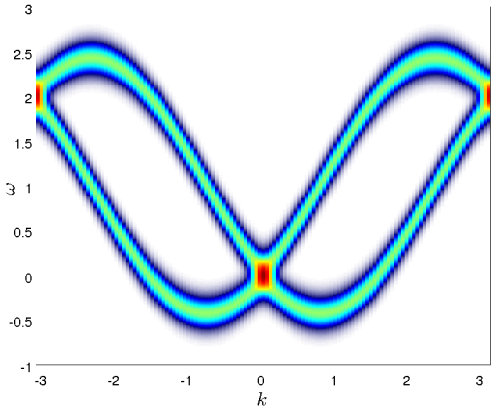

(b) Fourier transform and window function

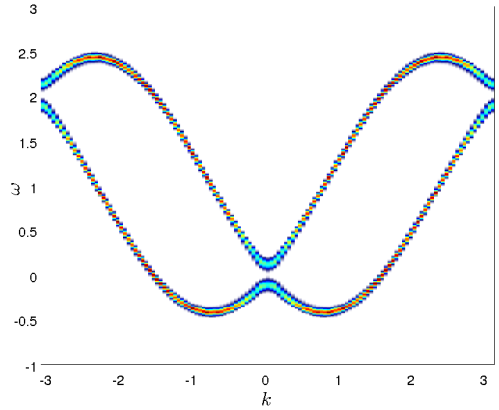

(c) Fourier transform and linear prediction

Figure 3.15

Linear prediction is a simple, yet powerful tool, for extrapolating a time series of equidistant data points. It is based on the ansatz that a data point x_n can be approximated by a fixed linear combination of the previous L data points:

$$x_n \approx \tilde{x}_n = -\sum_{j=1}^{L} a_j x_{n-j}. \tag{3.83}$$

The L coefficients a_j are fixed for all x_n. They are obtained by minimizing the least squares error

$$\mathcal{E} = \sum_{n=L+1}^{T} |\tilde{x}_n - x_n|^2, \tag{3.84}$$

using T known data points for the "training" of the coefficients a_j. The minimization condition $\nabla_{\vec{a}}\mathcal{E} = 0$ yields the following set of linear equations,

$$\begin{aligned} &R\vec{a} = -\vec{r}, \\ &R_{ij} = \sum_{n=L+1}^{T} x^*_{n-i} x_{n-j}, \qquad r_i = \sum_{n=L+1}^{T} x^*_{n-i} x_n, \end{aligned} \tag{3.85}$$

with $1 \leq i, j \leq L$. The coefficients $\vec{a}$ are then obtained by simply inverting the matrix $\vec{a} = -R^{-1}\vec{r}$. In general the time series won't be exact because of numerical errors. Therefore, the pseudoinverse with a cutoff δ is taken for inverting the matrx R. After the coefficients a_j have been calculated the time series can be extrapolated as

$$\tilde{x}_{L+k} = \sum_{j=1}^{L} \left[M^k\right]_{1j} x_{L+1-j}, \tag{3.86}$$

with the matrix

$$M = \begin{pmatrix} -a_1 & -a_2 & -a_3 & \dots & -a_L \\ 1 & 0 & 0 & \dots & 0 \\ 0 & 1 & 0 & \dots & 0 \\ \vdots & \ddots & \ddots & \ddots & \vdots \\ 0 & 0 & \dots & 1 & 0 \end{pmatrix}. \tag{3.87}$$

Reexpressing (3.86) by diagonalizing M yields,

$$M = U\lambda U^{-1}, \quad b_i = \sum_{j=1}^{L} U^{-1}_{ij} x_{L+1-j}, \quad \tilde{x}_{L+k} = \left[U\lambda^k \vec{b}\right]_1. \tag{3.88}$$

From the rightmost equation it is clear that the sequence of predicted data points will diverge if any $|\lambda_i| > 1$. This can happen because of numerical inaccuracies, or when the spectral function has some weight outside the intervall $[-1, 1]$. In these cases the eigenvalues can be either set to zero or renormalized to unity by $\lambda_i \to \frac{\lambda_i}{|\lambda_i|}$. The choice should not matter as long as the corresponding coefficient b_i is small. Usually, we set the eigenvalue to zero, but sometimes the prediction performed better with a renormalization of these λ_i. We will note these occasions.

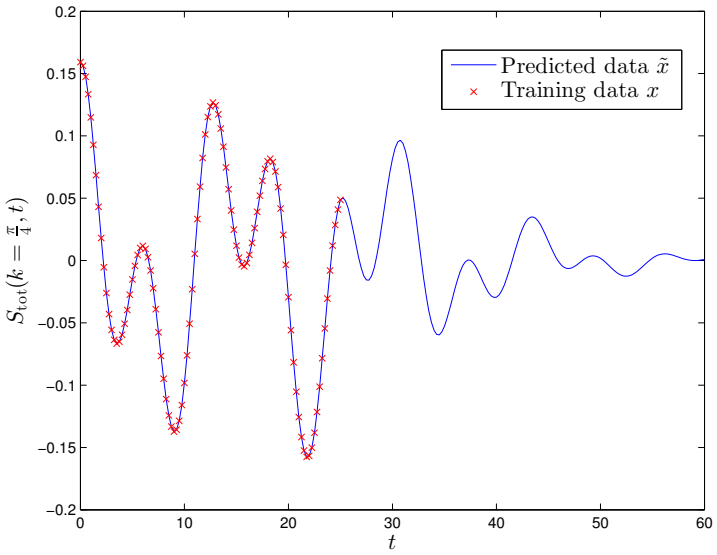

Figure 3.16: Data extrapolated by linear prediction.

From (3.88) it is also clear that the functional form of the predicted time series is simply a linear combination of damped exponential functions. This is a reasonable assumption because assuming this form after the Fourier transform the spectrum consists of a sum of Lorentzians.

The result of a typical linear prediction is shown in figure 3.16. Linear prediction is performed on the already spatially Fourier transformed spectrum $S(k,t)$. Then the time series has a simpler structure and the prediction works better. Generally, the data generated by linear prediction will be similar to the true time evolution, but not the same. We usually see the oscillations continued with the same frequency but at a stronger damping. However, it is appearantly good enough to drastically enhance the resolution of the spectrum. A quite large $\delta \approx 10^{-5} \ldots 10^{-3}$ for the pseudoinverse is typically choosen because of numerical errors.

3.5 Determination of the Luttinger Liquid Coefficients

A crucial point, for comparing microscopic models with their field theoretical Luttinger liquid counterparts, is the determination of the Luttinger liquid coefficients K_ρ and K_σ introduced in section 2.2. A reliable calculation of K_ρ and K_σ needs large enough system sizes to get into the vicinity of the thermodynamic limit. Some strategy to get rid of finite size effects is mandatory. Fortunately DMRG allows large enough system sizes to extract the Luttinger liquid coefficients directly from the correlations. We will use the method proposed by Ejima et. al [10]. A determination from ground and excited state energies is also possible [11]. We compared the two methods in appendix C.

3.5.1 Calculation of K_ρ

The Luttinger Liquid coefficient K_ρ dominates the long range behaviour of the density-density correlation function. For a spinless Luttinger liquid the asymptotic behaviour for $1 << r << L$ is given by

$$C^{\mathrm{NN}}(r) \sim -\frac{K_\rho}{2(\pi r)^2} + A\frac{\cos(2k_F r)}{r^{1+K_\rho}} \ln^{-\frac{3}{2}}(r) + ... \tag{3.89}$$

Following the discussion in section 2.2 we assume a spinless Luttinger liquid inside the 2 Fermi points phase and a spinful Luttinger liquid in the 4 Fermi point phase. The only difference for the spinful Luttinger Liquid is a factor of 2 in the first term of equation (3.89). As far as we know there are no results for $C^{\mathrm{NN}}(r)$ for spiral Luttinger liquids. Naively trying to fit (3.89) and then obtaining K_ρ from the fit works very bad. The asymptotic behaviour of $C^{\mathrm{NN}}(r)$ is difficult to obtain from the system sizes accessible with DMRG. Finite size effects from the boundaries influence also the result. The method presented below works surprisingly good under this circumstances.

The density-density correlation function is obtained by measuring

$$C^{\mathrm{NN}}(r) = \langle \hat{n}_r \hat{n}_0 \rangle - \langle \hat{n}_r \rangle \langle \hat{n}_0 \rangle. \tag{3.90}$$

First we start by taking the Fourier transform of the first term of (3.89)

$$\tilde{C}^{\mathrm{NN}}(q) = \sum_{r=-\frac{L}{2}}^{\frac{L}{2}} \exp(iqr)\ C^{\mathrm{NN}}(r) = \frac{K_\rho}{2\pi} q\,\mathrm{sign}(q) + \dots. \tag{3.91}$$

The second term of (3.89) is responsible for logarithmic corrections which vanish only very slowly with the system size. They are one of the reasons why it is so hard to extract the Luttinger liquid coefficients.

For spinless fermions the Luttinger liquid coefficient K_ρ can then be extracted from the derivative at $q = 0$ which corresponds to very long lengthscales:

$$K_\rho = 2\pi \lim_{q\to 0^+} \frac{\tilde{C}^{\mathrm{NN}}(q)}{q}. \tag{3.92}$$

For spinful fermions the corresponding formula is

$$K_\rho = \pi \lim_{q\to 0^+} \frac{\tilde{C}^{\mathrm{NN}}(q)}{q}. \tag{3.93}$$

In this work usually the form (3.92) for spinless fermions is assumed. Of course, this would give wrong results in the 4 Fermi point phase. We use the jump in K_ρ, however, for distinguishing between the 2 and 4 Fermi point phases.

However, it should be noted that the correct form of equation (3.89) is at the point of writing not known. Using the forms for spinless, respectively spinful fermions, is an assumption based on the idea that only the very vicinity near the Fermi points plays a role. Fortunately, we will find in section 4.4.1 that the quantities calculated this way behave very much like the Luttinger liquid coefficients. This method of extracting K_ρ is also compared to a method relying only on ground state energies and the energy of the first excited state in appendix C. The results agree reasonably well and the two methods are sufficiently different,

so we believe that the calculated K_ρ corresponds indeed to the Luttinger liquid coefficient. Nevertheless, the calculated quantities also proved to be very useful for distinguishing the different phases.

3.5.2 Calculation of K_σ

In section 2.2 we discussed that the spin degrees of freedom of a Luttinger liquid are described by a Hamiltonian of the same form as the charge degrees of freedom. Therefore the Luttinger liquid coefficient K_σ can be obtained by the same way than for the charge sector. A calculation yields K_σ from the derivative of the spin structure factor $\tilde{C}^{S^iS^i}(q)$ at $q = 0$ [16]:

$$K_\sigma = 4\pi \lim_{q\to 0^+} \frac{\tilde{C}^{S^iS^i}(q)}{q}. \tag{3.94}$$

Our system is anisotropically in spin and therefore K_σ depends on the chosen spin direction. Obtaining K_σ for the $\hat{S}^z$ direction gives another suitable criteria for differenciating the phases. If the system has a spin gap the coefficient K_σ should scale to zero and indeed it seems to do that inside of the spin-orbit gap for $\hat{S}^z$. For comparisons to the Luttinger liquid models in section 2.2 the $\hat{S}^y$ direction should be chosen.

Applying (3.94) on a system with spin-orbit coupling gives another problem. It turns out that $\tilde{C}^{S^iS^i}(q = 0)$ is generally not zero which is necessary for (3.94) to work. A calculation in the noninteracting system H_0 from (2.1) with $B = 0$ but nonzero α yields the spin-spin correlation functions

$$C^{S^xS^x}(r) = \langle \hat{S}^x_r \hat{S}^x_0 \rangle = \frac{1}{2L^2} \left(\sum_{|k|\le k_F} e^{ikr} \right) \left(\sum_{|k|>k_F} e^{-ikr} \right) \cos(2k_{\mathrm{SO}} r), \tag{3.95}$$

$$C^{S^yS^y}(r) = \langle \hat{S}^y_r \hat{S}^y_0 \rangle = \frac{1}{2L^2} \left(\sum_{|k|\le k_F} e^{ikr} \right) \left(\sum_{|k|>k_F} e^{-ikr} \right), \tag{3.96}$$

$$C^{S^zS^z}(r) = \langle \hat{S}^z_r \hat{S}^z_0 \rangle = \frac{1}{2L^2} \left(\sum_{|k|\le k_F} e^{ikr} \right) \left(\sum_{|k|>k_F} e^{-ikr} \right) \cos(2k_{\mathrm{SO}} r). \tag{3.97}$$

Because of $B = 0$ we don't need to subtract a constant magnetization. After a Fourier transform it turns out that equation (3.94) can only be applied onto $\tilde{C}^{S^yS^y}(q)$, for the other spin directions the structure factor doesn't vanish for $q = 0$, thus $\int dr\, C^{S^iS^i}(r) \neq 0$. Without the magnetic field B the S^y direction gives the "good" quantization axis. If the magnetic field is turned on the "good" quantization axis is k-dependent making matters even worse. Therefore, we adapt (3.94) to the circumstance $\tilde{C}^{S^iS^i}(q = 0) \neq 0$. By approximating $\frac{\partial \tilde{C}^{S^iS^i}(q)}{\partial q}|_{q=0}$ using Lagrangian interpolation we can generalize (3.94)

$$K_\sigma = L(-3C^{S^zS^z}(2\pi\frac{1}{L}) + 4C^{S^zS^z}(2\pi\frac{2}{L}) - C^{S^zS^z}(2\pi\frac{3}{L})). \tag{3.98}$$

Chapter 4

Results

4.1 Goals

The goals of this work are to identify the different phases of the system and how they are influenced by the interaction. Special attention was spent on the 2 and 4-Fermi point phases, for which a Luttinger liquid description is applicable. The first issue was to find observables for distinguishing the different phases. Then the properties, especially of the 2-Fermi point phase, were examined. The phase boundaries were surveyed for different parameter sweeps. Finally, breather bound states are observed and the results compared to field theoretical calculations. This chapter can be divided in five parts:

The first part of this chapter shows time evolutions for mostly noninteracting systems. The hope was to find easy criteria for distinguishing the 2 and 4-Fermi point phases. Although, this turned out not to be a very efficient method, some of the results are nonetheless interesting and therefore included here.

The second part can be seen as a further development of the time evolutions. Dynamical correlation functions were calculated, to obtain the interacting spectral densities. The spectra show all one needs to know to classify the system, however, the time evolutions are costly. The resolution is therefore limited by the maximum simulation time and the system size.

In the third part suitable observables for directly identifiyng the phase from the ground state were identified. The Luttinger liquid coefficients proved to be especially useful in this contex. The phase diagrams for 2 and 4 Fermi point phases were drawn here.

The fourth part finishes the phase diagram for quarter filling, by drawing the phase boundary to the mott phase.

In the fifth and last part we calculated the optical conductivity and compared the result to field theoretical calculations. The optical conductivity is dominated by breather bound states for repulsive interactions. The breathers were then observed separately in a time evolution after a suitable excitation.

Due to the large number of parameters we had to constrain our studies to the most interesting cases. In terms of interactions we concentrated at first only on on-site interaction U and then on a nearest neighbor interaction U' with a fixed ratio to U:

$$U' = \frac{U}{2}. \tag{4.1}$$

The motiviation for this choice of U' is to keep the backscattering coefficient

$$g_{1\perp} = V(q = 2k_{\mathrm{F}}) \tag{4.2}$$

small [1]. This makes comparisons to Luttinger liquid results easier because the backscattering term leads to logarithmic corrections that are usually not included in analytical results. For our interaction we can write the backscattering coefficient as

$$g_{1\perp} = U + 2U' cos(2k_{\mathrm{F}}), \tag{4.3}$$

and hence the condition $g_{1\perp} = 0$ leads to

$$U' = -U/[2cos(2k_F)]. \tag{4.4}$$

Most of the simulations where done for quarter filling. Since inside the spin-orbit gap there is a simple relationship between the filling n and the Fermi momentum: $k_{\mathrm{F}} = n\pi$. Therefore, for quarter filling and inside the spin-orbit gap (the 2 Fermi point phase) the above condition boils down to $U' = U/2$. We will use this nearest neighbor interaction throughout our whole work, whenever we don't confine us only to an on-site interaction.

For our simulations the computer code developed by Martin Ganahl is used. It contains efficient implementations of the two site DMRG and the TEBD algorithm, with the ability to preserve the total particle number and the total spin if applicable. Only very minor modifications to the TEBD code were necessary to make it applicable to the calculation of spectral densities. In general, the librarys of Martin Ganahl have ample functionality for manipulating MPS's and MPO's. We gladly used this functions in our computer code. The simulations were carried out either on local machines or the D-Cluster which belongs to Graz University of Technology and University of Graz.

4.2 Time evolutions

Due to the nontrivial shape of the dispersion relations (see figure 2.1 (c)) of our system, even the noninteracting physics has some surprising properties. In this chapter we looked at the time evolution after single-particle excitations for probing the dispersion relations.

4.2.1 Measurements

After a certain number of Trotter steps measurements are performed on the system. In most of our applications a Trotter step fo $\tau = 0.05$ is sufficient for keeping the error from the Suzuki-Trotter expansion small. Quite generally, we performed a number of measurements on the time evolved state.

We measured the spin-dependent particle densities $n_\uparrow = c_\uparrow^\dagger c_\uparrow$, $n_\downarrow = c_\downarrow^\dagger c_\downarrow$, $n_\rightarrow = c_\rightarrow^\dagger c_\rightarrow$, $n_\leftarrow = c_\leftarrow^\dagger c_\leftarrow$, $n_+ = c_+^\dagger c_+$ and $n_- = c_-^\dagger c_-$ with $c_+^\dagger = \frac{1}{\sqrt{2}}(c_\uparrow^\dagger + c_\downarrow^\dagger)$ and $c_-^\dagger = \frac{1}{\sqrt{2}}(c_\uparrow^\dagger - c_\downarrow^\dagger)$.

Also the expectation values of the spin operators $\hat{S}^x$, $\hat{S}^y$, $\hat{S}^z$ were measured. Another measurement, that is easily accessible in the MPS language, is the entanglement entropy. The truncated weight, which is useful for error estimations, was also logged.

Also the current density operator j was measured. One has to be careful not to naively use the current density from e.g. the Hubbard model. Because of the spin-orbit coupling the form of j changes quite a bit. Usually, only the kinetic energy hopping H_t contributes to the current density. In our system also the hopping in the spin-orbit coupling term H_SO has a contribution.

For a derivation of the current density operator, one has to find the j which together with $n = n_\uparrow + n_\downarrow$ satisfies the continuity equation

$$(j_{l+\frac{1}{2}} - j_{l-\frac{1}{2}}) + \frac{\partial n_l}{\partial t} = 0. \tag{4.5}$$

From the continuity equation and the Heisenberg equation of motion $\frac{\partial n_l}{\partial t} = i[H, n_l]$ follows then a recursion relation for the current density operator [38]

$$j_{l-\frac{1}{2}} = j_{l+\frac{1}{2}} + i[H, n_l]. \tag{4.6}$$

For open boundary conditions $j_{L+\frac{1}{2}} = 0$ can be used. The current density operator j can then be calculated by evaluating the commutator e.g. in the z-base

$$\begin{aligned} j_{l+\frac{1}{2}} =& i[-\frac{t}{2}\sum_\sigma (c_{l\sigma}^\dagger c_{l+1\sigma} - c_{l+1\sigma}^\dagger c_{l\sigma}) + \\ & \frac{\alpha}{2}(c_{l\downarrow}^\dagger c_{l+1\uparrow} - c_{l+1\uparrow}^\dagger c_{l\downarrow} - c_{l\uparrow}^\dagger c_{l+1\downarrow} + c_{l+1\downarrow}^\dagger c_{l\uparrow})]. \end{aligned} \tag{4.7}$$

The first term is the usual Hubbard model current density coming from the tight-binding kinetic energy. The second term is the contribution from the spin-orbit coupling. A side effect of the spin-orbit coupling, combined with the magnetic field, is that, due to the mixing of the spin directions, a simple current operator for only one spin species can't be given. The recursion relation (4.6) simply doesn't cancel in this case.

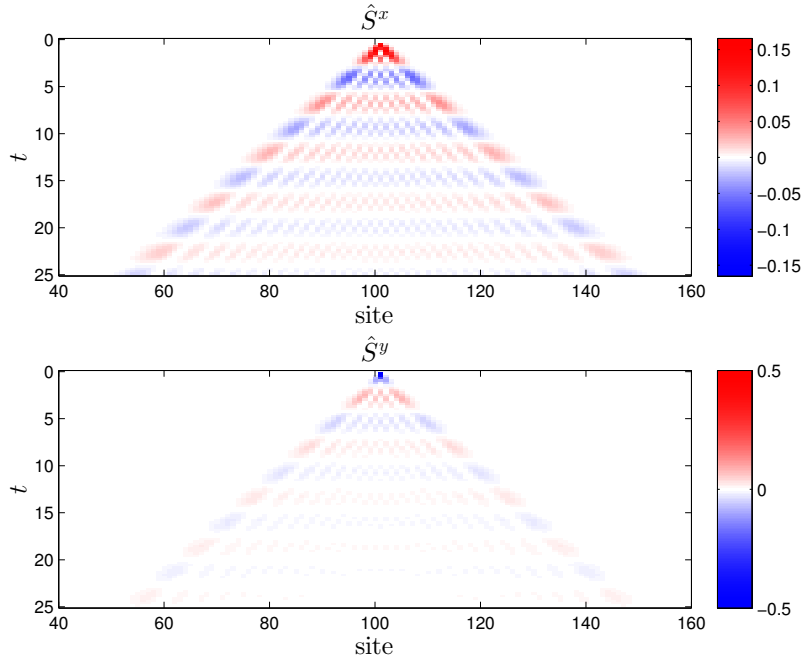

Figure 4.1: Single particle created $c^\dagger_{\leftarrow}$ in the middle of an empty system for $\alpha = 0,\ B = 0.3$. Measured are the spin operators $\hat{S}^x$ and $\hat{S}^y$.

4.2.2 Localized single particle excitations

Generally, one can learn a lot of a system by looking at the time evolution after a localized single particle excitation. The spectral density is basically obtained this way.

Without interactions and without a spin-orbit coupling α and only a magnetic field B we can observe a oscillation after the right kind of excitation (see figure 4.1 and 4.2). This oscillation is also known as Lamour precission and for observing it one only has to take care that the excitation acts on both branches of the dispersion relation. From figure 2.1 (a) we see that a magnetic field causes a Zeeman splitting between the spin $\uparrow$ and $\downarrow$ branch. Therefore, we have to excite in a direction transversal to the z direction. The frequency of this oscillations is directly related to the energy gap introduced by the magnetic field $\omega = 2\Delta^B = 2B$. In figure 4.1 and 4.2 we compare this oscillations for two different magnetic field strengths after an excitation $c^\dagger_{\leftarrow}$.

The effect of the spin-orbit coupling alone, without a magnetic field, is simply that the dispersion relations get shifted in k-space by k_{SO} dependent on the spin direction, like in figure 2.1 (b). Since a localized single particle creation is constantly spread out in k-space this gives exactly the same result as with $\alpha = B = 0$, see figure 4.3. Again we did an $c^\dagger_{\leftarrow}$ excitation.

If both the spin-orbit coupling and the magnetic field are turned on, the time evolution exhibits some assymmetric features. Again we are looking at the system after a $c^\dagger_{\leftarrow}$ excitation and observe the densities $n_\uparrow$ and $n_\downarrow$ in figure 4.4. We can clearly see that the time evolution is not symmetric anymore. This can be understood from the corresponding dispersion relation in figure 4.5. A spin $\leftarrow$ particle is created in the center of the system. Therefore, the biggest

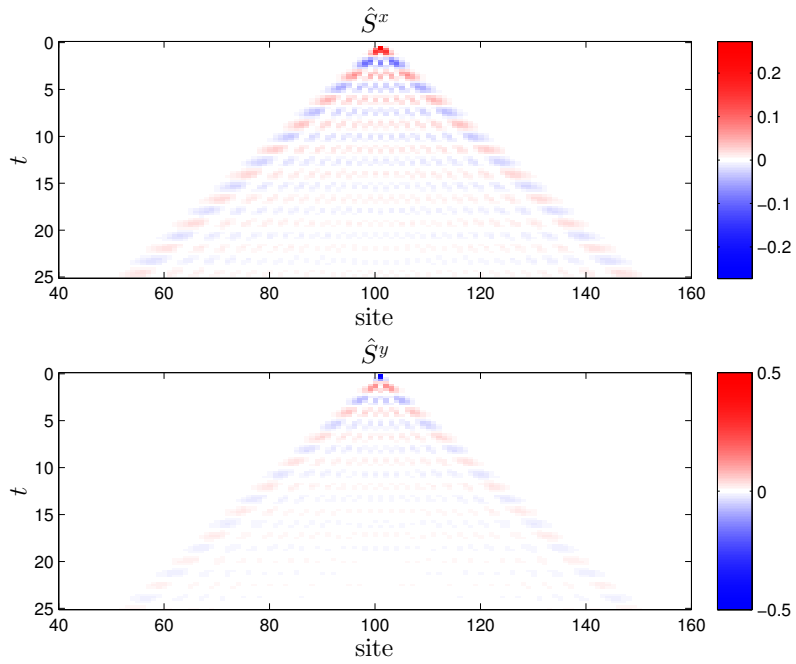

Figure 4.2: Single particle created $c^\dagger_{\leftarrow}$ in the middle of an empty system for $\alpha = 0,\ B = 0.6$. Measured are the spin operators $\hat{S}^x$ and $\hat{S}^y$.

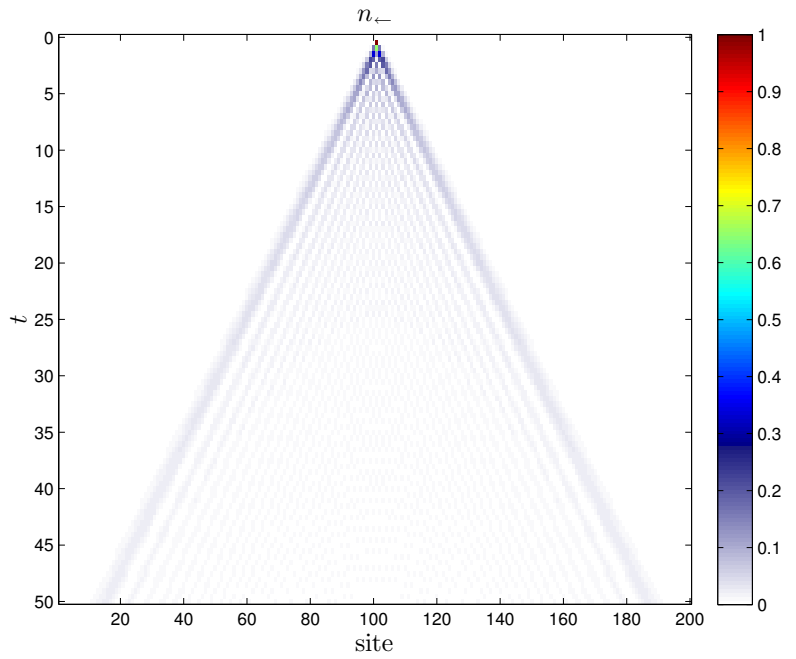

Figure 4.3: Single particle created $c^\dagger_{-}$ in the middle of an empty system for $\alpha = 1.5,\ B = 0$. Measured is the particle density n_{-}.

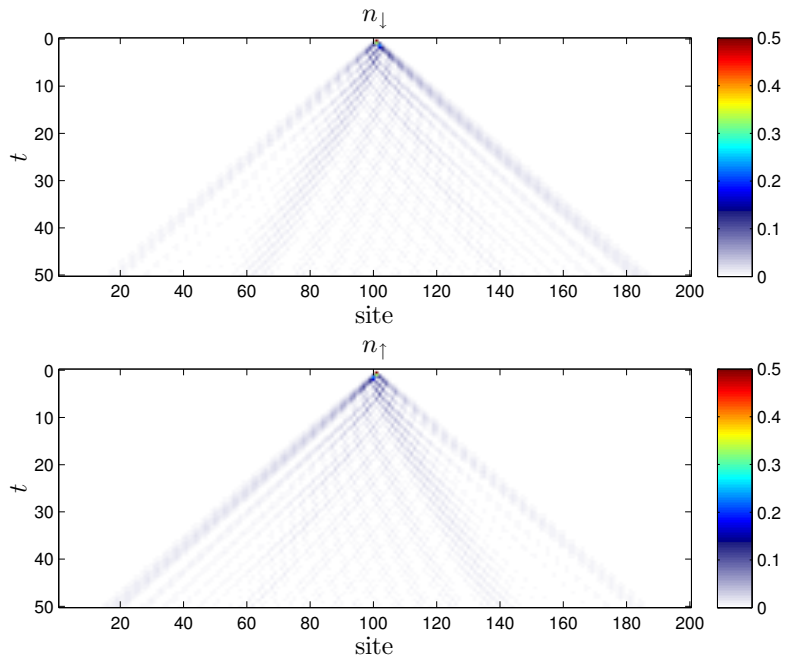

Figure 4.4: Single particle created $c^\dagger_-$ in the middle of an empty system for $\alpha = 1.5,\ B = 0.3$. Measured are the particle densities $n_\downarrow$ and $n_\uparrow$.

contribution comes from the left looking arrows in the dispersion relation. The lower spin $\leftarrow$ branch, on the right hand side, has more spin $\downarrow$ contributions than $\uparrow$ and a positive velocity. The upper spin $\leftarrow$ branch, on the left hand side, has more spin $\uparrow$ contributions than $\downarrow$ and a negative velocity. Hence, the signal in $n_\uparrow$ has more left-moving parts and the signal in $n_\downarrow$ has more right-moving parts. The second signal, with the opposite velocity, comes from the parts of the dispersion relation on the opposite side of the kinks at $\pm k_{\mathrm{SO}}$ and $\pm(\pi - k_{\mathrm{SO}})$. However, the overall particle density is still perfectly symmetric. For having a netto current in one direction, one has to go to partially filled systems, or do more complicated excitations that act only on a specific part of k-space.

4.2.3 Gaussian excitatons

Single particle creation operators on a specific site act evenly distributed in the whole k-space. It is much easier to learn something about the dispersion relation if the excitation is limited to a specific portion of k-space. This could be achieved by using momentum eigenstates as excitation operators. However, momentum eigenstates are instead evenly distributed in real space, which can make the interpretation of the measurements, that are done in real space, cumbersome.

Gaussian excitations provide a compromise between these two extremes. A gaussian wave packet has a finite width in real and in momentum space. Especially, they allow to excite specific k-values and therefore they allow a more direct interpretation of the results. A gaussian excitation with a specific k-value is applied using the operator [12]

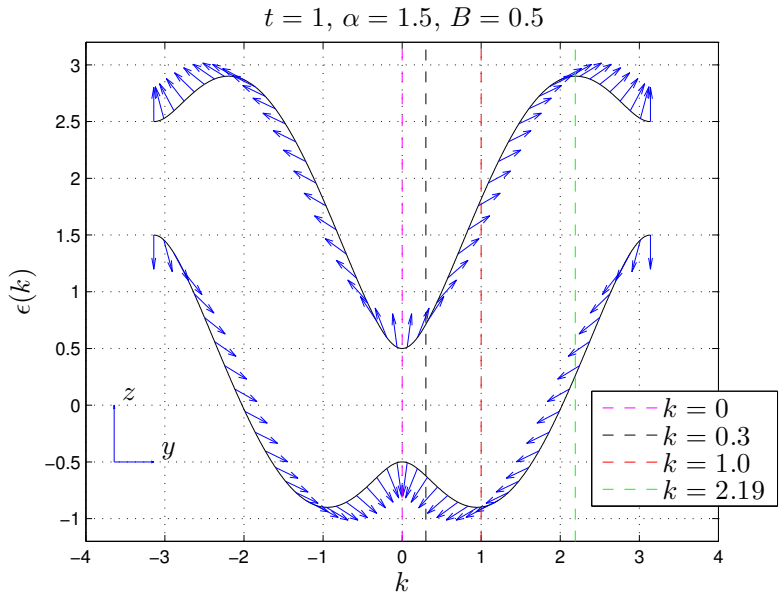

Figure 4.5: Dispersion relation for $\alpha = 1.5$ and $B = 0.5$.

$$\sum_x \exp(-\frac{(x-x_0)^2}{2\tilde{\sigma}^2}) \exp(i(x-x_0)k) c^\dagger_{x\sigma}. \tag{4.8}$$

The MPS state has to be normalized after the application of (4.8) anyway. Therefore, the normalization factor has been omitted. If nothing else is mentioned we use a Gaussian excitation with $\tilde{\sigma} = 4$, which corresponds to a width of $\sigma = 0.25$ in k-space.

Doing a gaussian excitation $c^\dagger_+$ at $k = 0$ in an empty system yields some surprising results at first sight. In figure 4.6 is the total density $n = n_\uparrow + n_\downarrow$ given and figure 4.7 shows the current density j and the expectation value of the spin operator $\hat{S}^y$. Looking at $\hat{S}^y$ we see some kind of Lamour precession which comes from the energy gap at $k = 0$ (see also figure 4.5). The initial spin looks in the + direction, the $+\frac{1}{2}$ eigenstate of the $\hat{S}^x$ operator. During the time evolution the spin starts to precess in the xy-plane due to the magnetic field. Surprisingly, this precission is also visible in the total density in figure 4.6. A zigzag movement of the particle with the frequency of precession is visible. Also the current density j in figure 4.7 shows very clear the zigzag movement. Comparing j with $\hat{S}^y$ we observe that a positive current (right-moving) corresponds to a spin $\leftarrow$ particle and a negative current (left-moving) corresponds to a spin $\rightarrow$ particle. This is due to the helical spin properties of the system, the spin direction is coupled to the direction of movement. An oscillation in the spin direction (due to the magnetic field) translates directly to an oscillatory movement in real space.

From equation (2.8) we know the spin eigenstates that correspond to a specific k-value. One just has to diagonalize the matrix for a given k and then the eigenvectors correspond to the wanted spin eigenstates. By doing an excitation in a spin eigenstate it is possible to excite only one of the two branches in the dispersion relation. Figure 4.8 is an example of a gaussian excitation with $k = 0.3$, where the total particle density n is plotted for an excitation on exclusively the upper branch, respectively the lower branch. The dispersion

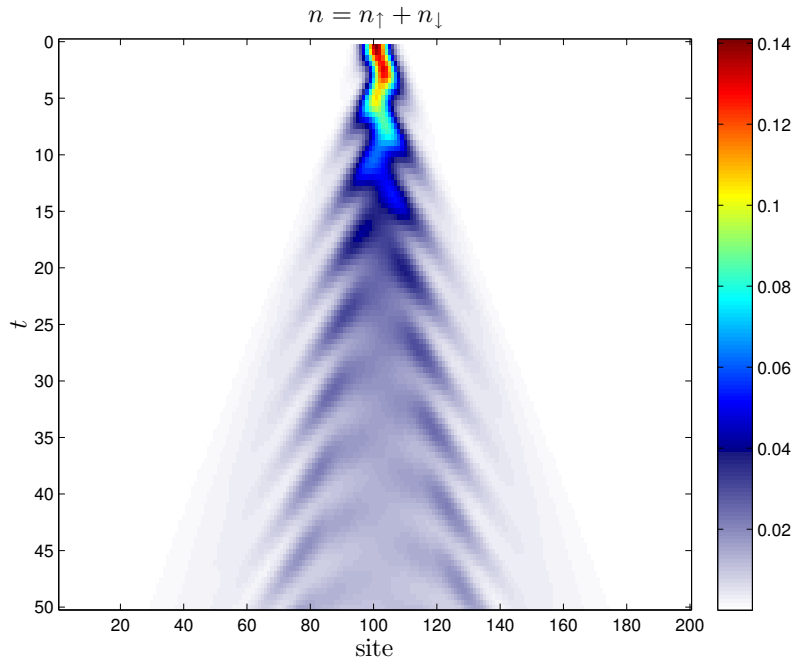

Figure 4.6: Gaussian $c^\dagger_{\uparrow_x}$ excitation with $k = 0.0$ in an empty system with $\alpha = 1.5,\ B = 0.5$. Measured is the total particle density $n = n_\uparrow + n_\downarrow$.

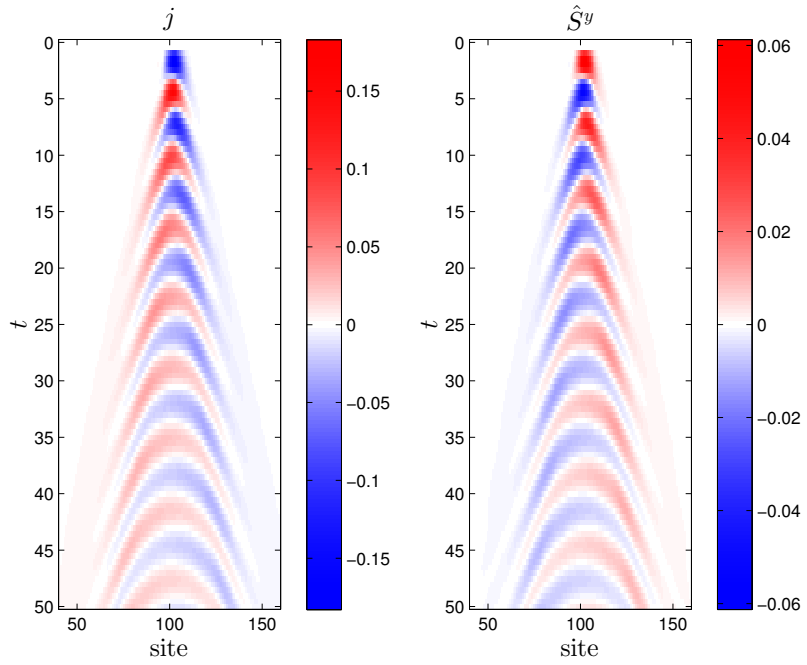

Figure 4.7: Gaussian $c^\dagger_{\uparrow_x}$ excitation with $k = 0.0$ in an empty system with $\alpha = 1.5,\ B = 0.5$. Measured are the current j and $\hat{S}^y$.

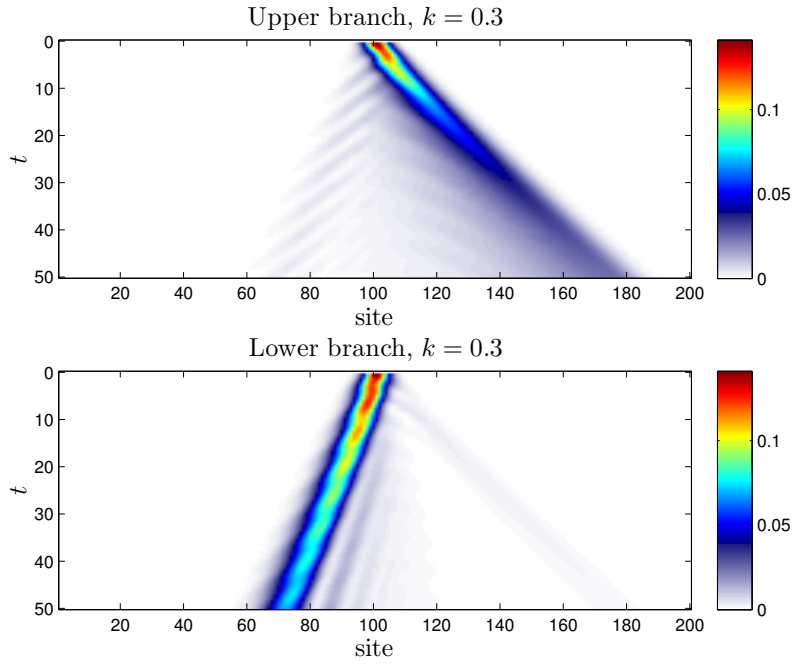

Figure 4.8: Gaussian $c^\dagger$ excitation with $k = 0.3$ in an empty system with $\alpha = 1.5,\ B = 0.5$. The spin directions of the excitations are such that they act solely on the upper respectively lower branch of the dispersion relation only. Measured is the particle density $n = n_\uparrow + n_\downarrow$.

relation 4.5 has the specific k-values indicated and also the spin directions on each branch. At $k = 0.3$ the upper branch has a positive slope and the lower branch a negative slope. Therefore, the the two excitations move in opposite directions.

In figure 4.9 we have the same but for $k = 1$. Here the lower branch has a minimum, therefore the corresponding excitation is stationary, whereas on the upper branch the excitation moves to the right.

At $k = 2.19$ the upper branch has a maximum, therefore the corresponding excitation in figure 4.10 is stationary.

4.2.4 Effect of an additional Cooper pairing field

Now we turn our focus again on the system from section 2.1.4. We use parameters based on the system researched by Stoudenmire et. al in [36]. The dispersion relations without and with the Cooper pairing field Δ^{C} are shown in figure 2.3 (a) respectively (b).

We start again in an empty system without the Cooper pairing field in figure 4.11. The corresponding dispersion relation is in figure 2.3 (a). We look at the spin dependent densities $n_\uparrow$ and $n_\downarrow$ after a gaussian excitation for three different k-values $k = 0,\ k = 0.3$ and $k = 1.5$. The excitation is in the spin + direction and because it is orthogonal to the magnetic field B, therefore we can observe Lamour precession. Because of the spin-orbit coupling this oscillation in spin-space is translated into an oscillatory movement in real space, like in figure 4.6. Away from $k = 0$, due to the spin-orbit coupling, the plane of precession is not anymore the xy-plane but also has a z-component. Therefore, we can see the precession

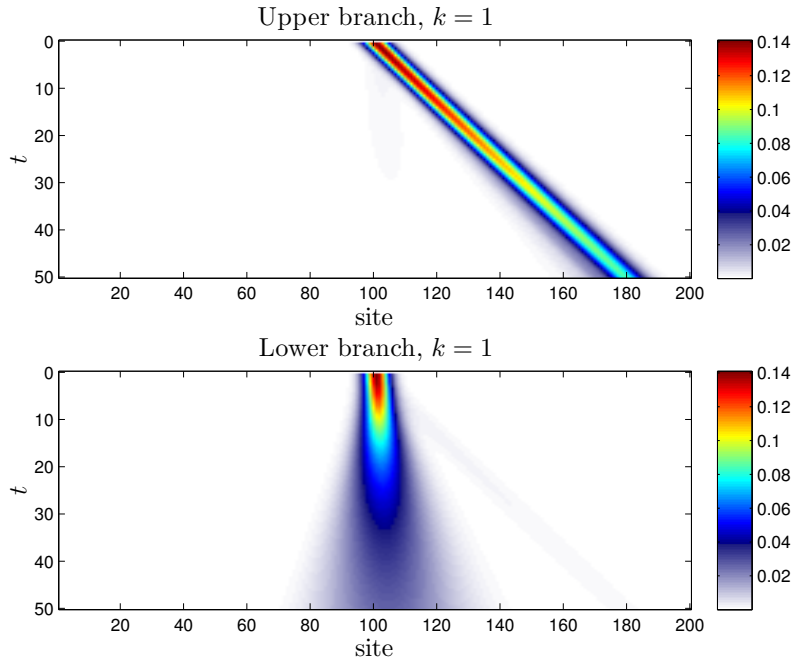

Figure 4.9: Gaussian $c^\dagger$ excitation with $k = 1$ in an empty system with $\alpha = 1.5,\ B = 0.5$. The spin directions of the excitations are such that they act solely on the upper respectively lower branch of the dispersion relation only. Measured is the particle density $n = n_\uparrow + n_\downarrow$.

directly in the $n_\uparrow$ and $n_\downarrow$ densities.

For the next time evolution we start with a partially filled system, corresponding to $\mu = 0$ in 2.3 (a), in figure 4.12. The system is still without a Cooper pairing field. We use a very small interaction $U = 0.1$. However, the interaction effects are negligible when compared to noninteracting systems. All other parameters are the same as above. We see that for $k = 0$ and $k = 0.3$ there is little to no signal in $n_\downarrow$. This is because these states are mostly filled, therefore the creation operator has no effect there. Because only one of the two energy levels are accessible, the Lamour precission, and also the zigzag movement, is inhibited. For $k = 1.5$ both branches are above the chemical potential, so we see the same as in figure 4.11.

Finally, we supplement the system above with the Cooper pairing field Δ^{C} in figure 4.13. The parameters are the same as in Stoudenmire et al. [36]. The system is now in a topologically nontrivial phase. We can understand what happens by looking at the corresponding dispersion relation in figure 2.3 (b). The Cooper pairing field opens up an energy gap at $\omega = \mu = 0$ of the size $2\Delta^{\mathrm{C}}$. The momentum eigenstates near this gap are of mixed particle-hole character. Therefore, a particle excitation at $k = 0$ acts on both the upper and lower branch. By the same arguments that lead to Lamour precession there are now oscillations in particle-hole space taking place. They are clearly visible for $k = 0$ and $k = 0.3$ with a frequency corresponding to the energy gap. Because the gap opened by the Cooper pairing field is smaller than the gap from the magnetic field the period of this oscillation is much larger. Also note that there is now a negative (hole-like) signal in the $n_\downarrow$ channel, which wasn't there before. For $k = 1.5$ the situation is again very similar to the two cases before.

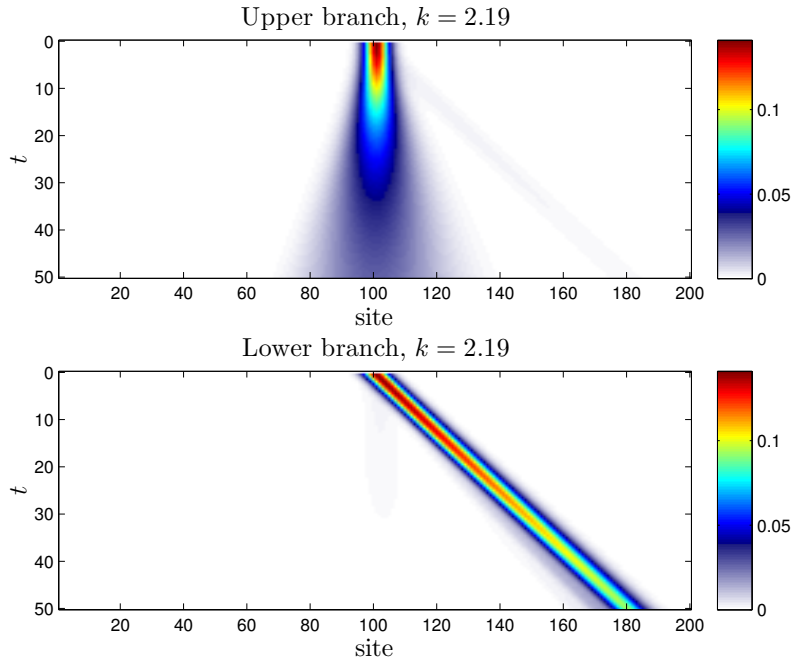

Figure 4.10: Gaussian $c^\dagger$ excitation with $k = 2.19$ in an empty system with $\alpha = 1.5,\ B = 0.5$. The spin directions of the excitations are such that they act solely on the upper respectively lower branch of the dispersion relation only. Measured is the particle density $n = n_\uparrow + n_\downarrow$.

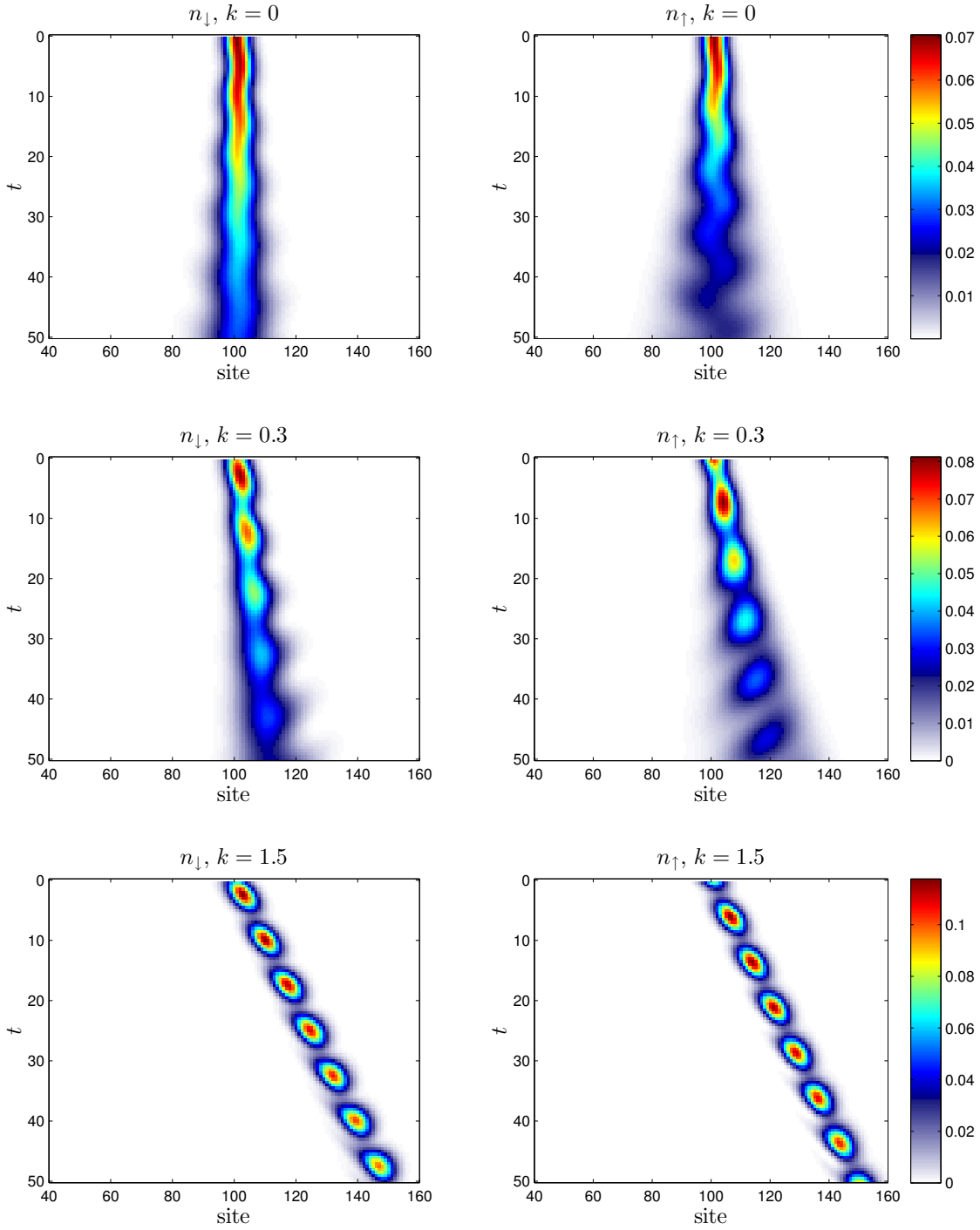

Figure 4.11: Gaussian $c_+^\dagger$ excitaton in the in an empty system for three different k-values ($k = 0,\ k = 0.3,\ k = 1.5$) with $\alpha = 0.3,\ B = 0.3,\ U = 0,\ \Delta^{\mathrm{C}} = 0$.

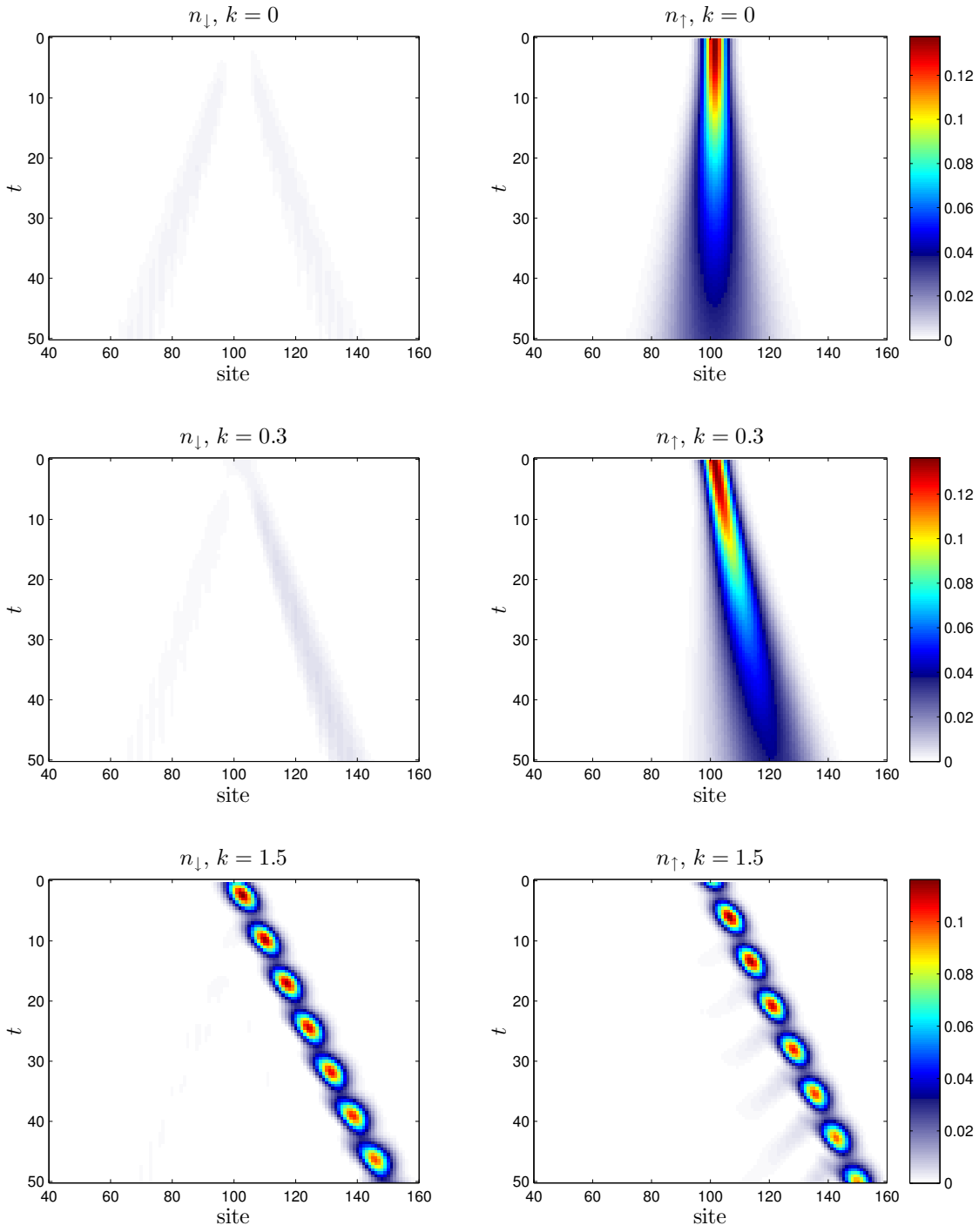

Figure 4.12: Gaussian $c_+^\dagger$ excitaton in the groundstate of a filled system, corresponding to $\mu = 0$, for three different k-values ($k = 0,\ k = 0.3,\ k = 1.5$) with $\alpha = 0.3,\ B = 0.3,\ U = 0.1,\ \Delta^{\mathrm{C}} = 0$. The background was subtracted.

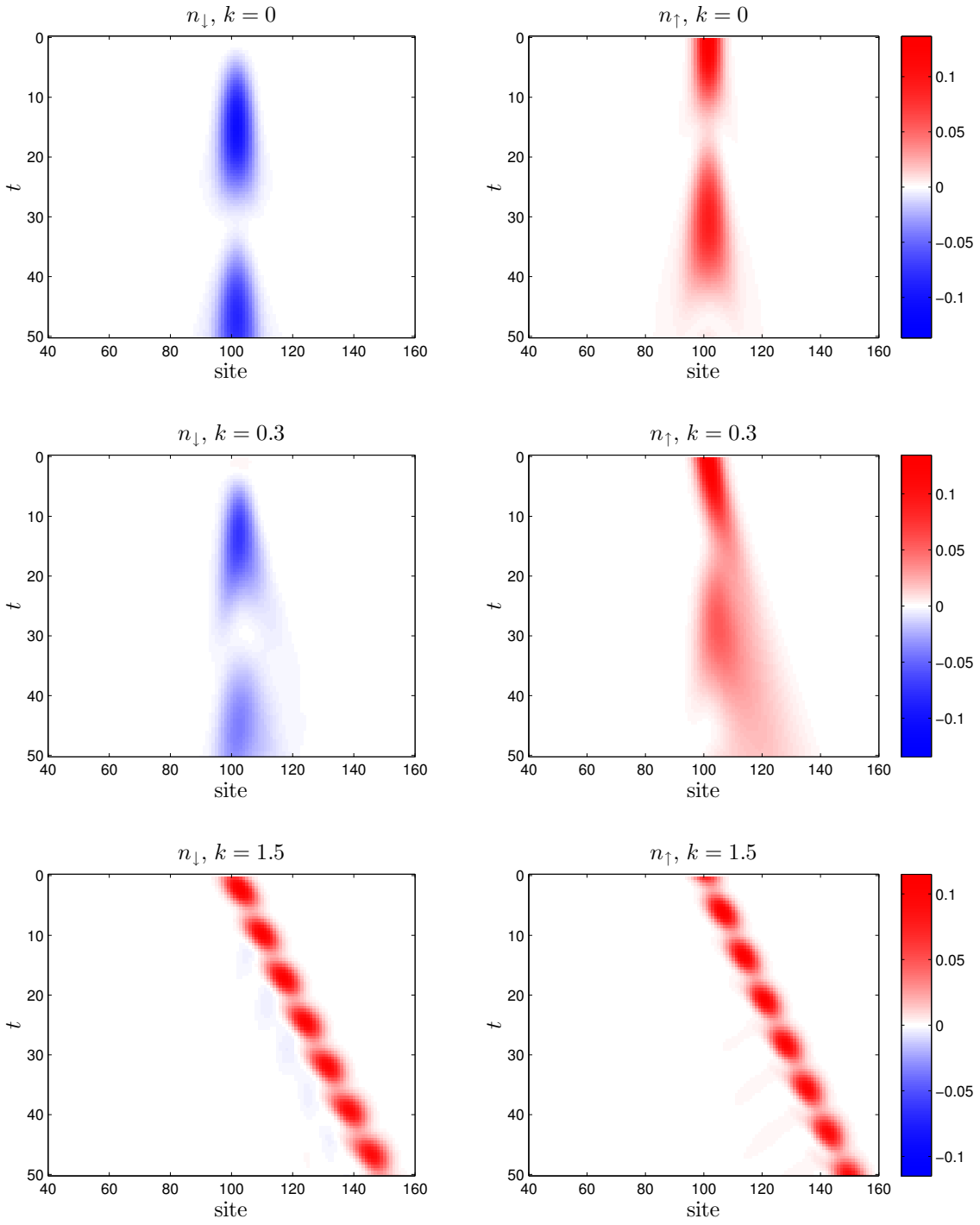

Figure 4.13: Gaussian $c_+^\dagger$ excitaton in the groundstate of a filled system for three different k-values ($k = 0,\ k = 0.3,\ k = 1.5$) with $\mu = 0,\ \alpha = 0.3,\ B = 0.3,\ U = 0.1,\ \Delta^{\mathrm{C}} = 0.1$. Due to the Cooper pairing field Δ^{C} additional electron-hole oscillations are visible for $k = 0$ and $k = 0.3$. The system is inside a topologically nontrivial phase. The background was subtracted.

4.3 Calculation of spectral densities from the time evolution

The spectral densities give very important insights in the system investigated here. They are the natural extension of the noninteracting dispersion relations to interacting systems. One particle excitations, that had a precise energy beforehand, are now transformed into collective charge (holon) and spin (spinon) excitations. Also various new types of excitations will emerge due to the interaction. The spectral densities give a very vivid picture about the properties and the current phase of the system. A comparison of the calculation of the spectral density from the time evolution to DDMRG, as well as a discussion of convergence and some technical details are given in appendix B.

4.3.1 Interaction effects on the spectral densities

Now we want to look at the evolution of the system from very weak interactions to very strong interactions. DMRG provides the perfect basis for such a study since the high quality of the results doesn't depend very strongly on the strength of the interaction. In general, the convergence gets even better with stronger interactions. For TEBD this is another story, although. Strong interactions lead to a high entanglement making the time evolution computationally expensive. Throughout this section we use a system size of $L = 128$ and calculated the time evolution up to $t_{\max} = 25$. For the truncation procedure we used a maximum matrix dimension of $m = 1200$. The total cumulative truncated weight ϵ_{tot} is the sum of all truncated weights during the whole simulation. We found that it depends strongly on the strength of the interaction. In most cases we managed to keep it below $\epsilon_{\text{tot}} = O(0.01)$. The worst case scenario was for $U = 6$ and $U' = 3$ where the total cumulative truncated weight reached $\epsilon_{\text{tot}} = 0.25$. However, the small deviation in the norm of the spectral density (smaller than 10^{-4}) and the analyisis in appendix B indicate us that the results are nevertheless reliable.

The interacting spectral densities are given in figure 4.14 and 4.15. Both show the evolution of the system from small to strong interaction strengths, but figure 4.14 has only an on-site interaction whereas for figure 4.15 there is also a nearest neighbour interaction with $U' = U/2$. For reference, the noninteracting spectral density is given in figure 2.1 (c) and the numerical result in figure 3.15 (c). At $k = 0$ we extracted the size of the spin-orbit gap directly from the spectra. We also did a separate calculation of the single-particle excitation gap defined as

$$\Delta_L^1 = E(L, N+1) + E(L, N-1) - 2E(L, N). \tag{4.9}$$

In the thermodynamic limes, and in the absence of pairing effects, the single-particle excitation gap (as the two-particle excitation gap) is the same as the charge gap. We indicated both gaps in the spectra with the single-particle excitation gap at $k = k_{\text{F}} = \frac{\pi}{2}$ and the spin-orbit gap at $k = 0$. The single-particle excitation gap is only visible for the strongest interaction in figure 4.15. The behaviour of these two gaps, as a function of the interaction, is also plotted in figure 4.16.

First let us start by confining the interaction to an on-site term in figure 4.14. The two main branches of the dispersion relation keep its general shape in the interacting spectral densities until the strongest interaction $U = 6$. Besides the broadening of the energies two other changes are visible for the two main branches: they get get shifted upwards to higher energies and the spin-orbit gap gets enhanced. The enhancement of the spin-orbit gap is

also shown in figure 4.16. Furthermore, we see that the main line of the lower branch seems to split into two lines at $k \approx \pm 2$. Above the two main branches an upper Hubbard band begins to emerge and moves quickly to higher energies. Below the two main branches an interesting new structure emerges. We suspect it to be the collective spin (spinon) excitations. Similarities to the ordinary Hubbard model become visible in the gauge transformed basis showed in figure 4.21.

Turning on the nearest neighbour interaction $U' = U/2$, in addition to the on-site interaction, has rather dramatic effects on the spectra. The spectral densities change their shape significantly with the interaction. The two main branches get stretched to a broader energy range and the bow at $k = 0$ on the lower branch gets straightened out. Both of these effects lead to a significantly enhanced spin-orbit gap at $k = 0$, see again figure 4.16. The lines seem to broaden more quickly than before. The splitting of the lower branch into two branches at $k \approx 2$ is still there. The upper Hubbard band is too weak, therefore it perishes besides the stretched spectrum. The peculiar structure below the two main branches emerges here faster with the interaction, besides that it looks the same as before. From $U = 4$ onwards a charge gap begins to open at the Fermi energy, due to the Mott phase which emerges here. We have indicated the size of the charge gap by the single-particle excitation gap. At $U = 6$ the origin of the spectral density from the noninteracting dispersion relation is hardly visible. The interaction transforms the system to a point where momentum eigenstates are not a very useful concepts.

Figure 4.16 shows the size of the partial gap and the single particle excitation gap as a function of U as already seen in figure 4.14 and 4.15. It shows distinctly that the spin-orbit gap is enhanced much more in the case of nonzero U'. Since the spin-orbit gap is only a partial gap it doesn't make sense if the system is wholly gapped, nevertheless the measured values at $U = 4$ and $U = 5$ for $U' = U/2$ are given for completeness.

Quite generally, we can say that that interaction effects are more dramatic with finite range interactions. From a Luttinger liquid point of view, one can't reach $K_\rho < 0.5$ with only on site interactions. With the nearest neighbour interactions a wider range of K_ρ values is available. Especially, we learned in section 2.2.3 that the critical value for the phase transition to the quarter filled Mott insulator is $K_\rho^* = 0.25$ which can only be reached by at least nearest neighbour interactions. Since the physics of extended Hubbard type interactions is much more rich, we will focus on them from now on.

4.3.2 Spin dependence of the spectral densities

Until now the spectral densities did always show contributions from both spin species at once. However, sometimes it can be interesting to look at the contribution from a single spin species. Especially, the eigenstates of the $\hat{S}^y$ operator are of interest because this is also the direction in which the spin-orbit coupling is applied.

By doing additional simulations for the four off-diagonal terms $S_{a_\uparrow a_\downarrow^\dagger}(k,\omega)$, $S_{a_\downarrow a_\uparrow^\dagger}(k,\omega)$, $S_{a_\uparrow^\dagger a_\downarrow}(k,\omega)$ and $S_{a_\downarrow^\dagger a_\uparrow}(k,\omega)$ the spin information can be reconstructed for arbitrary spin directions, see also equation (3.82). The results for selected interactions are shown in figure 4.46 to 4.20.

In figure 4.46 we calculated the noninteracting system for comparing it to the dispersion relations. The combined information of these spectra gives all the information necessary for drawing the arrows in the dispersion relation. The two upmost panels show the spin $\uparrow$ and

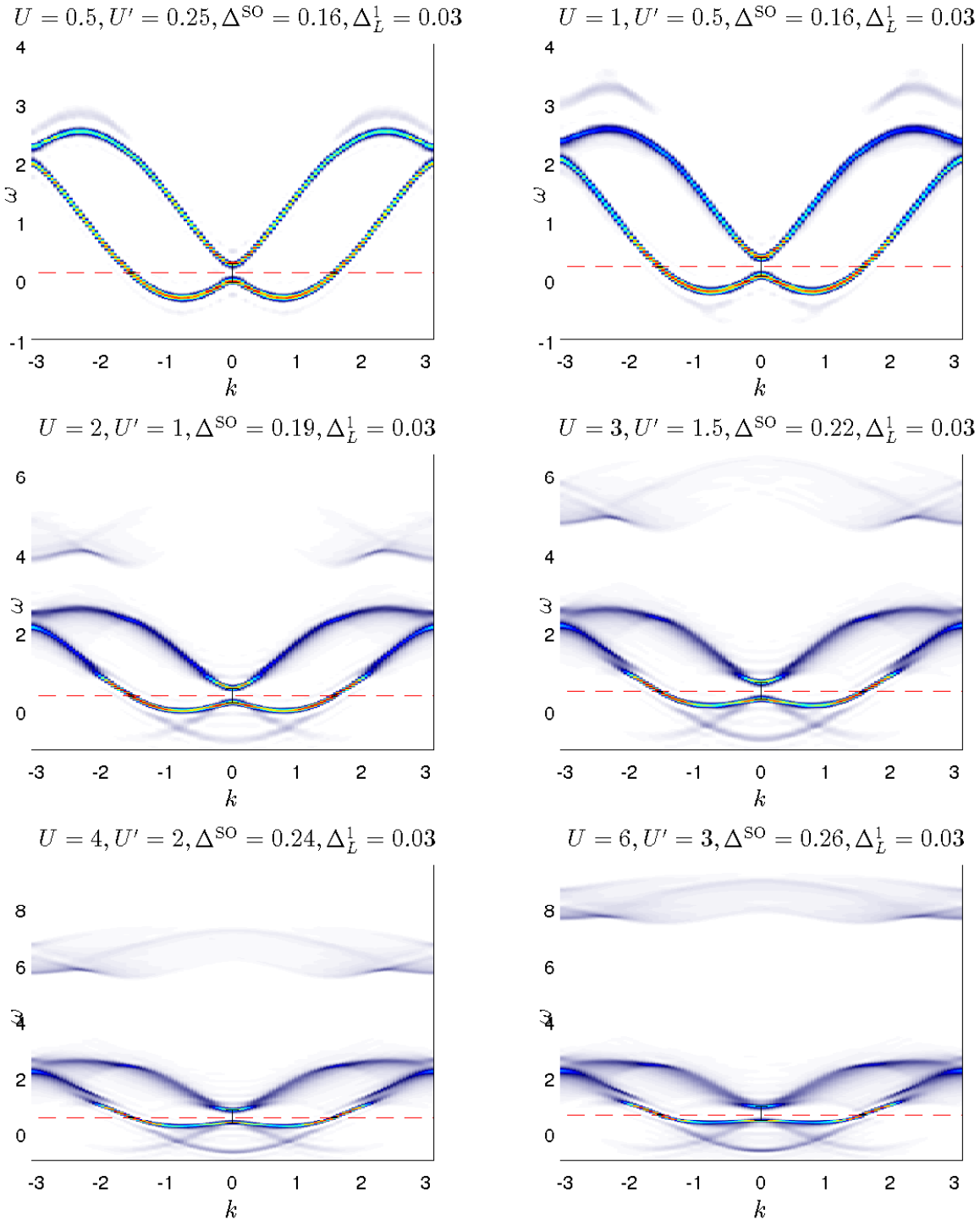

Figure 4.14: Spectral densities for systems with quarter filling and length $L = 128$ with $\alpha = 1$, $B = 0.1$ at different interaction strengths with $U' = 0$. The dashed red line is the chemical potential, the distance at $k = 0$ illustrates the spin-orbit gap and at $k = \frac{\pi}{2}$ the single particle excitation gap calculated from equation (4.9), which is only a finite size gap here.

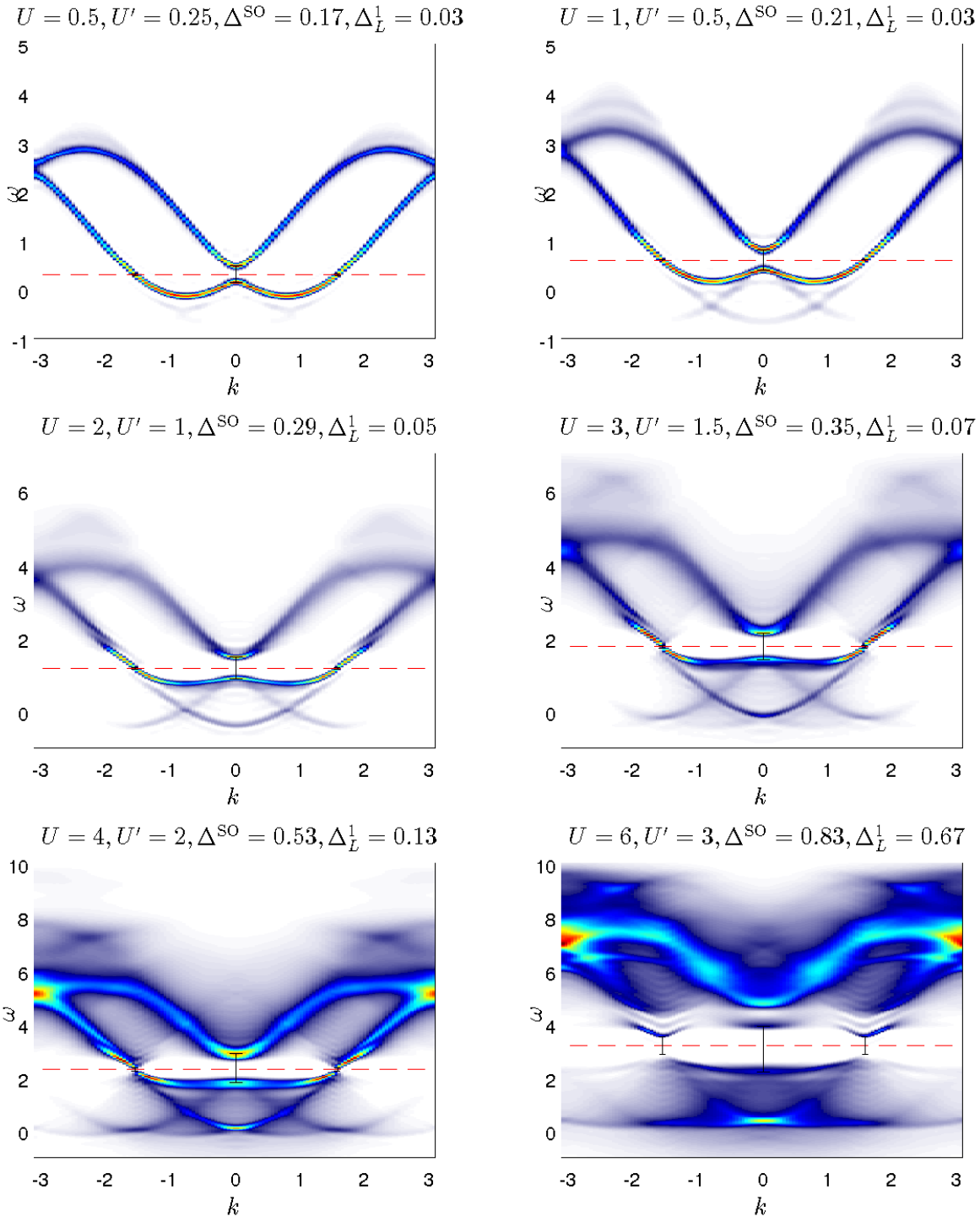

Figure 4.15: Spectral densities for systems with quarter filling and length $L = 128$ with $\alpha = 1$, $B = 0.1$ at different interaction strengths with $U' = U/2$. The dashed red line is the chemical potential, the black distance at $k = 0$ illustrates the spin gap and the black distance at $k = \pi/2$ is the single particle excitation gap calculated from equation (4.9).

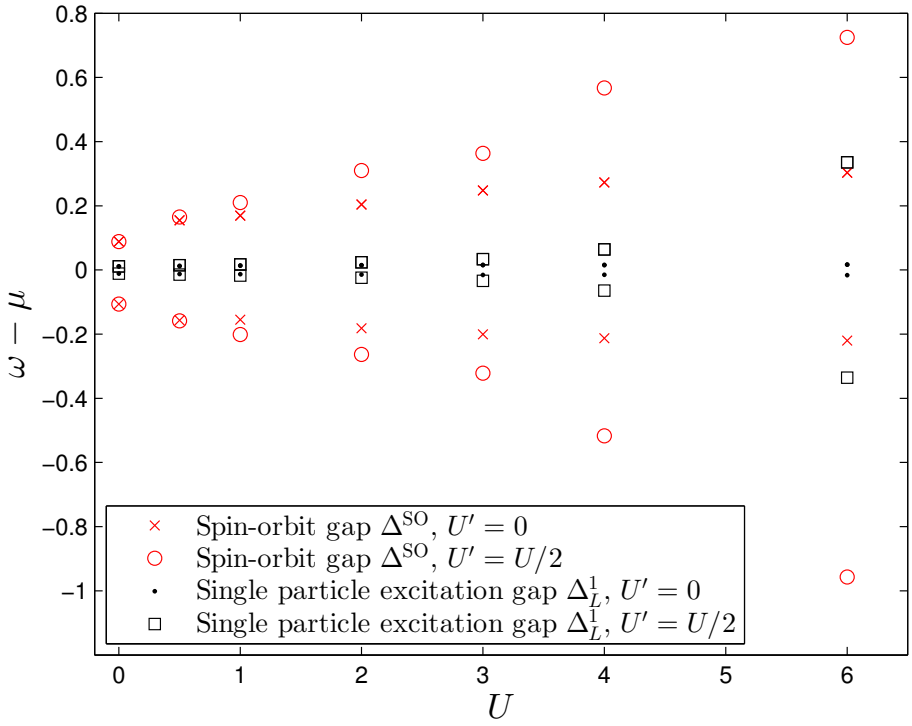

Figure 4.16: The spin gap and single particle excitation gap as a function of U. The spin gap was directly extracted from figure 4.14 and 4.15 and the single particle excitation gap was calculated from equation (4.9). No extrapolation to infinite system sizes was used here.

$\downarrow$ directions. Generally, spin $\uparrow$ states have a higher energy than spin $\downarrow$ states due to the magnetic field. The middle panels show the spin $\rightarrow$ and $\leftarrow$ directons. We can clearly see the helical spin order, that there is only one Fermi point for each spin species. The two lowest panels show the spin $+$ and $-$ directions. Since neither $+$ nor $-$ direction is distinguished in the Hamiltonian we expect them to be the same. They simply show the whole spectrum.

This spin properties basically remain also for the moderate interactions in figure 4.18 and 4.19. Most importantly, we can say from these simulations that the helical spin order at opposite Fermi points remains. Therefore, introducing interaction is a way to enhance the spin-orbit gap without destroying the helical spin order. Simply increasing the magnetic field B would also lead to a larger gap, but the spin directions at opposite Fermi points loose their orthogonality if $B \approx \alpha$. This orthogonality would be important for possible applications in spintronics.

Deep inside the Mott phase in figure 4.20 the spin behaviour is not so obvious anymore. Interaction effects dominate over the effect of the spin-orbit coupling. One can see that the spectra for spin $+$ and $-$ directions are asymmetric, which they shouldn't be. This is due to the strong spatial ordering in the Mott phase. These effects are also discussed in appendix B.

In section 2.2.2 we discussed a similar model to our system with the same Luttinger liquid description, a model where a partial gap is opened up due to the interaction between

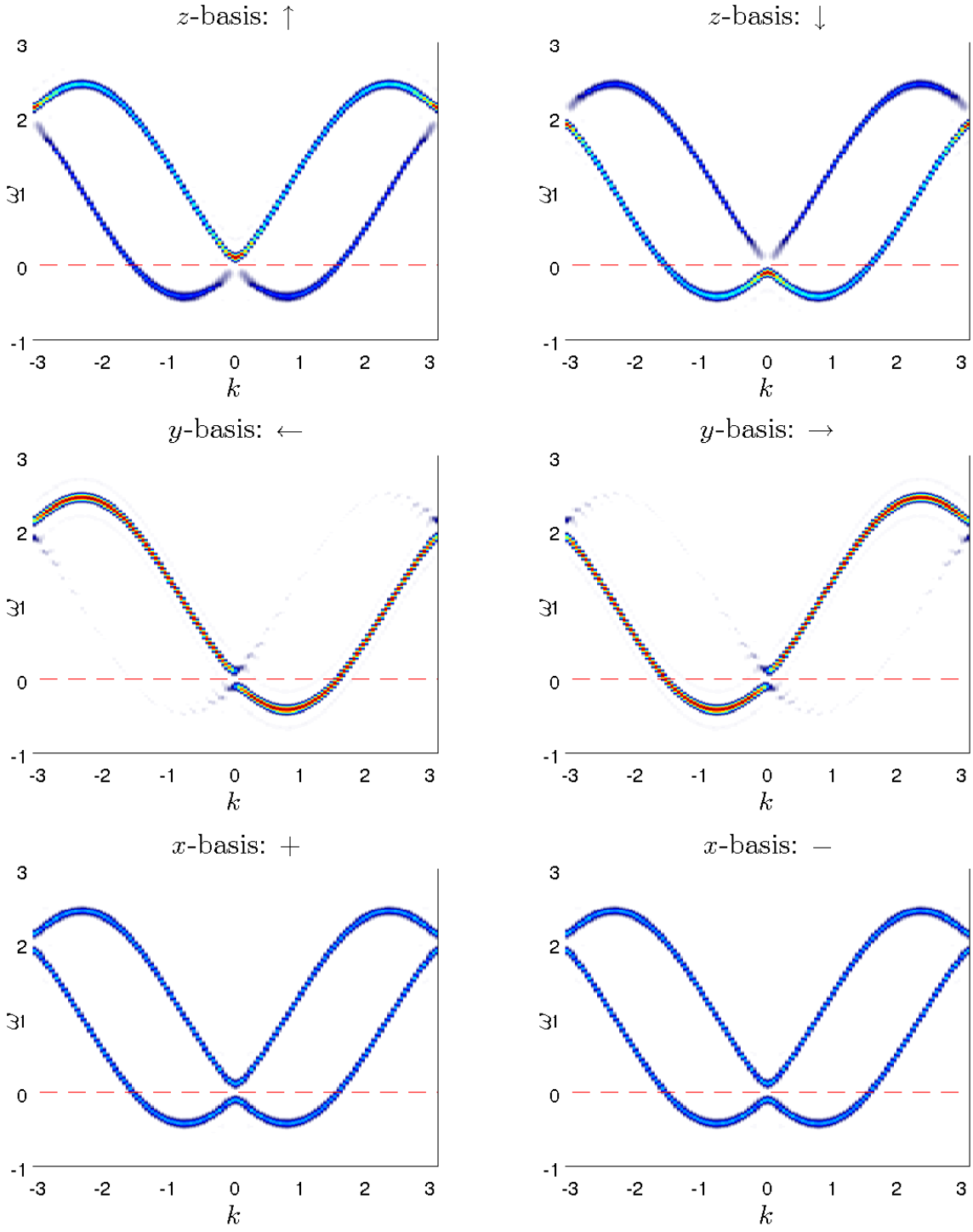

Figure 4.17: Spectral densities for systems with quarter filling and length $L = 128$ with $\alpha = 1$, $B = 0.1$ at $U = 0$ and $U' = 0$. The dashed red line is the chemical potential.

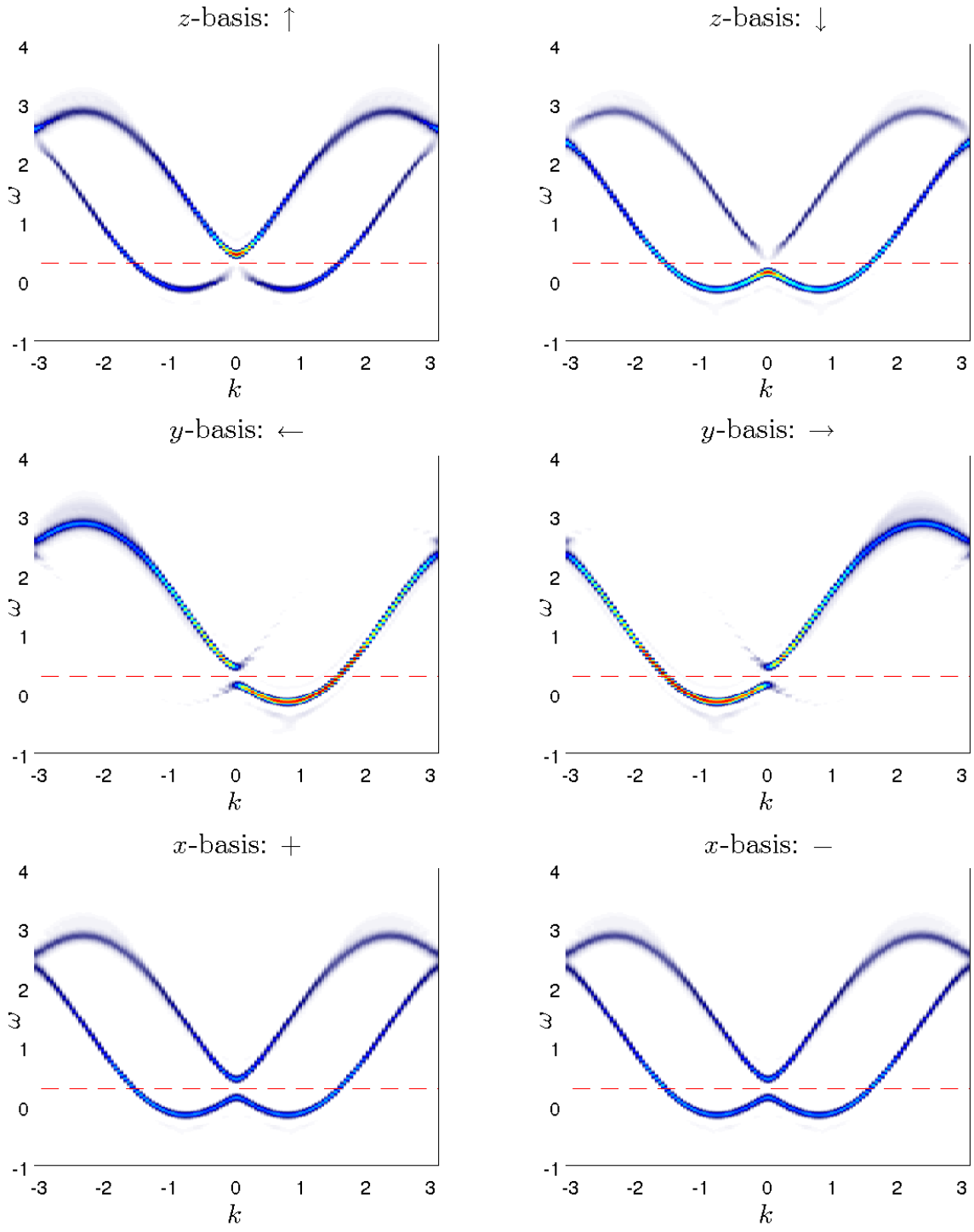

Figure 4.18: Spectral densities for systems with quarter filling and length $L = 128$ with $\alpha = 1$, $B = 0.1$ at $U = 0.5$ and $U' = 0.25$. The dashed red line is the chemical potential.

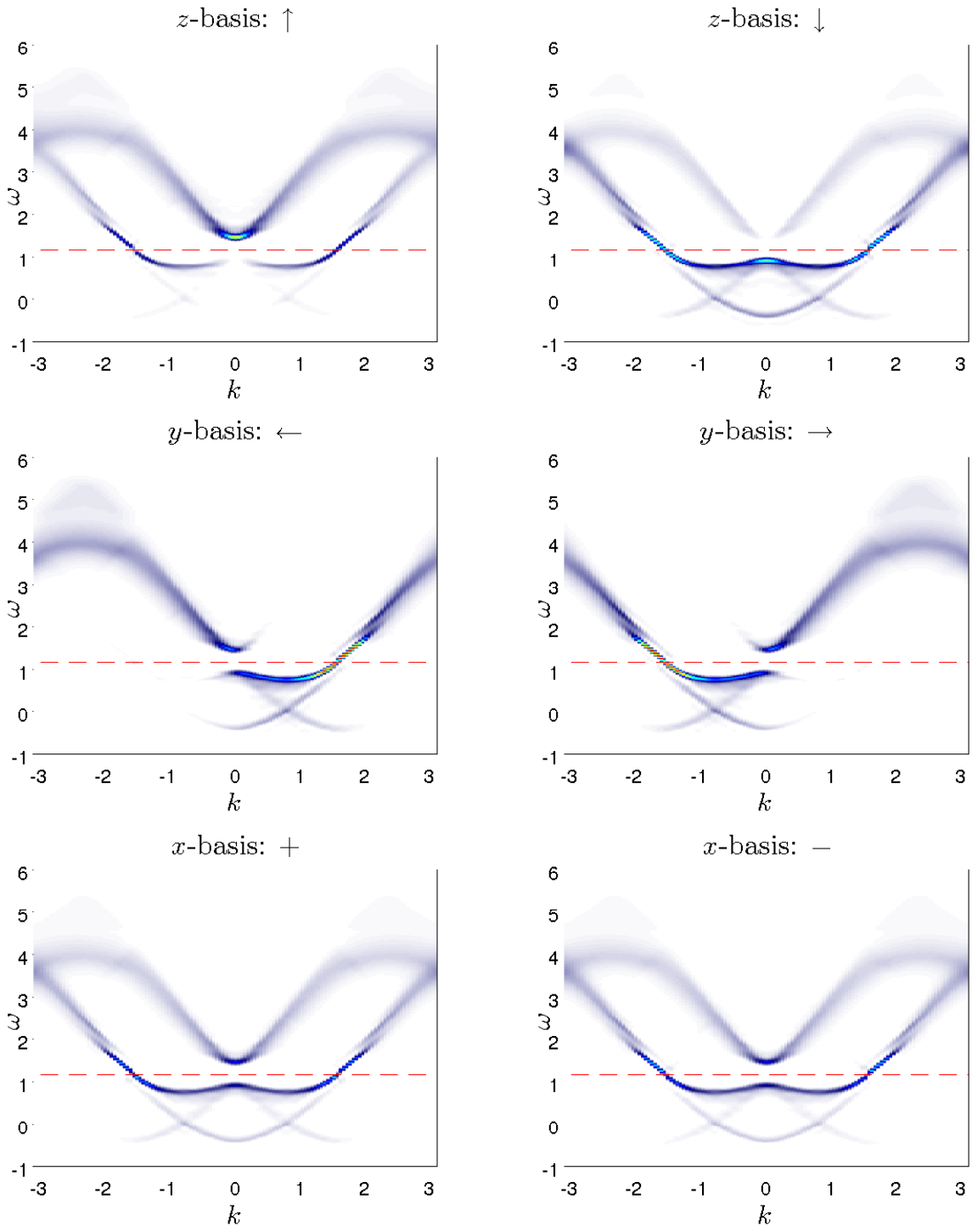

Figure 4.19: Spectral densities for systems with quarter filling and length $L = 128$ with $\alpha = 1$, $B = 0.1$ at $U = 2$ and $U' = 1$. The dashed red line is the chemical potential.

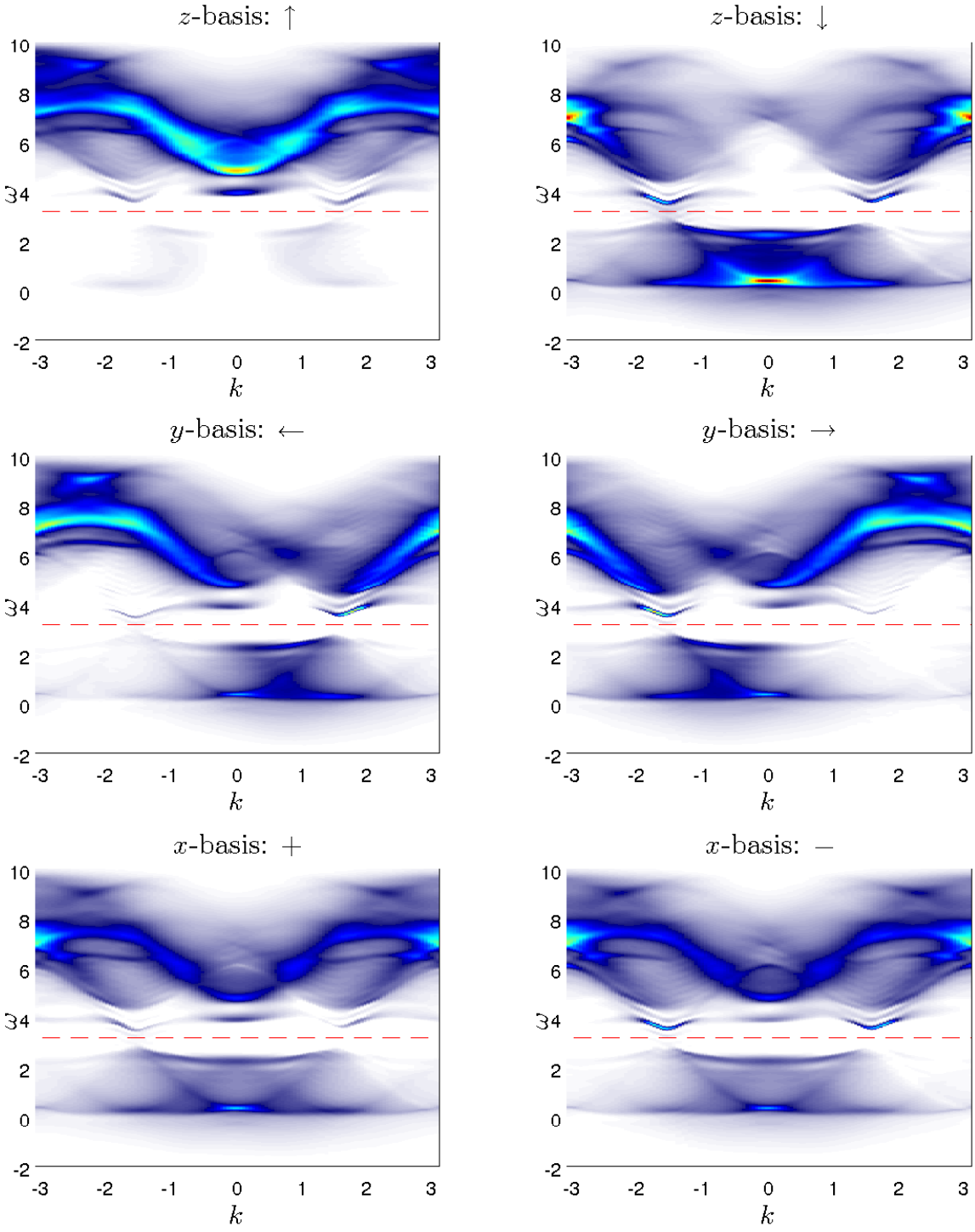

Figure 4.20: Spectral densities for systems with quarter filling and length $L = 128$ with $\alpha = 1$, $B = 0.1$ at $U = 6$ and $U' = 3$. The dashed red line is the chemical potential.

the electron spins and nuclear spins. These two models are connected by a simple gauge transformation

$$\psi_{\sigma_y}(r) \to e^{i\sigma_y k_{\mathrm{SO}} r}\psi_{\sigma_y}. \tag{4.10}$$

Since we have the spectra for the spin $\rightarrow$ and $\leftarrow$ directions separately available, it is straightforward to implement this transformation and show the corresponding spectra for the model with the nuclear spins. The gauge transformation simply amounts to shifting the spin $\leftarrow$ spectrum by k_{SO} to the left and the spin $\rightarrow$ by k_{SO} to the right. Afterwards they can be added to obtain the full spectrum. See figure 4.21 for the transformed spectra at different interactions.

We see that this transformation moves the gap from $k = 0$ out to the Fermi points. Since it is only a partial gap, we only see an ω-range with less spectral weight around the Fermi points. Generally, the system now looks much more like an ordinary Hubbard model. The spin-orbit coupling and the magnetic field is eliminated by the transformation and replaced by a helical magnetic field. As a consequence, the dispersions are not shifted anymore. At the strongest interaction in figure 4.21 (c) we see that the structure below the main branch transforms to something that is suspiciously similar to the collective spin excitation branch (spinon) in an ordinary Hubbard model. Compare e.g. to the Hubbard spectrum in figure B.1 in appendix B. Here a similar structure is below the usual cosine dispersion. In the Hubbard model it is known that this structure is the spinon dispersion.

4.3.3 Spectral densities for 2 and 4 Fermi point phases

Finally, in figure 4.22 we give the spectra for the two different 2 and 4 Fermi point phases at a moderate interaction of $U = 2$ and $U' = 1$. The system is still metallic, and a Luttinger liquid, at this interaction. Only the strength of the spin-orbit interaction α is varied, all other quantities are held fixed. By increasing α one achieves that the two dispersions move away from $k = 0$. Therefore, their point of intersection, or the spin-orbit gap at finite B, moves upwards to higher energies. Starting at $\alpha = 0$ the Fermi level is clearly above the spin-orbit gap and inside the 4-Fermi point phase. As soon as the Fermi energy slips into the 2-Fermi point phase at $\alpha = 0.6$, the spin-orbit gap is suddenly greatly enhanced. Going below the spin-orbit gap at $\alpha = 1.3$ the system is again inside the 4 Fermi point phase.

Distinguishing the 2 and 4 Fermi point phases using the spectra is straightforward by counting the number of Fermi points. However, each simulation for a spectra takes a few days of computer time making it unfeasible for drawing phase diagrams. In the next section we will discuss methods for determining the phase from the ground state properties.

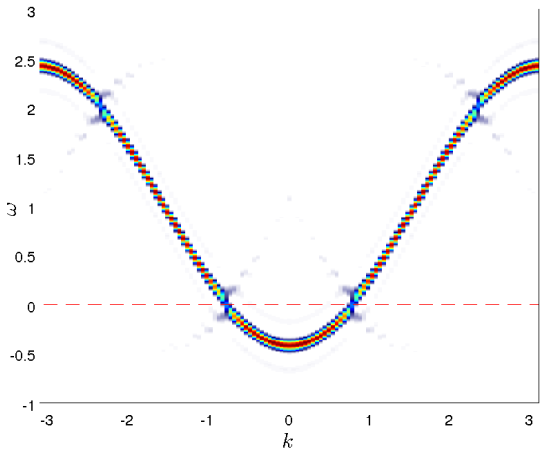

(a) $U = 0,\ U' = 0$

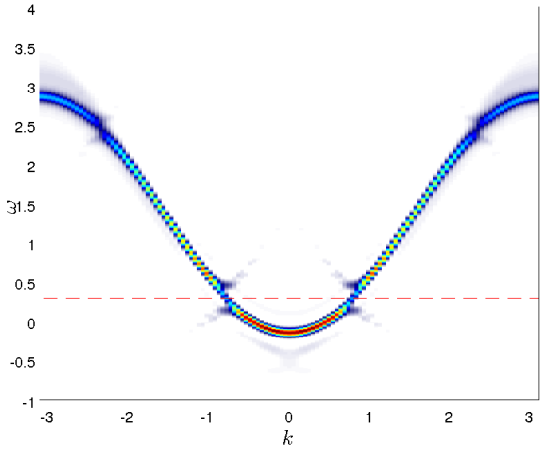

(b) $U = 0.5,\ U' = 0.25$

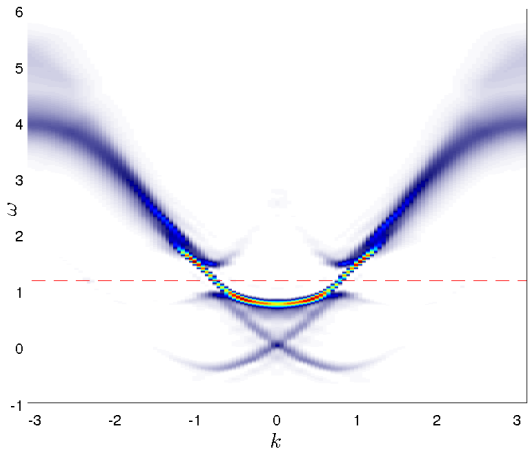

(c) $U = 2,\ U' = 1$

Figure 4.21: The full spectrum after the gauge transformation (4.10) for different interactions.

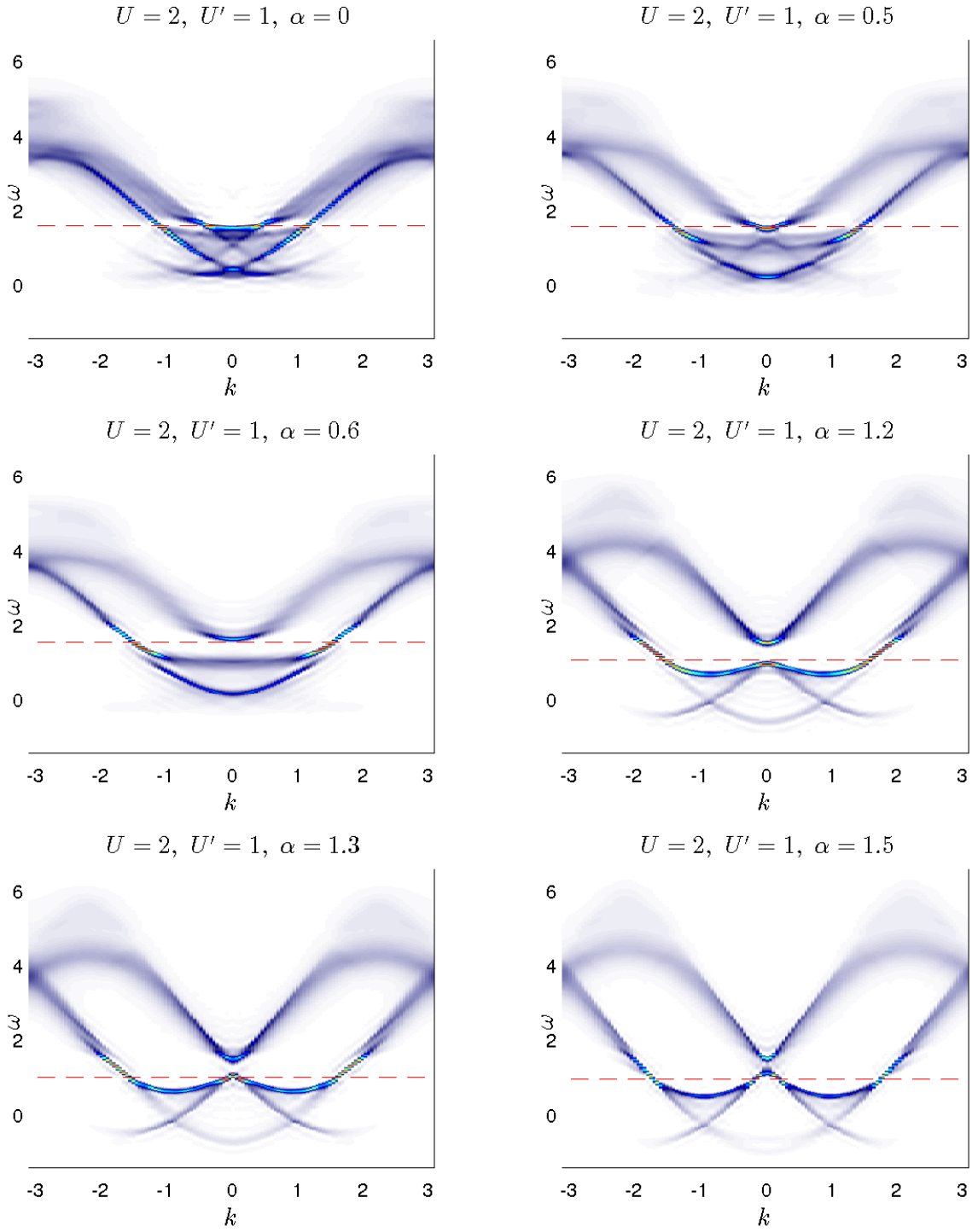

Figure 4.22: Spectral densities for systems with quarter filling, $L = 64,\ B = 0.1,\ U = 2$ and $U' = 1$ for different values of α. Plotted is both the particle and hole part of the spectral density, the dashed red line is the chemical potential. The values $\alpha = 0.6$ and $\alpha = 1.2$ are inside the spin gap.

4.4 Phase boundaries for the 2 and 4 Fermi point regimes

In this section the phase boundaries between the 2 and 4 Fermi point regimes are examined with high accuracy. In principle, one could extract the phase from the spectra like it was done in figure 4.22. However, time evolutions are computationally rather expensive and many would be needed for fixing the exact point of phase transition. Our search for computationally less expensive observables found an end in the Luttinger liquid coefficients K_ρ and K_σ. They can be extracted from the charge, respectively spin, correlation functions which are relatively easy to measure in the ground state. Only one ground state calculation is needed (for the method we primarly employed).

How do we know that the phase boundaries extracted from K_ρ and K_σ are reliable? Without interactions the boundaries can be calculated straightforward from the dispersion relation. In the special case of quarter filling we also found another method of distinguishing the phases, by looking at the Friedel oscillations. Finally, of course, the results are checked to be consistent with the spectral densities.

The system has a lot of parameters, therefore it is not feasible sweeping through all of them. We always vary the interaction strength together with another parameter to get a two-dimensional phase diagram. First we will vary the spin-orbit coupling (at fixed quarter filling) and then we will vary the filling (at fixed spin-orbit coupling $\alpha = 1$). Throughout the whole section (with one exception) we keep a magnetic field of $B = 0.1$ and we concentrate on the extended Hubbard model with $U' = U/2$. The previous section about spectral densities teached us that in the case with nonzero U' interaction effects are much stronger, so this is the more interesting case we want to focus on.

4.4.1 Luttinger liquid coefficients

The Luttinger liquid coefficients K_ρ and K_σ are the two parameters that encode the interaction in the Luttinger liquid model. Here we calculated them inside the spin-orbit gap from equation (3.92) and (3.98) (respectively (3.94)). Beforehand, we tested our method against known results from Hubbard and extended Hubbard models with good agreement. For testing purposes we also determined K_ρ with an independent method in appendix C and both methods agree within reasonable accuracy. However, the Luttinger liquid coefficients for systems with spin-orbit coupling and external magnetic field have not been calculated yet as far as we know. Here we discuss the applicability of the method on our system.

We calculated the Luttinger liquid coefficients for system sizes from $L = 16$ up to $L = 512$ and matrix dimensions up to $m = 1000$. The convergence was checked with smaller matrix dimensions. Generally, the long range behaviour of a correlation function, and the Luttinger liquid coefficients, are quite sensitive to the used matrix dimension. Other observables like the energy usually converge already with a much smaller matrix dimension. Here we always use quarter filling.

Also special care has to be taken to obtain the result in the thermodynamic limit $L = \infty$. For this purpose we plot the Luttinger liquid coefficient for different system sizes over $\frac{1}{L}$ and then apply a polynomial fit of fourth order to the data. The fit is then extrapolated to $\frac{1}{L} = 0$ to obtain the value for infinite system sizes. This is the standard method which proved to give reliable results in most occasions.

The determination of K_ρ from the charge structure factor is given in figure 4.23. For the noninteracting case $U = 0$ and $U' = 0$ it follows from Luttinger liquid theory that $K_\rho = 1$.

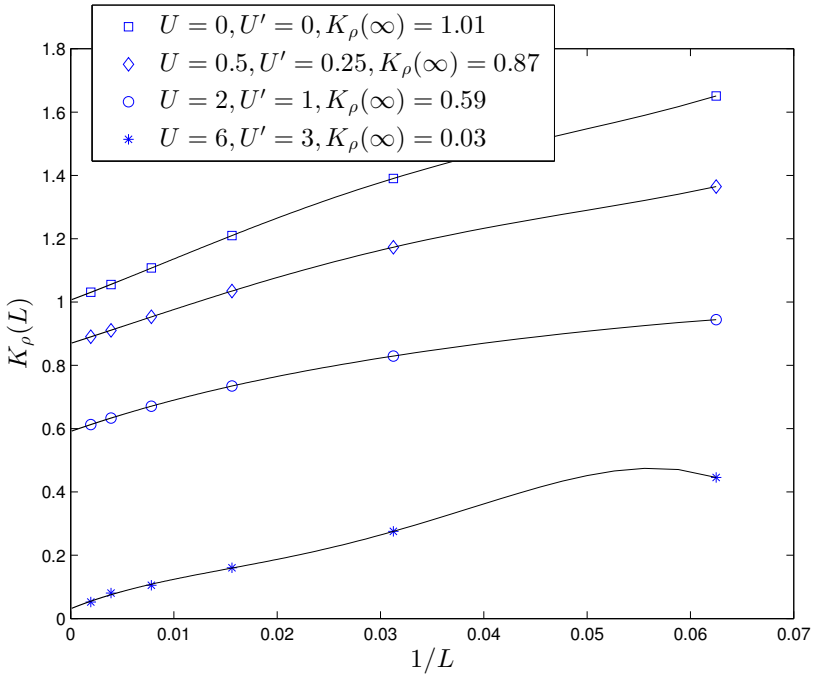

Figure 4.23: Luttinger Liquid coefficient $K_\rho(L)$ for different interaction strengths U and U' and $\alpha = 1,\ B = 0.2$. $K_\rho(\infty)$ has been extrapolated by a fourth order polynomial fit.

The calculation yields $K_\rho = 1.0064$ which is in good agreement. Generally, it holds that for repulsive interactions $K_\rho < 1$ and for attractive interactions $K_\rho > 1$. We then see K_ρ decreasing with the interaction, which is in accordance to our repulsive interaction. The system is at quarter filling so we expect a charge gap to open up at high interactions due to the Mott insulating phase. The interaction $U = 6$ and $U' = 3$ is already deep inside the Mott insulating phase. The Luttinger liquid coefficient K_ρ should be zero if the system has a charge gap and indeed it takes a very small value there $K_\rho = 0.0311$. However, the criteria $K_\rho = 0$ inside a charge gap is usually not met with numerical simulations. Logarithmic corrections get in the way at the system sizes available, therefore it is better to look at critical values for K_ρ. Nevertheless, these are all hints that the calculated K_ρ is reliable.

The calculation of K_σ is a little bit more cumbersome than for K_ρ. First one has to decide on a spin direction in which the spin structure factor should be measured, since our model is not isotropic in the spin direction. Due to the spin-orbit coupling the $\hat{S}^y$ direction is special over the other directions. Also, in the spiral Luttinger liquid model the spin quantization axis coresponds to the $\hat{S}^y$ direction in our system. Therefore, this direction should be chosen for comparing our simulations with the spiral Luttinger liquid model. For discerning the 2 and 4 Fermi point phases however, the $\hat{S}^z$ direction is more useful as we will see later.

Generally, we find that as long as the system has no spin-orbit coupling, equation (3.94) can be used. However, as soon as the spin-orbit coupling is turned on the spin structure factor $\tilde{C}^{S^i S^i}(q)$ doesn't approach zero at $q = 0$. We illustrated this behaviour in figure 4.24. The reason is that the good quantization axis is k-dependent in this case. Therefore, for nonvanishing spin-orbit interaction α equation (3.98) is always used instead of (3.94).

First we give results for K_σ at $\alpha = 0$ and $B = 0$ for a quarter filled extended Hubbard

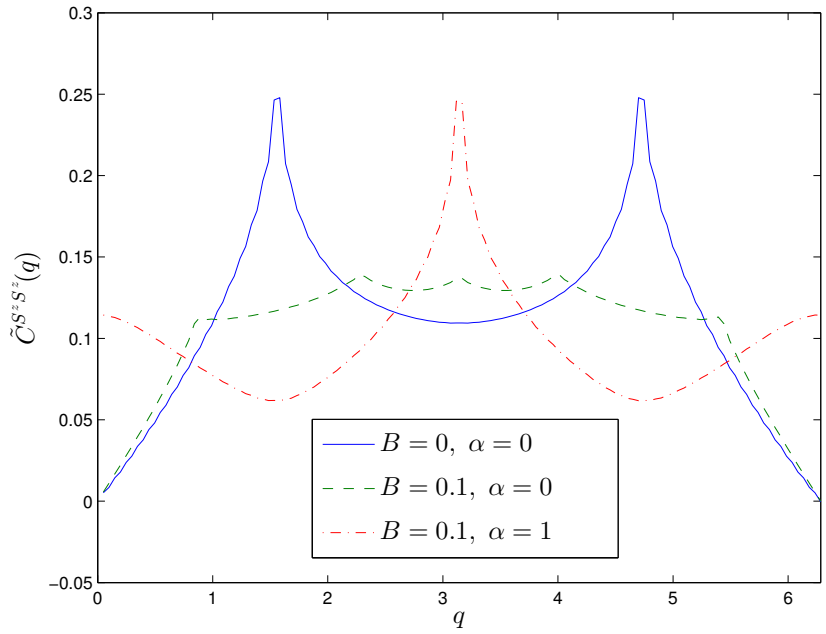

Figure 4.24: Spin structure factor at $U = 2$ and $U' = 1$ for different B and α.

model in figure 4.25. Here we can use (3.94). In the noninteracting case we get $K_\sigma = 1$ as expected. Because of the spin isotropy we would expect $K_\sigma = 1$ at all interactions. However, we get that K_σ grows with the interaction. Due to logarithmic corrections the value $K_\sigma = 1$ is not reached in the system sizes accessible to DMRG. Generally $K_\sigma > 1$ corresponds to a massless spin sector, whereas $K_\sigma < 1$ would indicate a spin gap. It is known, however, that the logarithmic corrections vanish at the point where a spin gap opens [23]. Therefore, it is common practice to look at the point where K_σ crosses 1 to find the phase transition to a spin density wave state with a spin gap.

Now we want to give K_σ for systems with spin-orbit coupling and an external magnetic field. Here one has to distinguish in the direction in which the spin structure factor is measured. In figure 4.26 K_σ is given for the $\hat{S}^y$ direction. For smaller interactions it looks very similar to figure 4.24. At the largest interaction $U = 6$ and $U' = 3$ something very weird happens. Clearly the extrapolation is not reliable here.

K_σ from the spin structure factor in the $\hat{S}^z$ direction is given 4.27. It behaves totally different in this direction than before. For smaller interactions it always goes to zero, which would indicate a spin gap in $\hat{S}^z$. At $U = 6$ and $U' = 3$ again something weird is going on hinting that the extrapolation is not reliable. It should be noted that only K_σ calculated from $\hat{S}^z$ scales to zero. If we calculate K_σ from $\hat{S}^x$ it behaves again totally different and even takes on negative values. However, we found K_σ calculated from $\hat{S}^z$ to be the most helpful in distinguishing the phases. It will show that it only scales to zero inside the partial gap, but has nonzero values outside.

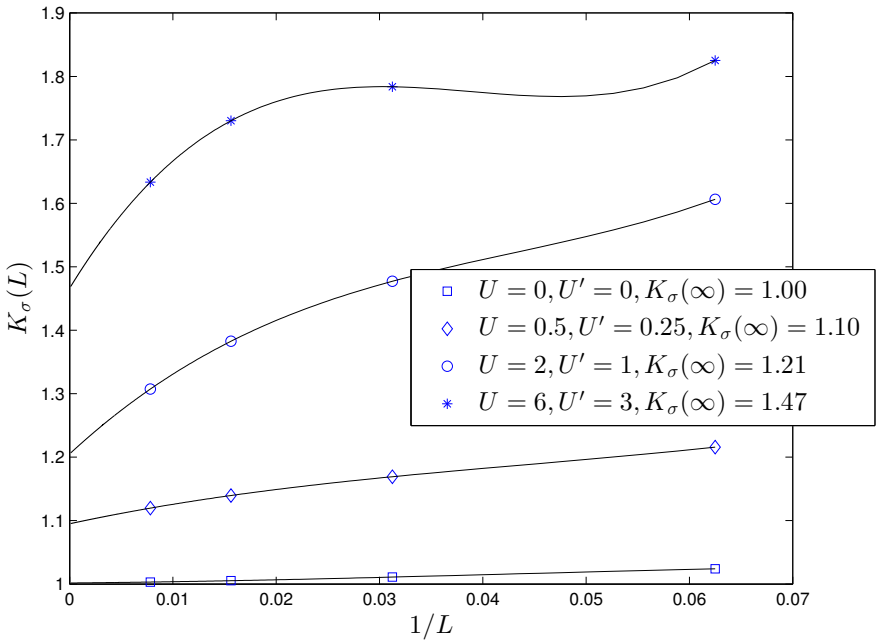

Figure 4.25: Luttinger Liquid coefficient $K_\sigma(L)$ for different interaction strengths U and U' and $\alpha = 0,\ B = 0$. $K_\sigma(\infty)$ has been extrapolated by a third order polynomial fit.

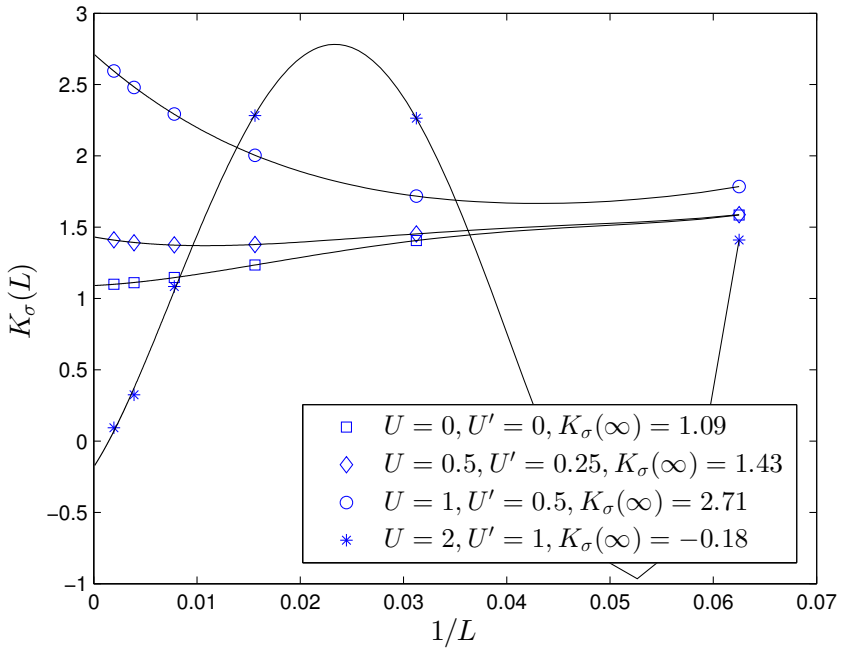

Figure 4.26: Luttinger Liquid coefficient $K_\sigma(L)$ obtained from $\tilde{C}^{S^y S^y}(q)$ for different interaction strengths U and U' and $\alpha = 1,\ B = 0.2$. $K_\sigma(\infty)$ has been extrapolated by a fourth order polynomial fit.

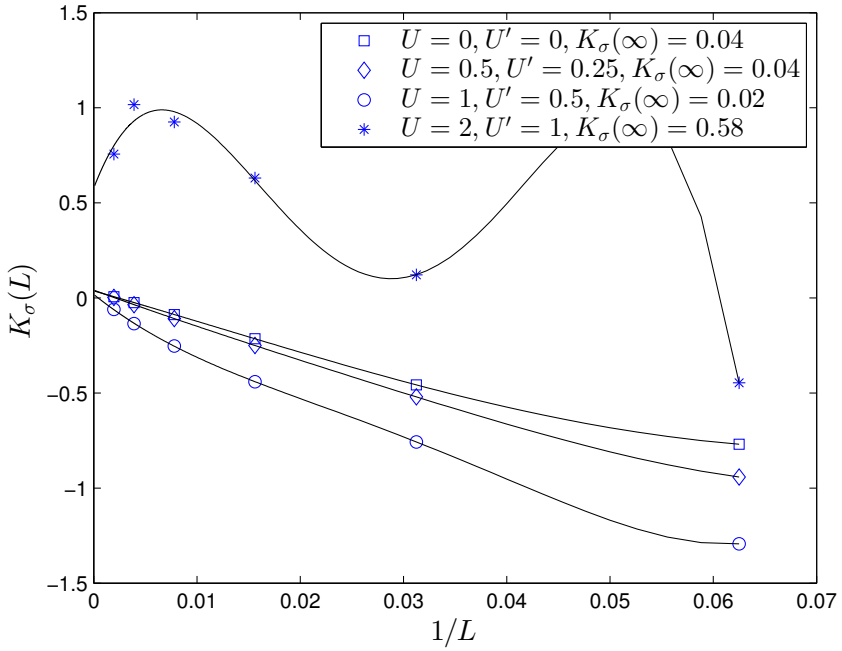

Figure 4.27: Luttinger Liquid coefficient $K_\sigma(L)$ obtained from $\tilde{C}^{S^zS^z}(q)$ for different interaction strengths U and U' and $\alpha = 1,\ B = 0.2$. $K_\sigma(\infty)$ has been extrapolated by a fourth order polynomial fit.

4.4.2 Phase boundaries in α

Now we want to draw our first phase diagram with the use of the Luttinger liquid coefficients. Like in figure 4.22 we will vary the strength of the spin-orbit coupling α to switch from the 2 Fermi point phase to the 4 Fermi point phases. We know from section 2.1.3 that the system is only inside the spin-orbit gap (the 2 Fermi point phase) if the Fermi momentum k_F is approximately two times the spin-orbit momentum k_SO. Going away from this condition, the system will eventually switch into a 4 Fermi point phase.

For $\alpha = t = 1$ it follows from equation (2.7) that $k_\mathrm{SO} = \frac{\pi}{4}$. Therefore, the Fermi momentum has to be $k_\mathrm{F} = \frac{\pi}{2}$ which amounts to $n = 0.5$, thus quarter filling. Then α is varied to find the size of the gap as a function of the interactions. We keep $B = 0.1$ and $n = 0.5$ fixed. In the noninteracting case for quarter filling α can take values between

$$\sqrt{t^2 - 2Bt} < \alpha < \sqrt{t^2 + 2Bt}, \tag{4.11}$$

inside the spin-orbit gap.

Figure 4.28 shows the α-dependece of the Luttinger liquid coefficient $K_\rho(128)$. We omitt the extrapolation to infinite system sizes here because it fails near the phase boundaries. Near a boundary the situation can occur that a smaller system size still belongs to one phase, whereas a larger system size already belongs to the other phase. The jump occuring between the phases then makes the extrapolation useless. Fortunately, for the distinction of the phases the exact value of K_ρ is not necessary. It suffices to note the characteristic jump at the phase boundary. Therefore, the numerical values of K_ρ given here should not be taken

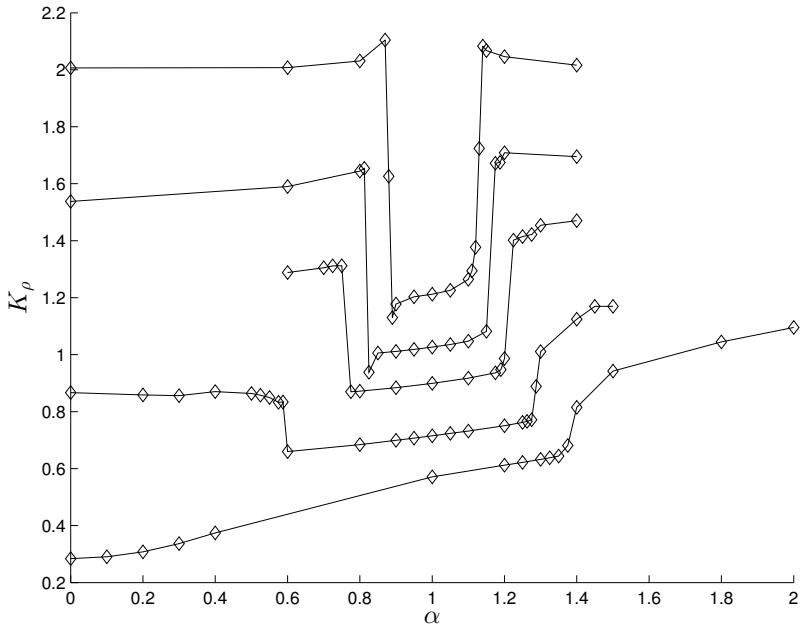

Figure 4.28: Luttinger Liquid coefficient $K_\rho(128)$ for different interaction strengths U and U' and as a function of α for $B = 0.1$ and quarter filling. The interaction strengths are from top to bottom $U = 0,\ 0.5,\ 1,\ 2,\ 3$ and $U' = U/2$.

too seriously because they are only finite size values. Moreover, equation (3.92) would need to be modified outside the partial gap. We use the form for spinless fermions through the whole α-interval.

One has to be careful that the system size is large enough so that the phase boundaries converge. Therefore, we give the size dependence of K_ρ in figure 4.29. A system size of $L = 128$ gives the phase boundaries already with reasonable accuracy for an acceptable computational cost. As a side remark, we also observe that the Luttinger liquid coefficient converges much faster in the 4 Fermi point phase than in the 2 Fermi point phase.

The jumps in figure 4.28 clearly indicate the boundaries from the 4 to the 2 Fermi point phase. In the noninteracting case, the jump is actually exactly a factor of 2 if extrapolation would be used. With stronger interactions this factor is reduced but a sharp boundary still remains. Only at very strong interactions $U > 2$ these boundaries slowly vanish indicating another, non Luttinger liquid, phase. We already saw from the spectral functions that a charge gap begins to open for strong interactions and $U' = U/2$. This Mott insulating phase will be investigated in section 4.5.

The very same information can be also extracted from K_σ. For this application it is advantageous to use the spin structure factor in the $\hat{S}^z$ direction. Then we see a jump that is even more distinct than in K_ρ and it even seems to grow with the interaction. It was verified that K_ρ and K_σ give exactly the same phase boundaries. With these two quantities we have found easily accesable and very powerful tools for distinguishing the 4 and 2 Fermi point phases.

For completeness, we checked if we can also induce a phase transition by varying the

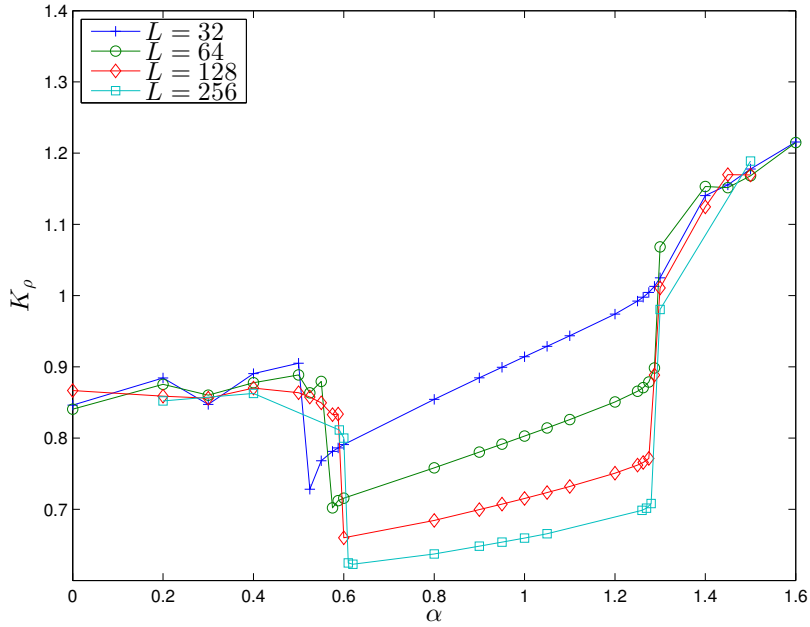

Figure 4.29: Luttinger Liquid coefficient $K_\rho(L)$ as a function of α for different system sizes at $U = 2,\ U' = 1,\ B = 0.1$ and quarter filling.

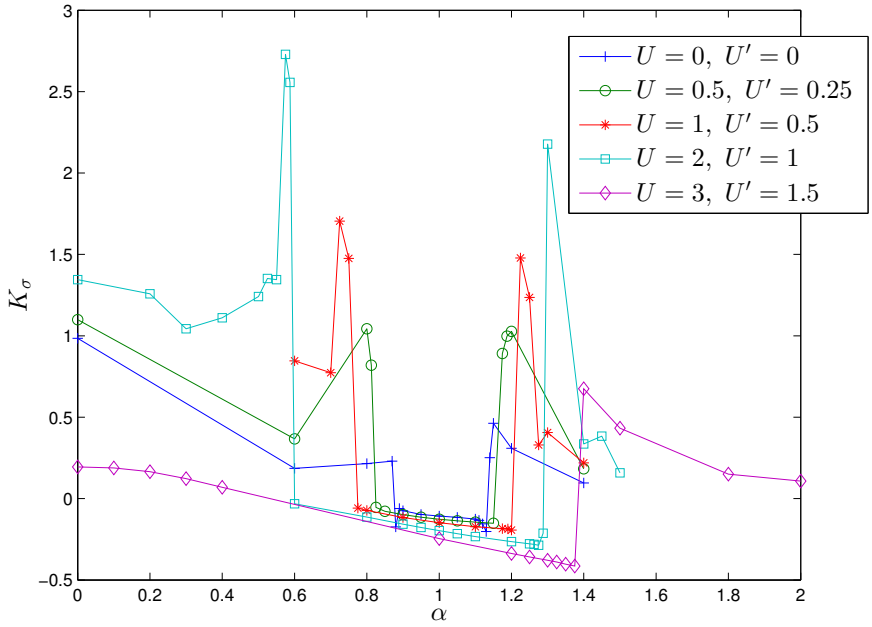

Figure 4.30: Luttinger Liquid coefficient $K_\sigma(128)$ for different interaction strengths U and U' and as a function of α for $B = 0.1$ and quarter filling.

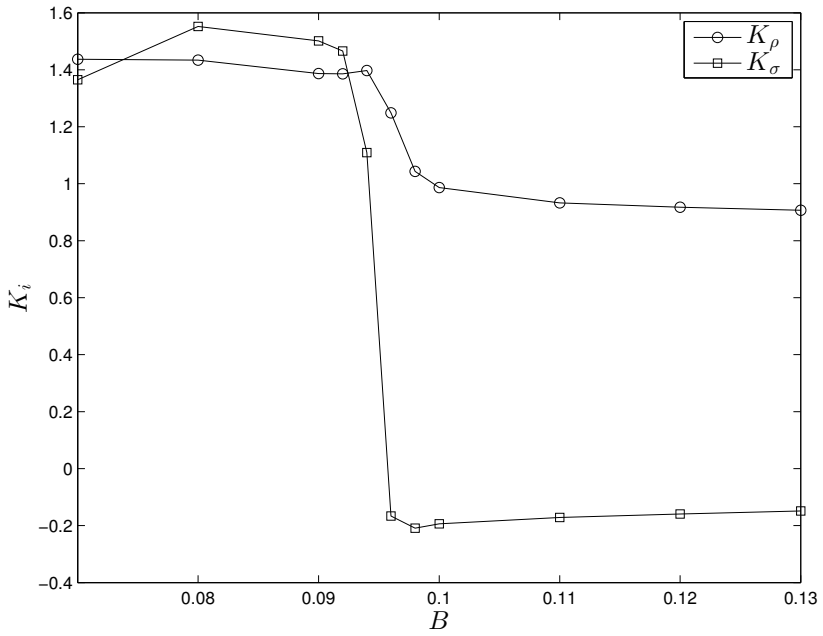

Figure 4.31: Luttinger Liquid coefficient $K_{\rho/\sigma}(128)$ as a function of B for quarter filling and $\alpha = 1.2$, $U = 1$ and $U' = 0.5$.

external magnetic field B. The magnetic field strength, together with the interaction, determines the size of the spin-orbit gap. One point near the phase boundary was chosen and B was then varied. The result is in figure 4.31. As expected we see the same kind of jump indicating the phase transition from 4 to 2 Fermi points into the spin-orbit gap.

We also found another method for distinguishing the phases using the commensurability of the filling. Because of the quarter filling we know from equation (2.11) that the Fermi momentum is always $k_\mathrm{F} = \frac{\pi}{2}$ inside the spin-orbit gap. Outside the spin-orbit gap (2.11) is wrong and the Fermi momentum will take some odd value. This can be seen in the Friedel oscillations because they depend very strong on the Fermi momentum. For spinless Fermions the asymptotic form of the Friedel oscillations is given by [9]

$$\frac{\delta\rho(x)}{\rho_0} = -(1 + \frac{x}{\tilde{\alpha}})^{-K_\rho} \cos(2k_\mathrm{F}x - K_\rho^2\lambda)P(x). \tag{4.12}$$

If $k_\mathrm{F} = \frac{\pi}{2}$ the Friedel oscillations have a period of 2. Outside of the spin-orbit gap, in the 4 Fermi point phase, this period is messed up. In figure 4.32 the phases can be distinguished very clearly. Once again the phase boundaries extracted here give the same result as all the previous methods.

Finally, we can combine the information from the many DMRG simulations and plot a single phase diagram in figure 4.33. Starting at $\alpha = 1$ the system is inside the partial gap. Decreasing the spin-orbit coupling the Fermi level moves to the top of the partial gap and at some point the system switches to the 4 Fermi point phase. Increasing the spin-orbit coupling the Fermi level moves to the lower end of the partial gap and the system switches again to the 4 Fermi point phase. See also figure 4.22.

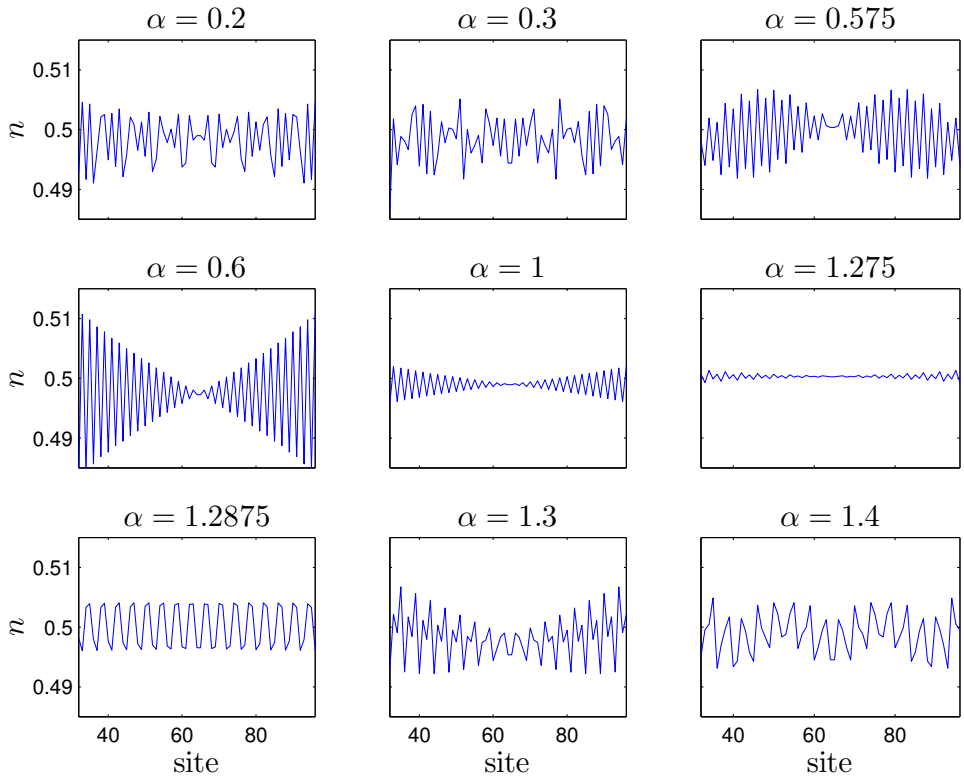

Figure 4.32: Friedel oscillations in the density n at quarter filling for different values of α. The other parameters $B = 0.1,\ U = 2,\ U' = 1$ are held fixed. The values from $\alpha = 0.6$ to $\alpha = 1.275$ are inside the gap.

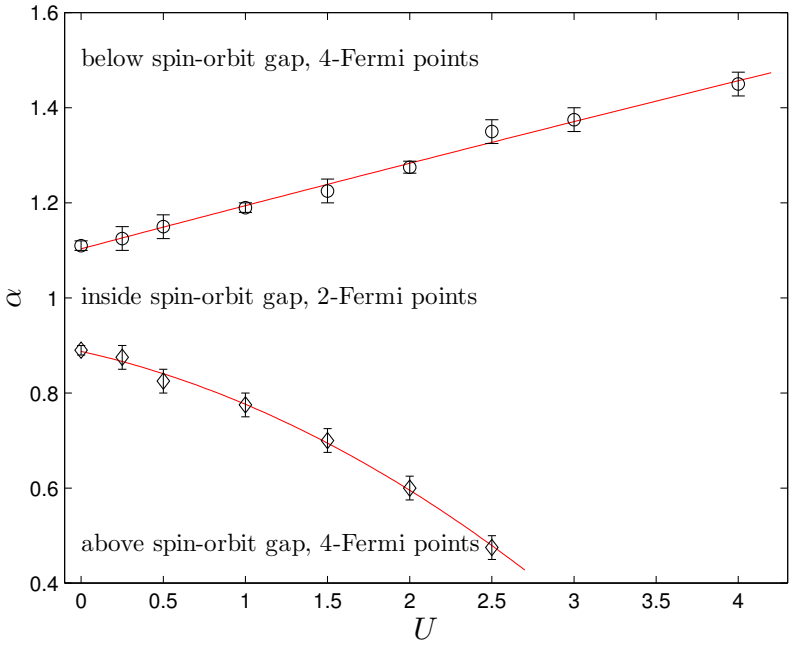

Figure 4.33: Phase diagram for α and U with the nearest-neighbour interaction $U' = U/2$. The other parameters are $B = 0.1$ and quarter filling. The upper red line is a linear fit and the lower a quadratic fit.

One may notice that the upper boundary is plotted until $U = 4$ whereas the lower boundary only until $U = 2.5$. A boundary was plotted as long as a jump was visible at the same position in K_ρ and K_σ. The upper jump simply lasted to stronger interactions than the lower. See also figure 4.28 and note the curve for $U = 3$.

The error bars plotted in figure 4.33 have two reasons. For one reason they simply come from the discrete data points nearest to the jump. One need at least two points, one before and one after the jump, to determine its position. The distance between these two points around the jump defines the uncertainty. The second reason is that especially at high interactions the jump itself is smeared out a little bit.

It should be also noted that the finite size error was not taken into account here. Strictly speaking, the phase boundaries are for a $L = 128$ site system with open boundary conditions. However, according to figure 4.29 the finite size error is smaller than the errorbars anyway.

What happens at higher interactions is the subject of section 4.5. However, we already know that a charge gap opens up and the system is going to leave the Luttinger liquid phase.

4.4.3 Phase boundaries in the filling n

Before we varied the spin-orbit coupling α to induce a change from the 2 Fermi point to the 4 Fermi point phase. Now we want to vary the filling n and keep α fixed to induce also a change from 2 to 4 Fermi points. Speaking in the language of noninteracting systems, in the last subsection we changed the shape of the dispersion relation and kept the Fermi level fixed. Now we keep the shape of the dispersion relation and vary the position of the Fermi

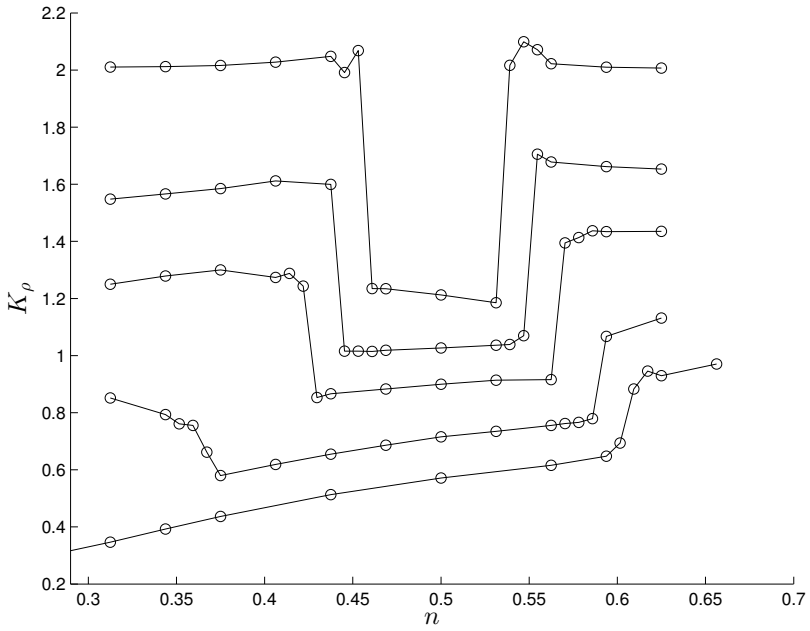

Figure 4.34: Luttinger Liquid coefficient $K_\rho(128)$ for different interaction strengths U and U' and as a function of n for $B = 0.1$ and $\alpha = 1$. The interaction strengths are from top to bottom $U = 0,\ 0.5,\ 1,\ 2,\ 3$ and $U' = U/2$.

level. Varying the filling too much away from the condition $k_\mathrm{F} = 2k_\mathrm{SO}$, the Fermi level will eventually come to the lower/upper boundary of the partial gap. In the noninteracting system the phase boundaries for the filling n are given by

$$\arccos(\frac{t^2 - \alpha^2 + 2Bt}{t^2 + \alpha^2}) < \pi n < \arccos(\frac{t^2 - \alpha^2 - 2Bt}{t^2 + \alpha^2}). \tag{4.13}$$

Like before, we look at the jumps in K_ρ and K_σ to find the phase boundaries. In figure 4.34 and 4.35 are the Luttinger liquid coefficients K_ρ and K_σ as a function of n.

The jumps are very distinct as before. Some of the curves in figure 4.34 and 4.35 show slight even/odd effects but their magnitude is always smaller than the actual jump at the phase boundary. Going away from quarter filling, one looses the possibility to extract the phase from the Friedel oscillations. Fortunately, we already know that K_ρ and K_σ give reliable phase boundaries. Also, as before, the jumps vanish at stronger interactions. Away from quarter filling it is not a Mott isolator that emerges but a different strong coupling phase. The strong coupling phase appearing here wasn't further investigated. However, it should be noted that away from half filling no charge gap was found.

As before, the information above is combined into a single phase diagram in figure 4.36. The errorbars are obtained from the finite "resolution" in n. Near the phase boundary there is always one filling N which is in one phase and a filling $N + 1$ which is in the other phase. We can't tell where the phase boundary lies in between without increasing the system size. Therefore, the errorbars are simply given by the finite "resolution" due to the finite system size of $L = 128$. From the energies we also calculated the chemical potential at the boundaries

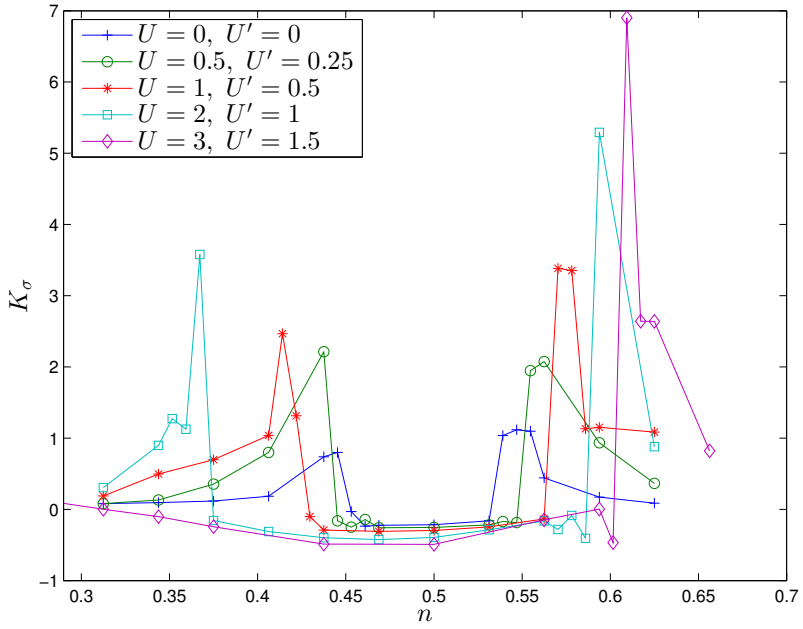

Figure 4.35: Luttinger Liquid coefficient $K_\sigma(128)$ for different interaction strengths U and U' and as a function of n for $B = 0.1$ and $\alpha = 1$.

$$\mu(N + \frac{1}{2}) = E(N + 1) - E(N). \tag{4.14}$$

We simply took the two energies, with N in one phase and $N + 1$ in the other phase. In figure 4.37 the phase diagram is given now for μ and U.

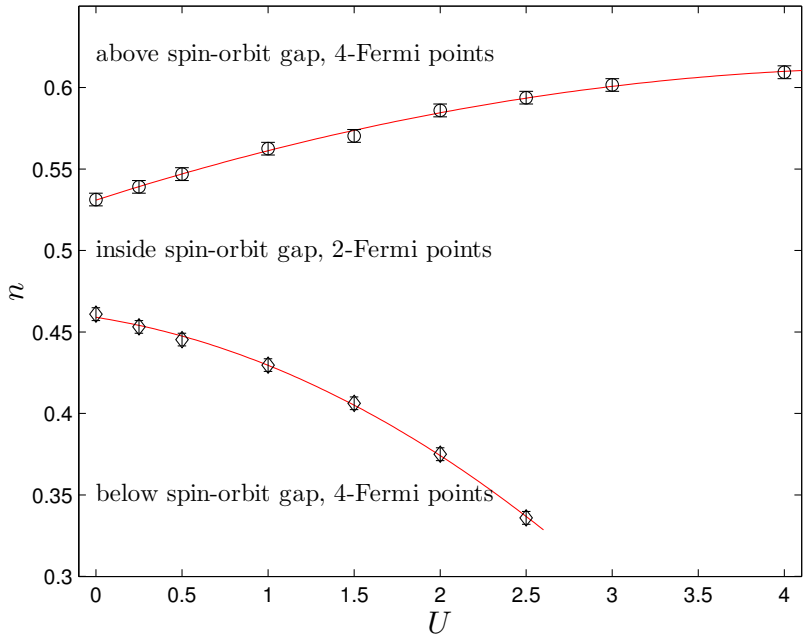

Figure 4.36: Phase diagram for n and U. The nearest-neighbour interaction is always $U' = U/2$. The red-lines are quadratic fits.

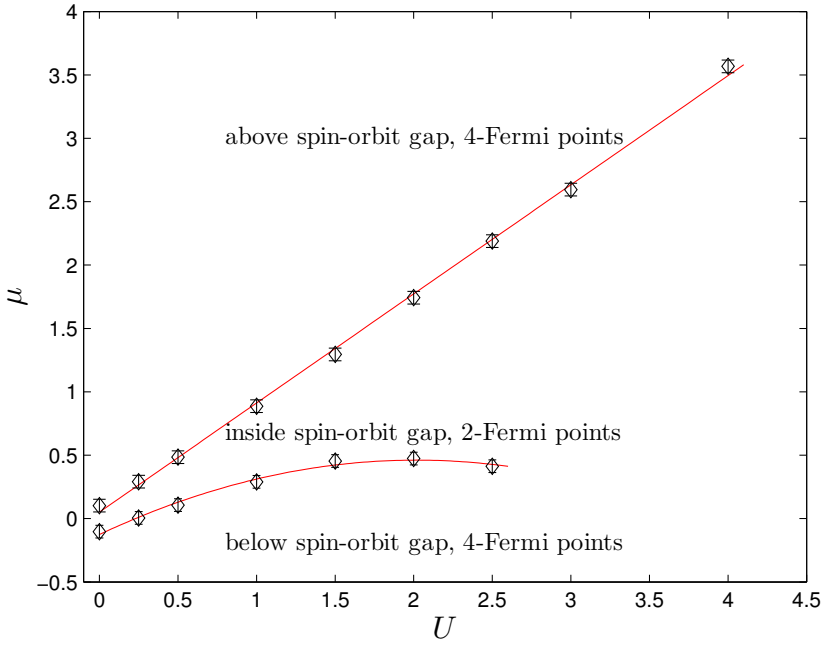

Figure 4.37: Phase diagram for μ and U. The nearest-neighbour interaction is always $U' = U/2$. The upper red line is a linear fit, the lower a quadratic fit.

4.5 Phase boundary to the Mott insulator

In the section 2.2.3 we learned that the extended Hubbard model has a transition to a Mott insulating state at quarter filling. Our model is an expansion to the extended Hubbard model and therefore we also expect some kind of transition to a strong coupling phase with high spatial ordering. Indeed, we did find from our analysis of the spectral densities in section 4.3 that the system exhibits a charge gap for high interactions if $U' \neq 0$. We call this strong coupling phase a Mott insulator since it shares its caracteristics with the Mott insulator in the extended Hubbard model: a charge gap and the same kind of charge order (see figure 2.6). In an ordinary Mott insulator the spin sector would be unaffected from the Mott transition, which takes place only in the charge sector. However, we did find some weird behaviour in the spin sector (compare figure 4.25 to 4.26) which indicates that it isn't totally unaffected. This might be due to the spin anisotropy in the system which allows an instability in the spin sector to become relevant.

4.5.1 Single particle excitation gap

The single particle excitation gap was already calculated in figure 4.16. The openening of a charge gap is one of the most distinctive features of the Mott insulator phase. In figure 4.38 we give again the single particle excitation gap, but now for much larger system sizes up to $L = 512$. We keep a matrix dimension of $m = 1000$ during the simulations. We also employed the same extrapolation technique to infinite system sizes as for the Luttinger liquid coefficients. We plotted Δ_L^1 as a function of $\frac{1}{L}$ and then fitted the data points with a polynom of fourth order. The fit is then used to obtain the values in the thermodynamic limit at $\frac{1}{L} = 0$. We see that all single particle excitation gaps scale to zero except at $U = 6,\ U' = 3$. This extrapolation technique gives excellent results if the system is far from phase transitions. Near a phase boundary extrapolations can be problematic, as we found for the Luttinger liquid coefficients. We also found that all single particle excitation gaps scale to zero in the case $U' = 0$. This is not surprising because the quarter filled Mott isolator can only appear if finite range interactions are present.

4.5.2 Local spectral weight

In figure 4.14 and 4.15 we already compared the case of $U' = 0$ to $U' = \frac{U}{2}$. We want to do that again, but now for the local spectral weight at the boundary. Generally, interaction effects are more present near boundaries than in the bulk for Luttinger liquids.

The local spectral weight is obtained the same way as the spectral densities. The difference is that only the overlap on always the same site is measured. Therefore, it corresponds to a spectral density that is summed over all k-values, e.g.

$$\frac{1}{2\pi} \langle 0 | \, c_0(t) c_0^\dagger(0) \, | 0 \rangle = \sum_k \frac{1}{2\pi} \langle 0 | \, a_k(t) a_k^\dagger(0) \, | 0 \rangle \, . \tag{4.15}$$

The same four parts as for the spectral density have to be calculated separately. After a Fourier transform one gets the energy dependent local spectral weight. Linear prediction is then carried out, as it was done for the spectral densities.

The energy dependent local spectral weight was also calculated for 64 site systems at a boundary site. Due to the local measurements, one it is safe for the time evolution to reach

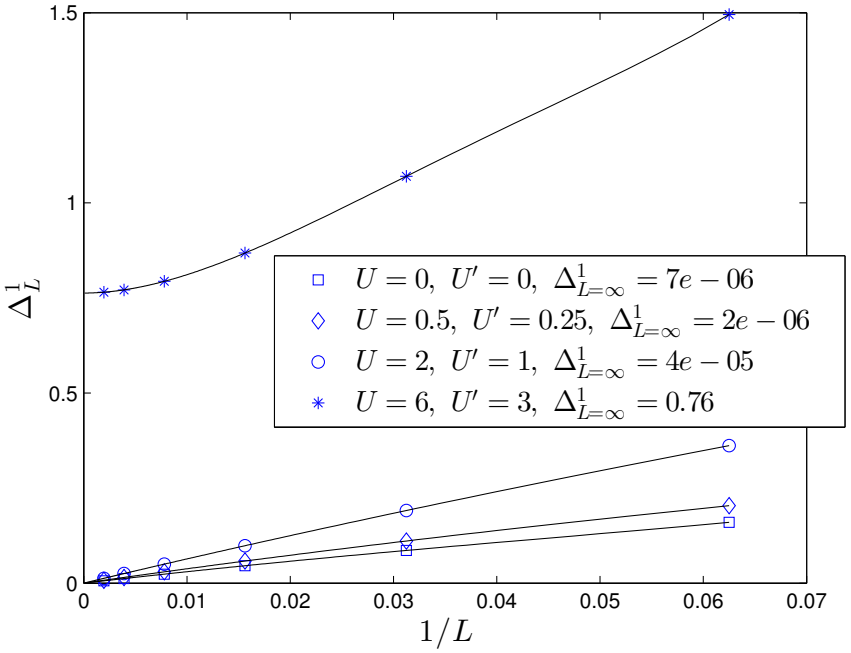

Figure 4.38: Single particle excitation gap Δ_L^1 for different values of U and U' with $\alpha = 1$ and $B = 0.2$ at quarter filling. $\Delta^1_{L=\infty}$ has been extrapolated by a fourth order polynomial fit.

the boundary. It is only important to stop the simulation before the evolution comes reflected back from the boundary to the site where the spectral weight is measured. Therefore, longer simulation times, or smaller system sizes, can be used. The case with $U' = U/2$ to $U' = 0$ is compared in 4.39 and 4.40. In both cases there is a clear suppression of the local spectral weight at the Fermi level, which is a well known Luttinger liquid result [33]. However, in the case of nonzero U' there is a wide energy gap that opens up. In the case of $U' = 0$ we also see a gap but not at the Fermi level. This gap separates the upper Hubbard band. This results again emphasize the different physics for onsite interactions and extended interactions. The resolution and reliability of this local spectral weight calculations was checked by comparing our results to results from functional renormalization group in appendix D.

4.5.3 Phase diagram

To make the phase diagram given in figure 4.33 complete, it is necessary to include the phase boundary to the Mott insulator. We employ two different methods for determining this boundary. Firstly, it can be detected by a nonvanishing charge gap. Secondly, by the Luttinger Liquid coefficient K_ρ which is zero inside a charge gap. However, due to the finite system size and logarithmic corrections K_ρ doesn't jump discontinouly to zero. For pinpointing the exact point of phase transition it is better to look at the critical value of K_ρ for the quarter filled Mott insulator. Fortunately, it is known from Luttinger liquid theory, that the critical value of K_ρ for the quarter filled Mott insulator is $K_\rho^* = 1/4$, see section 2.2.3. When using equation (3.92) one must be careful in which phase the system is.

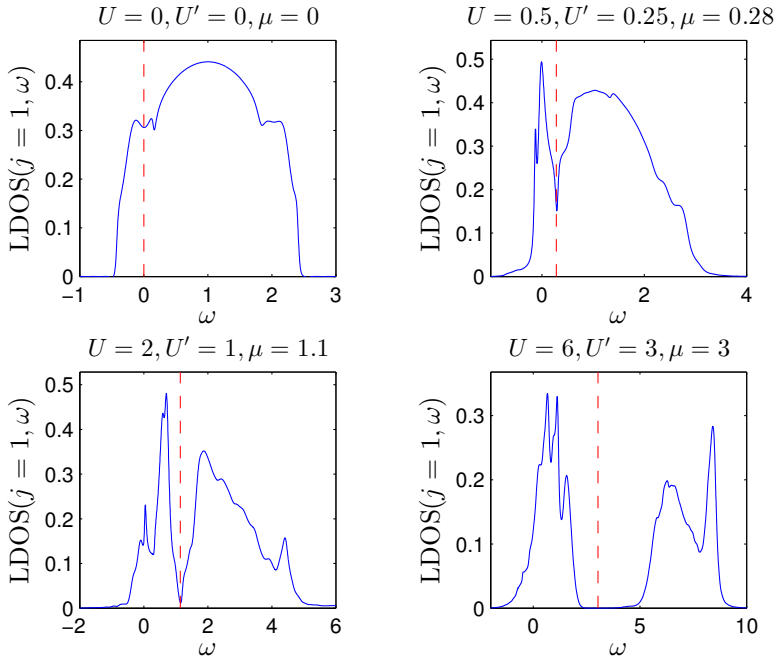

Figure 4.39: Energy dependent local spectral weight for different interactions with $U' = \frac{U}{2}$ and $\alpha = 1$, $B = 0.2$ at the boundary for a 64-site system. The dashed red line is the chemical potential.

Whenever the system was in the 4 Fermi-point phase we used the spinful fermion version of equation (3.92), which amount to dividing the K_ρ value from (3.92) by a factor of two.

In figure 4.41 we give the Luttinger liquid coefficient K_ρ as a function of U (with $U' = \frac{U}{2}$) for different spin-orbit couplings. We observe that it goes to zero at high interactions, but it is not a very sharp boundary. Therefore, the intersection with the critical coefficient $K_\rho^* = 0.25$ is used as the boundary. Generally, we observe that the spin-orbit coupling supresses the Mott insulating phase.

Until now, we approximated the charge gap by the single particle excitation gap. This is valid as long the energy is not dominated by pairing effects. We found indications of small pairing effects during the calculation of the Luttinger liquid coefficients as a function of N, see figure 4.34. Therefore we now use the two particle excitation gap, which gets rid of pairing effects by adding/removing two particles, instead of only one, from the system.

$$\Delta_L^2 = (E(L, N+2) + E(L, N-2) - 2E(L, N))/2 \tag{4.16}$$

If pairing is absent both the single and two particle excitation gap become the charge gap in the thermodynamic limit. For comparisons with the single particle spectral density, however, it is advantageous to take the single particle excitation gap. We plotted the two particle excitation gap as a function of U for three different spin-orbit couplings in figure 4.42. Again we see that with stronger spin-orbit coupling the charge gap opens up at stronger interactions. Generally, we find that the information about the phase boundary is the same from figure 4.41 and 4.42.

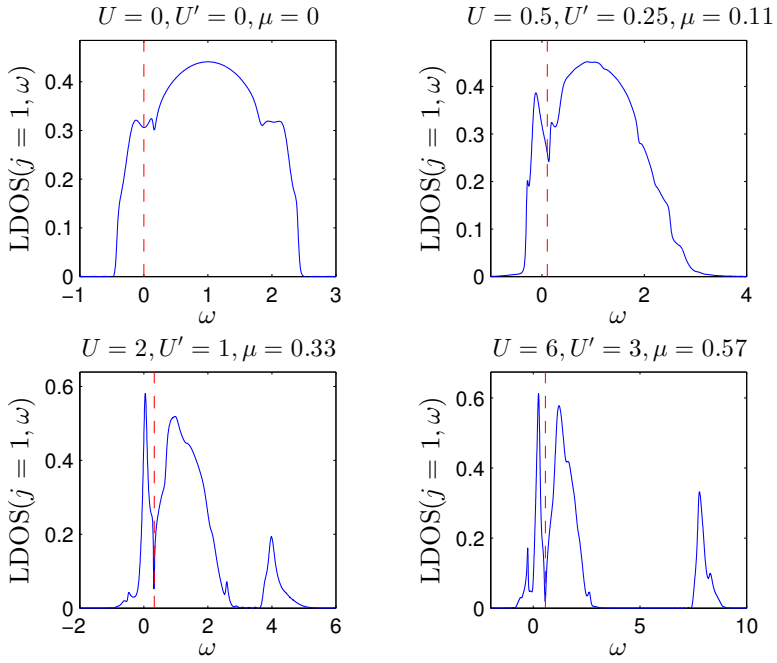

Figure 4.40: Energy dependent local spectral weight for different interactions with $U' = 0$ and $\alpha = 1$, $B = 0.2$ at the boundary for a 64-site system. The dashed red line is the chemical potential.

Therefore, we can use both of these two methods to obtain the phase boundary. The final phase diagram, including the boundary to the Mott insulator, is given in figure 4.43. For the boundary we took the U-value where K_ρ reaches the critical value $\frac{1}{4}$. We estimated an error of 0.05 in the coefficient K_ρ. Then from the slope in $K_\rho(U)$ we estimated the error in U, which is shown in the phase diagram. It is interesting to note how the Mott insulator gets supressed with stronger spin-orbit coupling. If the system is in a 2 or 4 Fermi point phase doesn't seem to be very important for the Mott insulating phase. In the middle part of the phase diagram, the 2 Fermi point phase, the system can be related to the spiral Luttinger liquid. In the 4 Fermi point phases we also have some kind of spinful Luttinger liquid, albeit with two different Fermi velocities for the spin and charge degrees of freedom. The Mott insulator has no Fermi point at all and is therefore not described by a metallic Luttinger liquid.

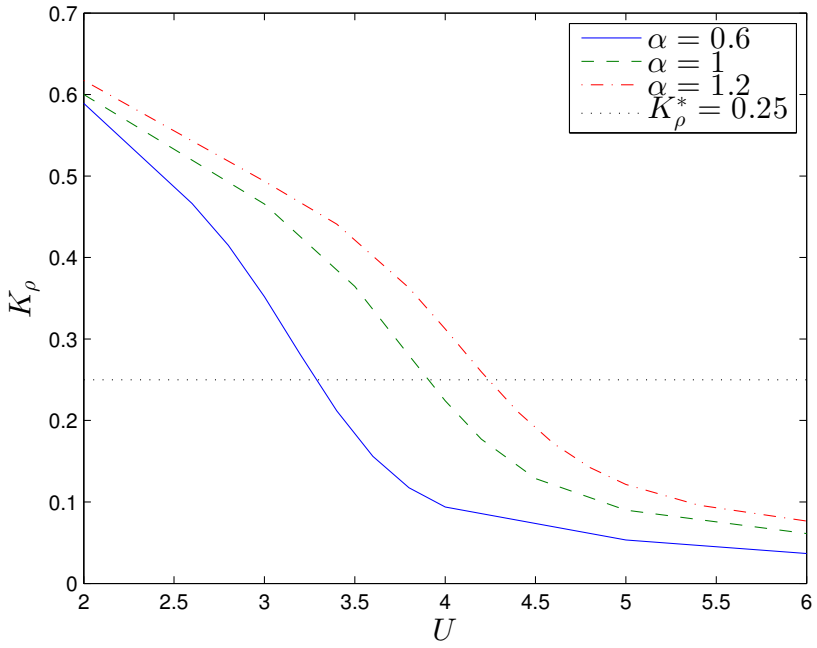

Figure 4.41: Luttinger Liquid coefficient K_ρ as a function of the interaction strength U ($U' = U/2$) for different values of α with $B = 0.1$ and quarter filling.

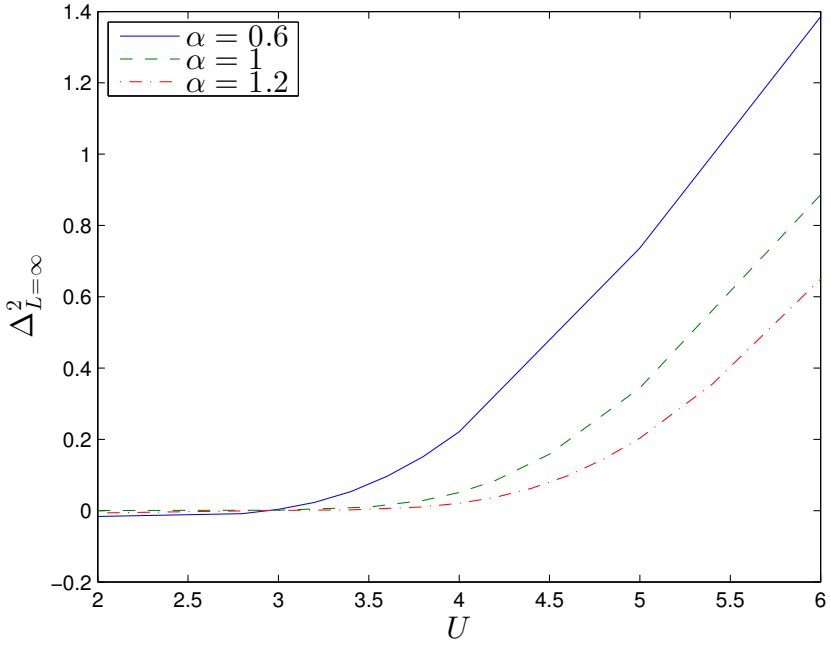

Figure 4.42: Two-particle excitation gap as a function of the interaction strength U ($U' = U/2$) for different values of α with $B = 0.1$ and quarter filling.

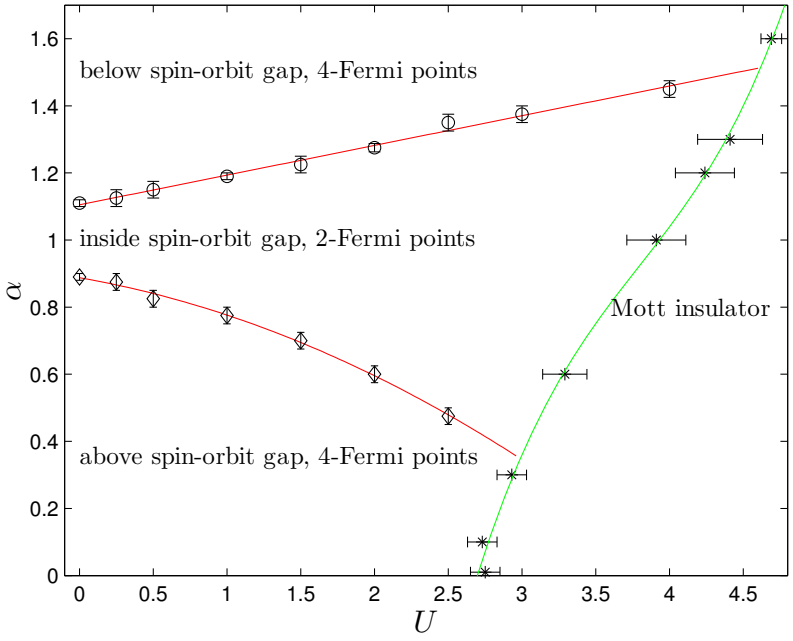

Figure 4.43: Phase diagram for α and U with the nearest-neighbour interaction $U' = U/2$. The other parameters are $B = 0.1$ and quarter filling. The upper red line is a linear fit, the lower a quadratic fit. The green line is a third order fit and it shows the phase boundary to the Mott isolator.

4.6 Breather bound states inside the spin-orbit gap

Here we will try to find the breather states described in section 2.2.2. Until now we looked only at the single particle spectral density. Breathers are bound states, therefore in order to observe them at least two particle excitations have to be applied to the ground state. Specifically, we will look at the optical conductivity, obtained from the dynamical current-current correlation function.

We will also try to compare our results to field theoretical spiral Luttinger liquid calculations. We use the results of Dirk Schuricht [34] here, who kindly allowed us to use his code for the field theory calculations. The field theory uses five parameters we have to obtain first: K_ρ, K_σ, v_ρ, v_σ, Δ^{SO}. First we discuss on how to obtain them in a reliable way.

The physics of the breathers takes place at the low energies inside the spin-orbit gap. Since we can't enhance our energy resolution arbitrarily we have to adapt our parameters for an enhanced gap. Therefore, we will use a magnetic field of $B = 0.3$ in this section, otherwise the other parameters stay the same. The helical spin order at opposite Fermi points is not necessary here, hence we can savely use a larger magnetic field.

4.6.1 Determination of the parameters for the field theory calculations

We already learned in section 4.3.1 how to obtain the spin-orbit gap from the spectra. The spin-orbit gap is also visible in the local density of states (LDOS). Since the LDOS is calculated at only one site, measurements are less time consumptive and it is also safe for the time evolution to reach the boundary. One only has to take care that the reflected signal doesn't reach the site where the measurements are done. Therefore, longer time evolutions and hence a better energy resolution are feasible with this method. The LDOS is plotted in figure 4.44. We also indicated the measured spin-orbit gap, the region around μ where the LDOS suddenly drops, with the vertical dashed green lines. The oscillations, we see in the LDOS for low interactions, are consistent with the finite system size and therefore also finite number of eigenenergies.

We also already have experience in determining the Luttinger liquid coefficients. Note that for comparisons with the spiral Luttinger liquid K_σ is obtained from the spin correlation in $\hat{S}^y$ direction. The finite size scaling is plotted in figure 4.45 for system sizes up to $L = 256$ and matrix dimensions of up to $m = 1000$. This method gives reliable results for K_ρ, but the K_σ are not very reliable due to the unknown logarithmic corrections. Remember figure 4.25 where we calculated K_σ for an extended Hubbard model. The result should be 1 all the time for a spin symmetric system. The results we obtain here goes in the right direction, $K_\sigma > 1$ for the interacting system, but their numerical value cannot be trusted. We suspect the true K_σ to be always much closer to 1.

For the determination of the the charge velocity v_ρ and the spin velocity v_σ we calculate the dynamical charge and spin structure factors $S_{NN}(k,\omega)$ and $S_{S^yS^y}$ in figure 4.46. Note that the expectation value of the density $\hat{n}_i$ is generally not zero, therefore we have to subtract the background for $S_{NN}(k,\omega)$, see also equation (3.90). Due to numerical errors the background won't stay constant over the time evolution, leading to small errors in the time evolution that add up to a large error after the Fourier transform. Special care must be taken, therefore. We used a smaller Trotter step of $\tau = 0.01$ for these simulations to keep Trotter error especially low. Matrix dimensions of $m = 1200$ where used. We still had to remove a small constant part in $S_{NN}(k,\omega)$ which gives unphysical results for $k = 0$.

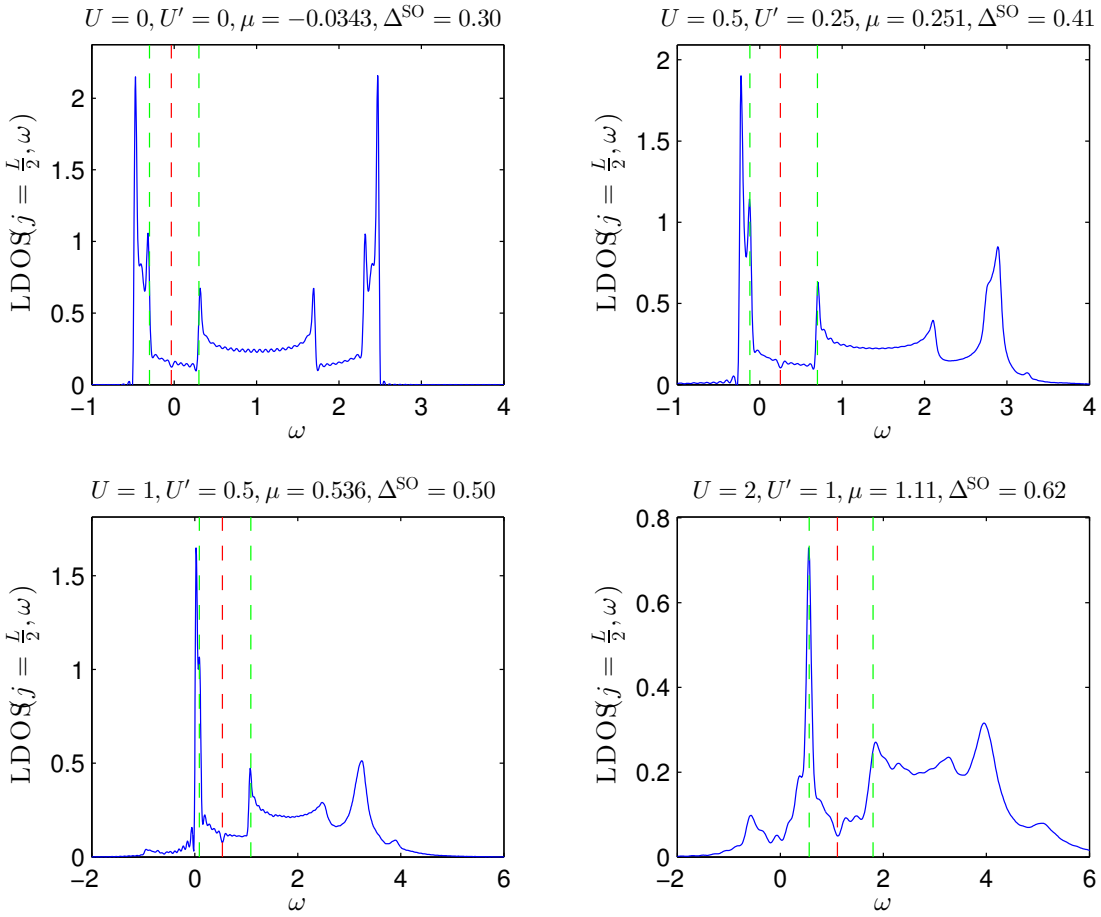

Figure 4.44: Local density of states different interactions with $U' = \frac{U}{2}$ and $\alpha = 1$, $B = 0.3$ in the middle for a $L = 128$ sites system. The dashed red line is the chemical potential and the two vertical dashed green lines mark the spin-orbit gap.

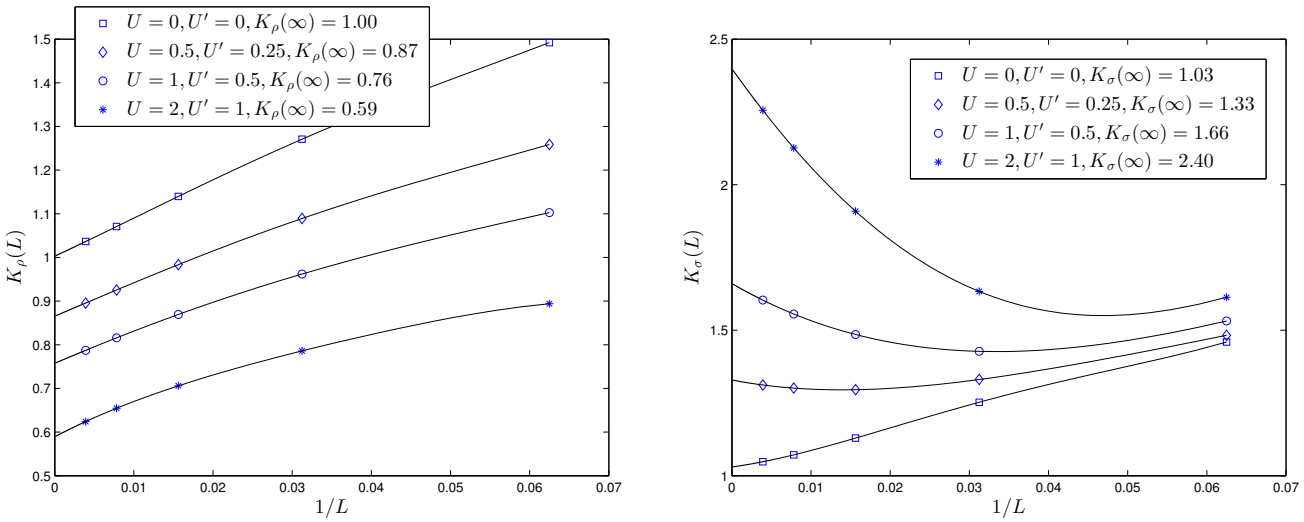

(a) (b)

Figure 4.45: Luttinger Liquid coefficient $K_\rho(L)$ (a) respectively $K_\sigma(L)$ (b) at quarter filling for different interaction strengths U and U', $\alpha = 1$, $B = 0.3$. $K_{\rho/\sigma}(\infty)$ has been extrapolated by a fourth order polynomial fit, the value is given in the legend.

After the simulations of the dynamical structure factors we tried to fit the velocities v_ρ and v_σ. For the gapless modes a linear dipersion starting at $k = 0$ symmetrically in both directions is expected. The downward pointing bow at energies $\omega \approx \Delta^{\mathrm{SO}}$ then represents the gapped modes. Unfortunately, due to the curvature of the dispersion relation, there is only a very short part in the vicinity of $k = 0$ and $\omega = 0$ suitable for fitting the velocities. We used the local maxima as the data points for the fitting. Combined with the low energy resolution the results are of very poor quality. Generally we can say that for the considered interactions $v_\rho \approx v_\sigma$, which also justifies dropping H_{mix} in (2.22). For the noninteracting case we should get $v_\rho = v_\sigma = 0.97$, whereas we get instead $v_\rho = 0.94$ respectively $v_\sigma = 0.96$.

The parameters we finally used in the field theoretical calculations are given in table 4.1. We didn't trust the results for K_σ, therefore we fitted K_σ so that the position of the first breather agrees with the numerical result. See equation (2.27) for the breather positions. We didn't calculate the velocities for $U = 2$ because the extraction is so inprecise anyway. We simply assumed for both the value 1.10 here.

4.6.2 Optical conductivity

The optical conductivity is obtained from the imaginary part of the current-current correlation, see equation (2.28). The current operator from equation (4.7) is used. The calculation is analogous to the spectral densities. We calculate the time evolutions on a $L = 200$ site system with $t_{\max} = 42.5$. A matrix dimension of $m = 1200$ is used. We observe that the entanglement grows slower with a j excitation, than a single particle excitation. Therefore, the longer simulation times were feasible. This allowed us to use little linear prediction, up to time 140.5, for accurate results. Since these breather states are very long-lived oscillations, it is better in this case to renormalize the λ_i with $|lambda_i| > 1$ to 1 during the linear

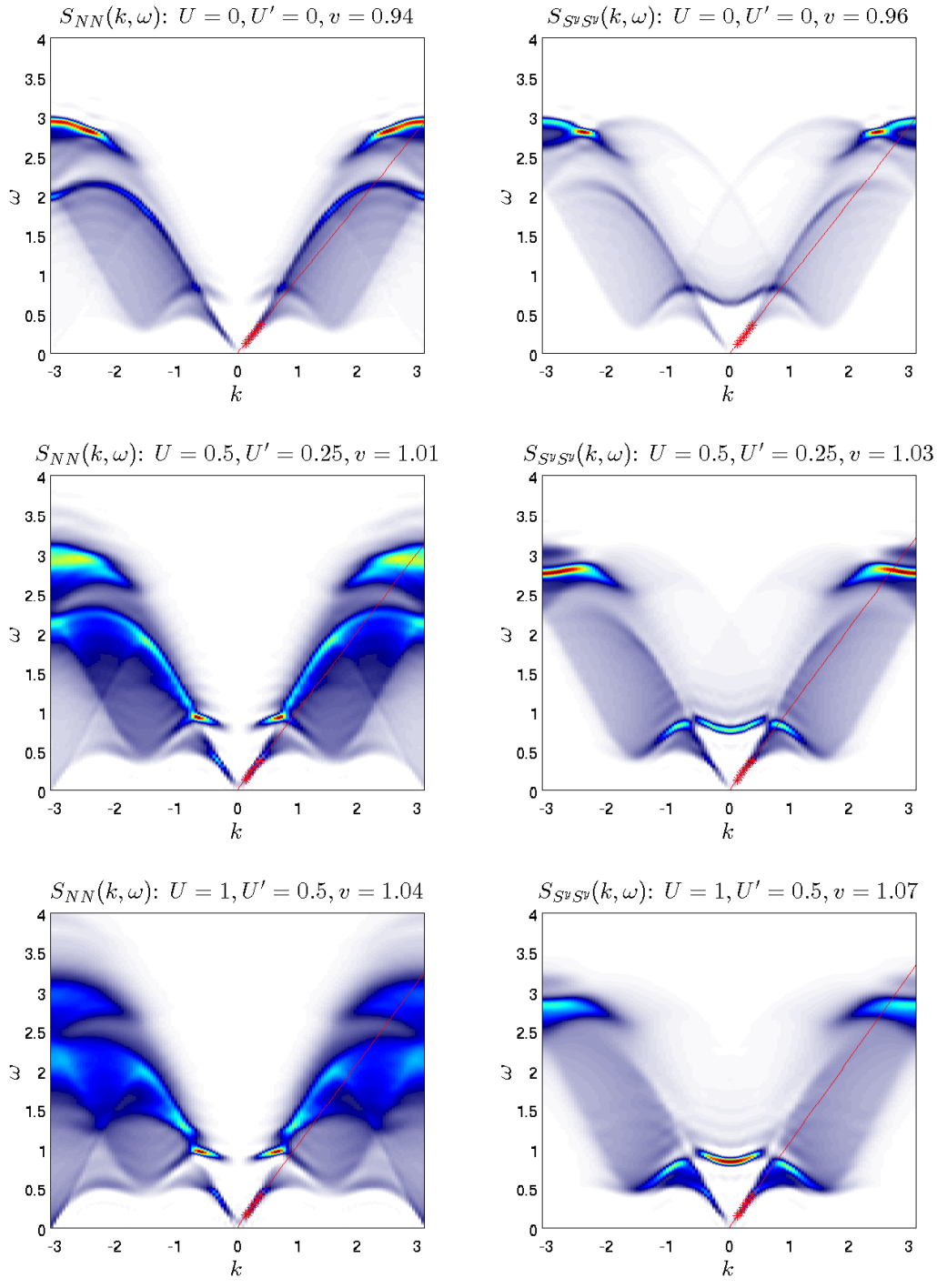

Figure 4.46: Structure factors for quarter filled systems with length $L = 128$ and $\alpha = 1$, $B = 0.3$ at different interactions. The plots on the left hand side are charge structure factors $S_{NN}(k,\omega)$ and on the left hand side is the spin structure factor $S_{S^yS^y}(k,\omega)$. The slope of the red line corresponds to the measured charge/spin velocity. The red stars mark the data points used in the fit.

U	K_ρ	K_σ	v_ρ	v_σ	Δ^{SO}
0	1.00	1.00 (1.03)	0.97 (0.94)	0.97 (0.96)	0.30
0.5	0.87	1.20 (1.33)	1.01	1.03	0.41
1	0.76	1.28 (1.66)	1.04	1.07	0.50
2	0.59	1.29 (2.40)	1.10*	1.10*	0.62

Table 4.1: Parameters used for the field theoretical calculations with $\alpha = 1$ and $B = 0.3$ and $U' = \frac{U}{2}$. K_σ was fitted so that the position of the breather peak in figure 4.47 fits to the numerical result. The calculated values of K_σ are set in parentheses. The velocities v_ρ and v_σ are known for $U = 0$. The measured values are set in parentheses again. For $U = 2$ no velocities have been measured. Therefore, the assumed values of 1.10 are marked with an asterix.

prediction, than rather set them to 0. The optical conductivity is presented in figure 4.47.

The field theoretical result was convoluted with the same Dolph-Chebyshev window as the numerical data. We also scaled the field theoretical result so that the first breather has the same height. It agrees very well for the noninteracting case. In the interacting cases, the big peak is the contribution from the first breather. The continuum at energies higher than the gap $2\Delta^{\mathrm{SO}}$ represents the soliton-antisoliton continuum. Generally, we observe that the field theoretical result drops slower at high energies than our numerical calculation. This may come from the fact that the field theory assumes linear dispersion relations, whereas our model has a finite bandwidth. The agreement between the two optical conductivities is good, but one should keep in mind that we had to adapt K_σ due to the unreliable data available. Also, since the first breather represents a delta peak in the optical conductivity, the shape of the two results will agree if the same window function is used.

4.6.3 Direct observation of breather bound states

We remarked in section 2.2.2 that the breather states have their name from the oscillations in their time evolution. We tried to visualize this oscillations by directly exciting breather bound states and then looking at the time evolution in figure 4.48. To know how to excite these bound states directly one only has to look at the dispersion relation in figure 2.5. We need both a particle and hole excitation near $k = 0$. One has to be careful about the spin directions, though. The particle has spin $\uparrow$ and the hole is to be generated in a see of spin $\downarrow$ electrons. We choose a density excitation in the + direction, the positive eigenvalue $\hat{S}_x$ eigenstate, for this purpose

$$(\sum_x \exp(-\frac{(x-x_0)^2}{2\tilde{\sigma}^2}) c^\dagger_{x+})(\sum_{x'} \exp(-\frac{(x'-x_0)^2}{2\tilde{\sigma}^2}) c_{x'+}). \tag{4.17}$$

As before we take $\tilde{\sigma} = 4$, which corresponds to a width of $\sigma = 0.25$ in k-space. The breather bound state itself has a positve magnetization $\hat{S}^z$, therefore we use this observable in figure 4.48. We can clearly see the zigzag oscillations of the breather bound state during the time evolution. The frequency of oscillation corresponds to its energy. We already observed such oscillations in the context of the noninteracting time evolutions in figure 4.6. We only had to use a single particle excitation back then, because the system was empty. However, the idea why the zigzag movement occurs is essentially the same for both the breathers and

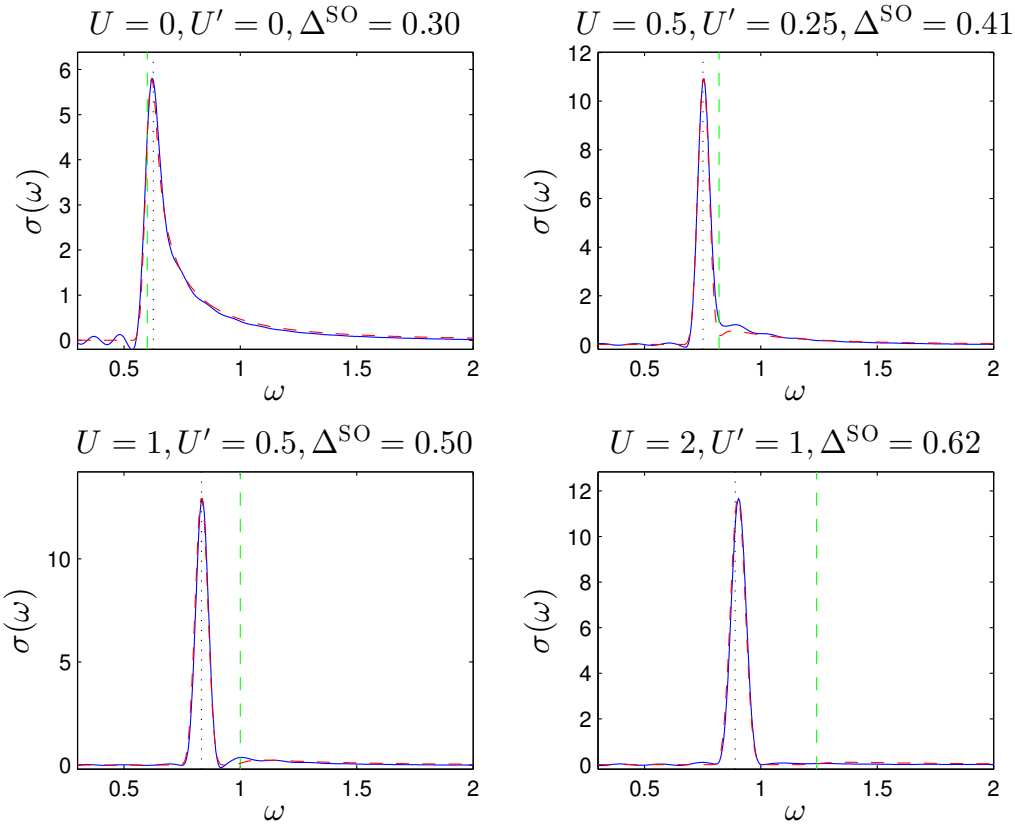

Figure 4.47: Optical conductivity $\sigma(\omega)$ for different interactions. The solid blue lines are the numerical result, the dashed red lines are the field theoretical results from the calculations of Dirk Schuricht [34]. The parameters are taken as in table 4.1. The vertical dashed green lines mark the size of the spin-orbit gap extracted from the density of states in figure 4.44. The vertical dotted black line marks the frequency of the breather measured in figure 4.48.

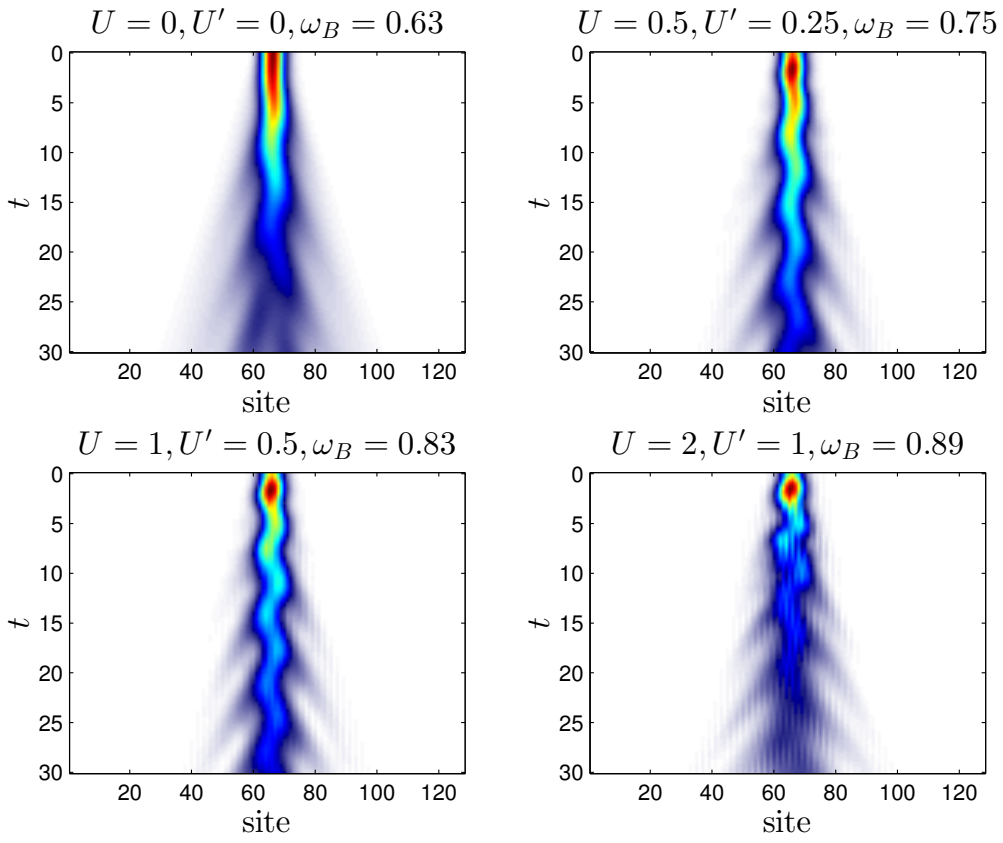

Figure 4.48: Spin expectation value $\hat{S}^z$ after a gaussian $c_+^\dagger c_+$ excitation in quarter filled systems with length $L = 128$ and $\alpha = 1$, $B = 0.3$ at different interactions. The frequency of the oscillation ω_B is given in the title. The background was subtracted.

the single particle excitations at $k = 0$. The frequency of the oscillation can be determined accurately by looking at the current density j (also $\hat{S}^y$ or $\hat{S}^x$ work well), see also figure 4.7. The energies of the first breathers in figure 4.47 are in very good agreement with the frequencies obtained here. One can also observe that the breather states are stabilized due to the interaction. The breather state at $U = 1$ lives much longer than at $U = 0$. However, the Mott instability at higher interactions seemingly interferes with the stability of the breather states.

Chapter 5

Conclusions

We investigated an one-dimensional extended Hubbard chain with additional Rashba spin-orbit coupling and an external magnetic field. This system exhibits a pseudogap, the spin-orbit gap, in one half of the conduction modes, when the Fermi momentum is commensurate with the momentum shift introduced by the spin-orbit coupling. Due to the nontrivial mixing of the spin and charge degrees of freedom the system has some peculiar spin-dependent conduction properties. The helical spin order - opposite Fermi points have orthogonal spin directions - leads to interesting prospects for the system in spintronics applications. The direction of movement of the electron is directly coupled to its spin direction. The Luttinger liquid theory has various low energy models available for the system.

We simulated this Hamiltonian using MPS methods, especially the DMRG for ground state calculations and TEBD for time evolutions. In the first part (cf. section 4.2), we looked at the time evolutions of empty systems after single particle excitations. The results were explained by the properties of the noninteracting dispersion relations derived in section 2.1. Gaussian excitations, with a finite width in real space and in k-space, proved to be very useful for investigating the dispersion relations. We showed how the specific gap energies of the spin-orbit gap, and an optional superconducting gap, translate into oscillations clearly visible in the time evolution.

A direct extension of the time evolutions above are the spectral densities obtained in section 4.3. The procedure to obtain them can be easily implemented using standard MPS methods, as has been shown in section 3.4. We used the spectra to investigate the interaction effects on the noninteracting dispersing features. Hubbard and extended Hubbard type interactions were compared. For both we confirmed that the spin-orbit gap gets enhaced with repulsive interactions, as is predicted by Luttinger liquid theory. Furthermore, for the extended Hubbard type interactions a gapped strong coupling phase emerges, which was then identified as a quarter-filled Mott insulator. Quite generally, we found that the interaction effects are much stronger with finite range interactions, than with onsite interactions. By looking at the spectra corresponding to a single spin species, we confirmed that the helical spin order holds as long as the system is a Luttinger liquid. Furthermore, we looked also at the spectra outside the spin-orbit gap, the 4 Fermi point phase, and compared them to spectra inside the spin-orbit gap, the 2 Fermi point phase.

Then we calculated the Luttinger liquid coefficients, as described in section 3.5. We found that they have a different form in the 2 and 4 Fermi point phases, therefore a jump occurs at the phase transition. We used this jump to distinguish the 2 and 4 Fermi point phases

in section 4.4. Two-dimensional phase diagrams were obtained for the interaction and the spin-orbit coupling, or respectively the interaction and the filling. Again, we found that the parameter range of the 2 Fermi point phase is drastically enhanced with interactions for both cases. Furthermore, we found that although the charge coefficient K_ρ could be obtained with reasonable accuracy, the results for the spin coefficient K_σ are not very reliable. One of the reasons is that the good quantization axis of the system is generally k-dependent, leading to strange spin correlation functions from which K_σ was extracted.

The Mott insulating phase, appearing at very strong interactions, has been investigated in section 4.5. By looking at local spectral weight calculations we confirmed that that a quarter-filled Mott insulator doesn't emerge with only onsite interactions. Two observables for the phase transition to the Mott insulator were identified: the charge gap and the critical value of K_ρ. With their help we completed the phase diagrams by drawing the boundary to the Mott insulator. It was observed, that the spin-orbit coupling has negative effects on the charge order of the Mott insulator and therefore it emerges at higher interactions.

The spiral Luttinger liquid model predicts bound states, so-called breathers, with energies inside the spin-orbit gap for repulsive interactions (cf. section 2.2.2). We observed these breathers by looking at the optical conductivity obtained from the current-current correlation function (cf. section 4.6). The result was then compared to field theoretical calculations and we found them to be in good accordance, considering the approximations of the field theory. The breather bound states were then observed directly by looking at the time evolution after a suitable excitation. We could clearly see their oscillatory behaviour, from which stems their name, with the frequency of oscillation in accordance with the optical conductivity. These breather states confirm that a spiral Luttinger liquid is different from a helical liquid, also inside the pseudogap.

Appendix A

Test of the Hamiltonian

As a test of the Hamiltonian we replicate the results of Stoudenmire et al. [36]. This was mainly done to see if the Hamiltonian was correctly implemented in the MPO language and to test the performance of the programs. Stoudenmires Hamiltonian is exactly the same as the one we reasearched. To get to the topological properties he always used the additional Cooper pairing field, whereas most of the time we set $\Delta^{\mathrm{C}} = 0$. The Cooper pairing field destroys the particle number conservation, a symmetry which can be exploited in the DMRG and TEBD code. Without this symmetry smaller matrix dimensions m and hence smaller system sizes are achievable. Since our focus where not the topological properties of the system we didn't use the Cooper pairing field if not neccessary.

Furthermore, the topological phase with $\Delta^{\mathrm{C}} \neq 0$ corresponds to our 2 Fermi point phase at $\Delta^{\mathrm{C}} \to 0$. Therefore, we tried to see if some of the properties of the topological phase remain at $\Delta^{\mathrm{C}} = 0$ and can be used to distinguish the 2 Fermi point phase. The topological phase can be identificated among others by the following properties:

- Degenerate groundstate in the topological phase $\Delta E = |E_1 - E_0|$. This holds as long as the Majorana wave functions, residing at the boundaries, don't overlap too much.
- The spectrum of the bulk entanglement Hamiltonian should be two-fold degenerate in the topological phase: $\rho_L = Tr_R|\psi >< \psi|$ with the Entanglement Hamiltonian $H_E = -\ln \rho_L$.
- The majorana wavefunctions can be directly measured, see equation (12) and (13) in Stoudenmire.

We verified the first two points in figure A.1 and A.3. Since this was a proof of concept, we used a much smaller system size of $L = 100$ than Stoudenmire with $L = 400$. Therefore, the two-fold degeneracy in figure A.3 is not as accurate as in Stoudenmires work. We also found that these two properties don't remain at $\Delta^{\mathrm{C}} = 0$ in figure A.2 and A.4. Therefore, they are not suitable criteria for distinguishing the 2 and 4 Fermi point phases.

As a technical remark, we had some problems at first to replicate figure A.3, because our program can't conserve parity. The symmetry of charge parity remains with finite Cooper pairing field. For the calculation of the entanglement spectrum inside the topoligical phase it is vital that the investigated groundstate has parity +1. If the two parity sectors mix then the two-fold degeneracy is not visible anymore. Since the implementation of the DMRG

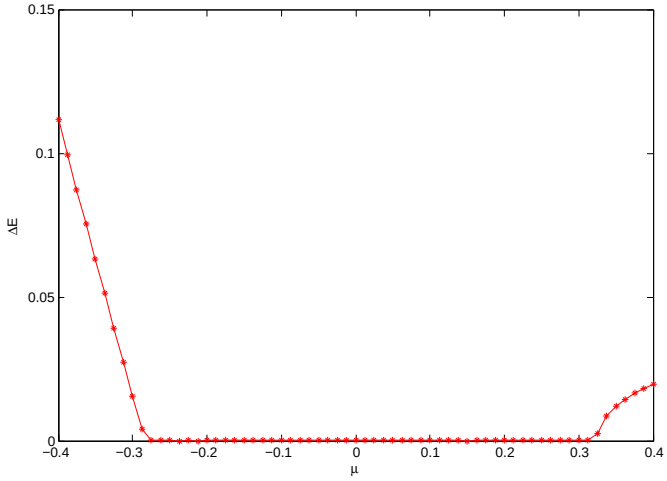

Figure A.1: Energy difference ΔE between the groundstate and the first excited state for a 100-site chain with $\Delta = 0.1$, $\alpha = 0.3$, $B = 0.3$, $U = 0.1$ and $\chi = 50$. Agrees with Stoudenmire [36] fig 2.

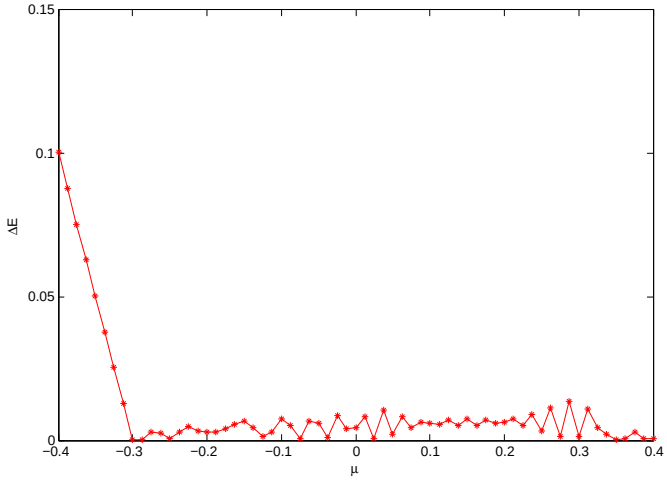

Figure A.2: Energy difference ΔE between the groundstate and the first excited state for a 100-site chain with $\Delta = 0.0$, $\alpha = 0.3$, $B = 0.3$, $U = 0.1$ and $\chi = 50$.

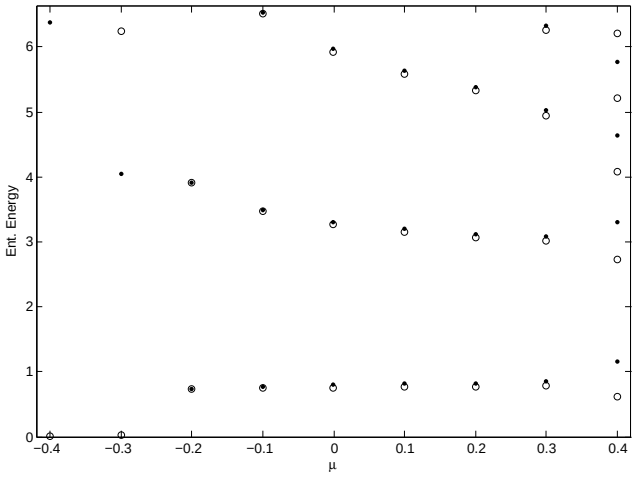

Figure A.3: Entanglement Energy spectrum for a 100-site chain with $\Delta = 0.1$, $\alpha = 0.3$, $B = 0.3$, $U = 0.1$ and $\chi = 100$. Agrees with Stoudenmire [36] fig 2.

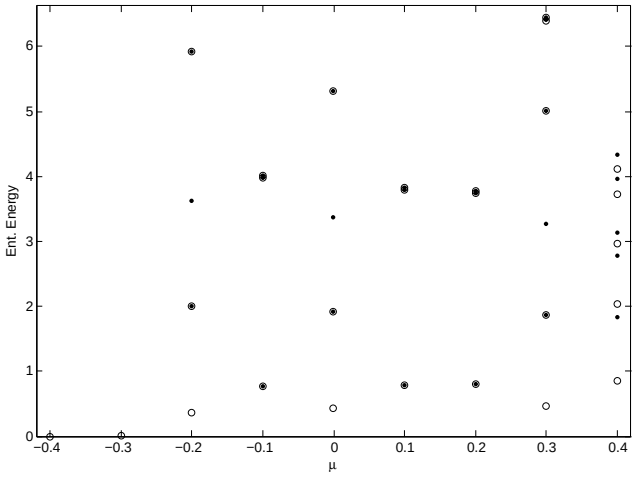

Figure A.4: Entanglement Energy spectrum for a 100-site chain with $\Delta = 0.0$, $\alpha = 0.3$, $B = 0.3$, $U = 0.1$ and $\chi = 100$.

algorithm we used can't conserve parity as a good quantum number, we projected the -1 parity sector out by application of the parity operator:

$$|0>_{+1} = |0>_{\text{mixed}} + P|0>_{\text{mixed}} \tag{A.1}$$

Figure A.3 was generated using this technique.

Appendix B

Test of the spectral densities

As a test the spectral density of an ordinary Hubbard model has been calculated in figure B.1. The results agree with the spectral function calculated by Jeckelman in 2008 with the DDMRG method [19]. A matrix dimension of $m = 400$ was used and the total cumulative truncated weights at the end ($t_{\max} = 20$) of the two simulations (in the particle and hole sector) were $\epsilon_{\text{tot}} = 0.04$ and $\epsilon_{\text{tot}} = 0.008$. The time evolution for the particle part was repeated with $m = 1000$ leading to a smaller final total cumulative truncated weight of $\epsilon_{\text{tot}} = 0.01$. The maximum absolute difference between the two spectra is 0.008 and by comparing the spectra by eye there is no visible difference. Therefore, we can say that the spectrum is already converged.

The spectral functions from figure 4.15 were tested for convergence in the matrix dimension m. Only the cases with high interactions $U = 2$ and $U = 6$ (and $U' = U/2$) were tested, because they lead to a higher entanglement during the time evolution. For both cases simulations for $m = 400$ and $m = 800$ were done. As before there is no visible difference for the spectra at the two different matrix dimensions m. For $U = 2$ the maximum absolute difference was 3.7×10^{-4} and for $U = 6$ it was 2.4×10^{-4}. Again there is no visible difference in the spectra between the different matrix dimensions.

The entanglement entropy is compared in figure B.2. As the entanglement entropy grows over time a higher m is necessary for describing the more entangled state. Therefore, the entanglement entroy is very sensible to m. The total cumulative truncated weight is given in figure B.3. It grows very fast even for the high m simulations. Therefore, it is computationally expensive to simulations to long times.

In all time evolutions, for calculating the spectral density, it was taken care that $t_{\max}$ is small enough so that the signal can't reach the boundary. Finite size effects can be minimized by this effort. However, the ground state still has finite size effects. Therefore it was not possible to get completely rid of them. In particular, we found a slight asymmetry in the spectra getting more distinct with stronger interactions. For one part this is due to numerical inaccuracies but the more important reason is an asymmetry stemming from the time evolution. If the system has an even number of sites it is not possible to start the initial excitation exactly in the middle, it is always one site off. Taking an odd number of sites this problem doesn't persist but it is not possible to have exactly quarter filling then. For the spectra in this work the mirrored part was added to symmetrize them. A comparison of the unsymmetrized spectra is given in fig B.4. It is especcially interesting to note that for $U = 6$ for $L = 63$ the hole part of the spectrum is extremely weak. The k-summated spectral

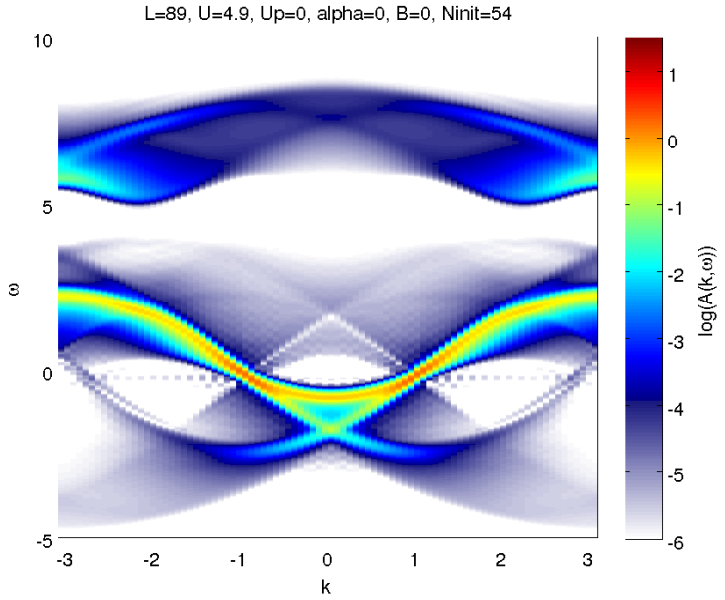

Figure B.1: Spectral density for a Hubbard model with $U = 4.9$ on a 90-site chain with filling $\rho = 0.6$. The result agrees with [19] figure 7.

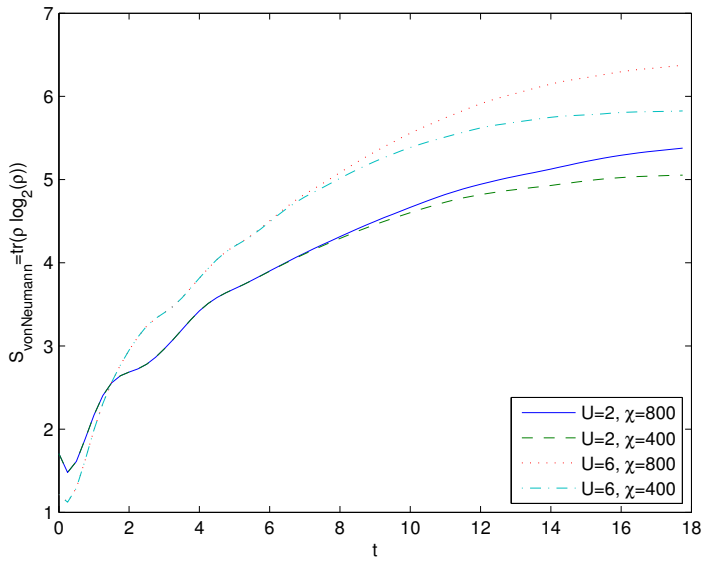

Figure B.2: Entanglement entropy in the middle of the chain for two different U and m values.

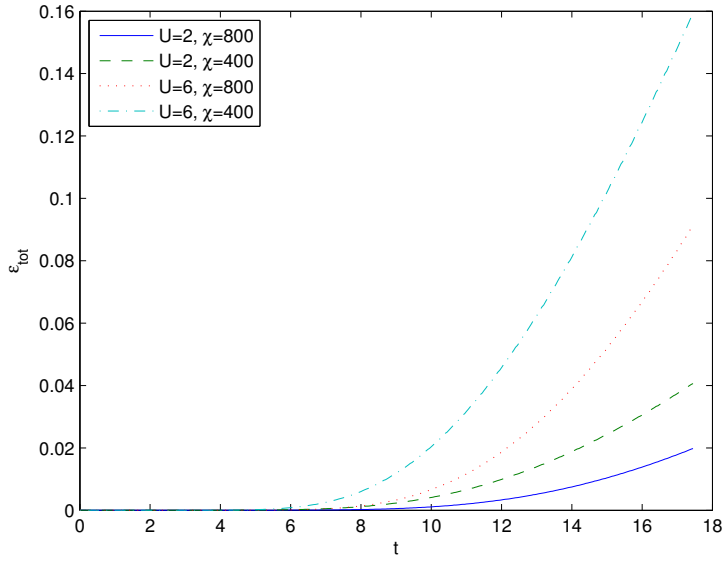

Figure B.3: Total cumulative truncated weight for two different U and m values.

density is the local density of state, which can be very site dependent for open boundary conditions especcially for the Mott phase with its strong spatial ordering. What causes the strong difference for even and odd sites at $U = 6$ can be seen in the local number densities in figure B.5. For $L = 64$ the number density in the middle is 0.476 and for $L = 63$ it is 0.136 which is very small compared to the filling 0.5. Therefore, in the Mott phase this approach of calculating spectral densities is questionable because of the strong site dependence.

We compare now possible finite size effects for the spectra in figure B.6 for two different system sizes $L = 64$ and $L = 128$. There are no qualitative changes between the two system sizes. The spectra of the bigger systems show more detail.

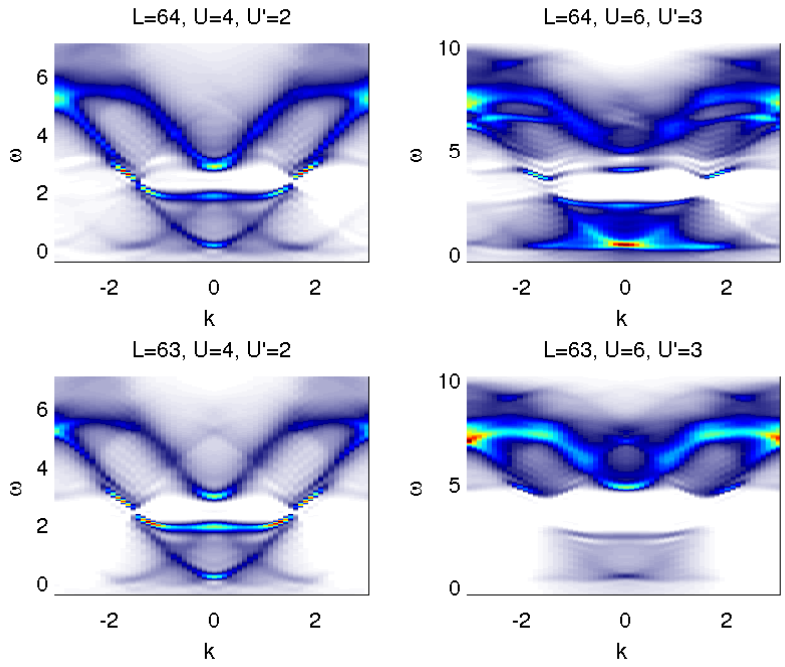

Figure B.4: Comparison of spectra for an even and odd number of sites for $\alpha = 1$, $B = 0.1$ and different interaction strengths. In both cases there are 32 in the system. Even odd effects are considerably strong and get stronger for more interacting systems.

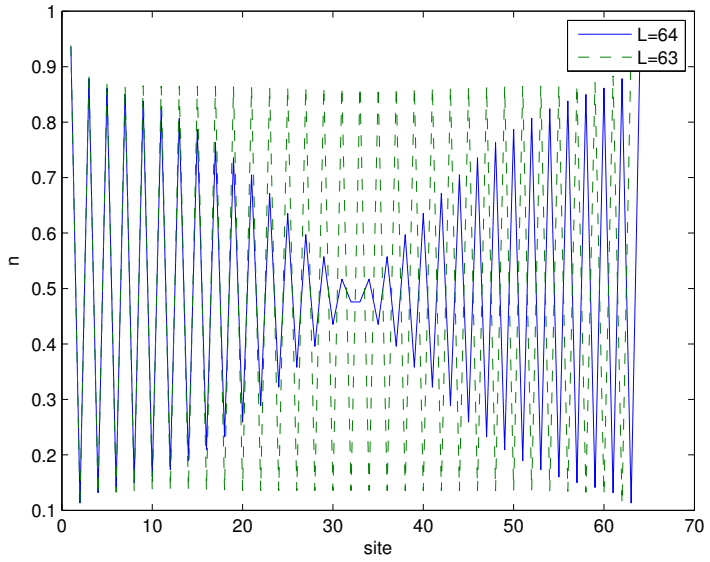

Figure B.5: Site dependent number density at $U = 6$, $U' = 3$ and $\alpha = 1$, $B = 0.1$ for an even and odd number of sites.

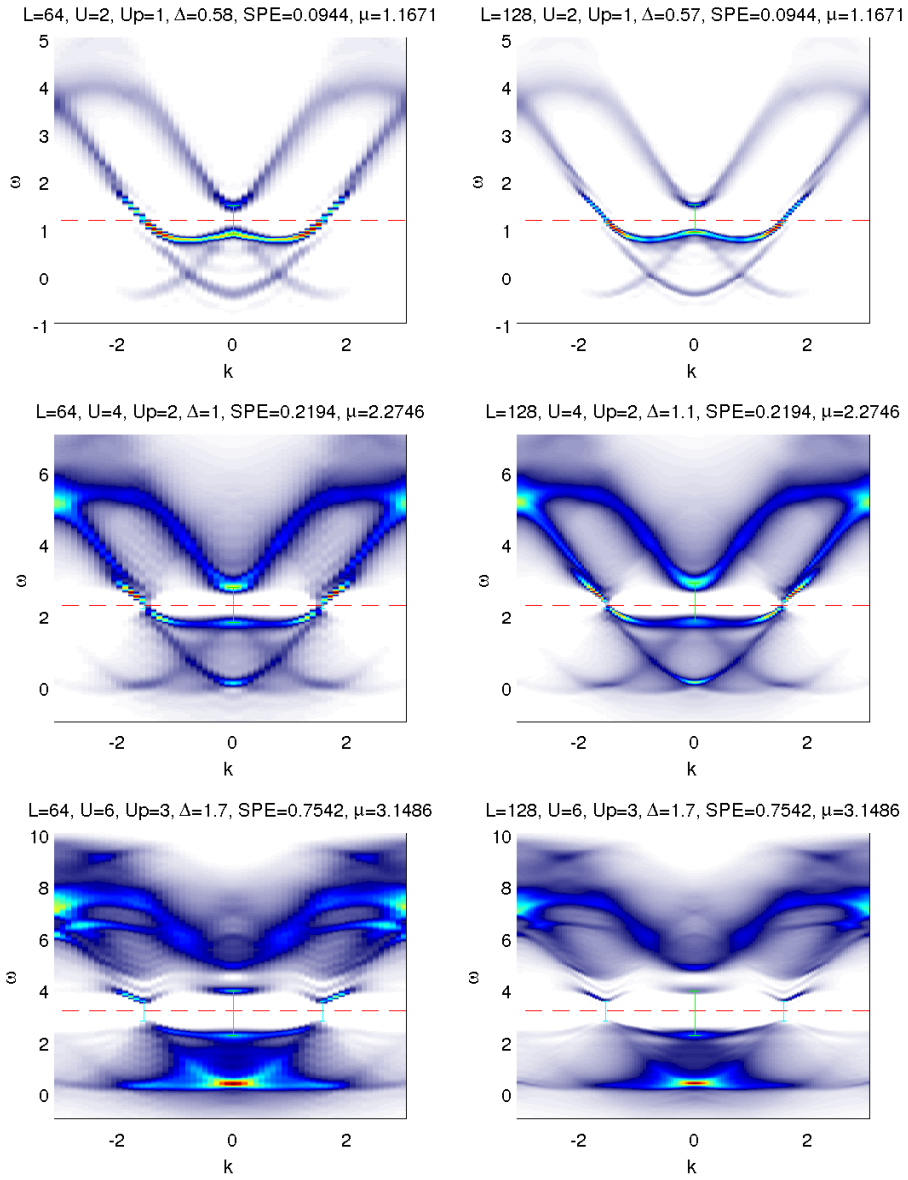

Figure B.6: Comparison of spectra for $\alpha = 1$, $B = 0.1$ and different interaction strengths. The left site shows a system size of $L = 64$ and the right site a system size of $L = 128$. All spectra are for quarter filling.

Appendix C

Alternative Calculation of Luttinger Liquid coefficients

The correct form of equation (3.89) for our system is not known, therefore equation (3.92) could be wrong. For testing purposes an alternative way of calclulating K_ρ has been implemented. The method presented here is most commonly used with the Bethe Ansatz and Quantum Monte Carlo. DMRG allows big enough system sizes to extract K_ρ directly from the correlations. This method is based only on groundstate energies and the energy of the first excited state [11]. The relations used here are textbook material and can be found in e.g. [15]. K_ρ is related to the compressibility by

$$K_\rho = \frac{\pi}{2} n^2 \kappa v_\rho. \tag{C.1}$$

For spinless fermions it translates to

$$K_\rho = \pi n^2 \kappa v_\rho. \tag{C.2}$$

The compressibility is calculated from the two particle charge gap

$$\frac{4}{n^2 L \kappa} = E_0(N+2, L) + E_0(N-2, L) - 2E_0(N, L). \tag{C.3}$$

The charge velocity can be obtained from the energy difference of the groundstate to the first excited state

$$\frac{2\pi v_\rho}{L} = E_1(N, L) - E_0(N, L). \tag{C.4}$$

Both functions given above scale to zero in a gapless system. The scaling is shown in fig C.1. They are fitted to a polynomial $f(L) = a_0 + \frac{a_1}{L} + \frac{a_2}{L^2} + ...$
Now $K_\rho(\infty)$ can be obtained by

$$K_\rho(\infty) = \frac{a_1^{v_\rho}}{a_1^{\kappa}}. \tag{C.5}$$

A table with a comparison of the results for K_ρ at $\alpha = 1,\ B = 0.2$ and different values of U and U' is given below:

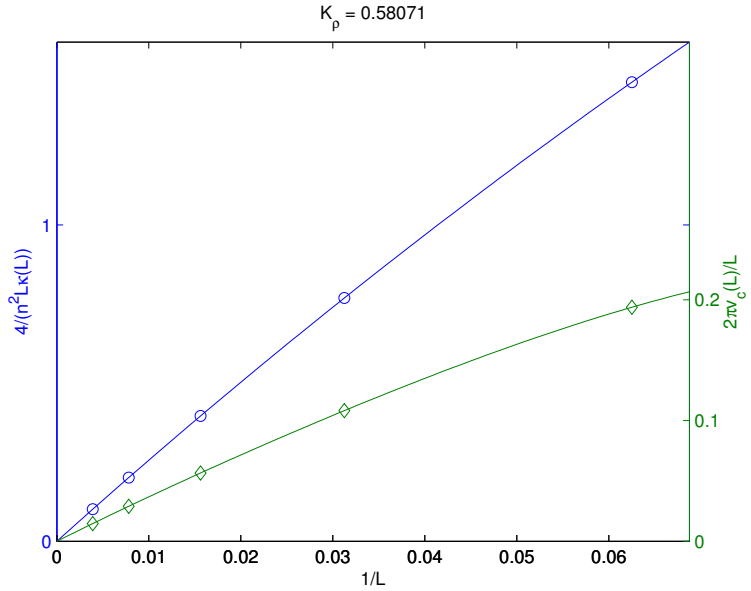

Figure C.1: Scaling of the two functions given by equations (C.3) and (C.4) for $\alpha = 1,\ B = 0.2,\ U = 2$ and $U' = 1$.

U	U'	K_ρ from correlations	K_ρ from energies
0	0	1.0064	0.9822
0.5	0.25	0.8694	0.8635
2	1	0.5914	0.5807
6	3	0.0311	-0.0261

The results agree pretty well. There is a small problem with equation (C.4). For K_ρ one needs to calculate the charge velocity v_ρ. However, in our system it is not possible to do strictly a charge excitation because spin is not a good quantum number. Therefore, the first excited state won't have exactly the same magnetization. The results agree good enough to believe that our calculation is valid.

Apart from this test only the method using the corellation function is used since it needs only one DMRG run. The alternate method based on energies needs at least four DMRG runs.

Appendix D

Test of the local spectral weight

Here we do a comparison of the energy dependent local spectral weight for an ordinary Hubbard model to results from the functional renormalization group (FRG) in [1]. Although, the achievable energy resolution is smaller with DMRG we can reproduce the results. In contrast to FRG our method isn't limited to small interactions.

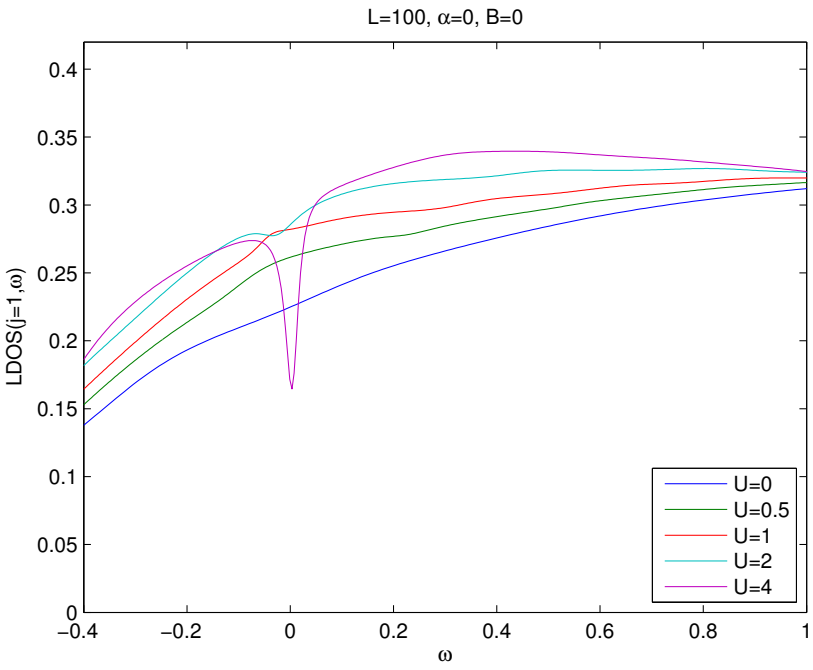

Figure D.1: Compare to [1] fig 5.

Bibliography

[1] S. Andergassen. Renormalization-group analysis of the one-dimensional extended hubbard model with a single impurity. *Physical Review B*, 73(4), 2006.

[2] Thomas Barthel, Ulrich Schollwöck, and Steven R. White. Spectral functions in one-dimensional quantum systems at finite temperature using the density matrix renormalization group. *Physical Review B*, 79(24):245101, June 2009.

[3] J.E. Birkholz. *Spin-orbit Interaction in Quantum Dots and Quantum Wires of Correlated Electrons - A Way to Spintronics?* 2008.

[4] Bernd Braunecker, Cristina Bena, and Pascal Simon. Spectral properties of luttinger liquids: A comparative analysis of regular, helical, and spiral luttinger liquids. *Physical Review B*, 85(3):035136, January 2012.

[5] Bernd Braunecker, George I. Japaridze, Jelena Klinovaja, and Daniel Loss. Spin-selective peierls transition in interacting one-dimensional conductors with spin-orbit interaction. *Physical Review B*, 82(4):045127, July 2010.

[6] Bernd Braunecker, Pascal Simon, and Daniel Loss. Nuclear magnetism and electron order in interacting one-dimensional conductors. *Physical Review B*, 80(16):165119, 2009.

[7] Bernd Braunecker, Pascal Simon, and Daniel Loss. Nuclear magnetism and electronic order in ^{13}C nanotubes. *Physical Review Letters*, 102(11):116403, 2009.

[8] A J Daley, C Kollath, U Schollwöck, and G Vidal. Time-dependent density-matrix renormalization-group using adaptive effective hilbert spaces. *Journal of Statistical Mechanics: Theory and Experiment*, 2004(04):P04005, 2004.

[9] Reinhold Egger and Hermann Grabert. Friedel oscillations in luttinger liquids. arXiv e-print cond-mat/9604026, April 1996.

[10] Satoshi Ejima, Florian Gebhard, and Satoshi Nishimoto. Tomonaga-luttinger parameters for doped mott insulators. arXiv e-print cond-mat/0507508, July 2005. Europhys. Lett., 70, 492 (2005).

[11] Satoshi Ejima, Florian Gebhard, Satoshi Nishimoto, and Yukinori Ohta. Phase diagram of the t–U–V_1–V_2 model at quarter filling. arXiv e-print cond-mat/0411151, November 2004. Phys. Rev. B, 72, 033101 (2005).

[12] M. Ganahl, M. Haque, and H. G. Evertz. Quantum bowling: Particle-hole transmutation in one-dimensional strongly interacting lattice models. arXiv e-print 1302.2667, February 2013.

[13] Martin Ganahl. Simulation of spin transport in one dimensional quantum heisenberg spin 1/2 systems in real time. Master's thesis, Graz University of Technology.

[14] Martin Ganahl, Patrik Thunström, Frank Verstraete, Karsten Held, and Hans Gerd Evertz. Chebyshev expansion for impurity models using matrix product states. *arXiv:1403.1209 [cond-mat]*, March 2014.

[15] T. Giamarchi. *Quantum Physics in One Dimension*. International Series of Monographs on Physics. Clarendon Press, 2004.

[16] R. P. Hardikar and R. T. Clay. Phase diagram of the one-dimensional hubbard-holstein model at half and quarter filling. *Phys. Rev. B*, 75:245103, Jun 2007.

[17] Andreas Holzner, Andreas Weichselbaum, Ian P. McCulloch, Ulrich Schollwöck, and Jan von Delft. Chebyshev matrix product state approach for spectral functions. *Phys. Rev. B*, 83:195115, May 2011.

[18] Eric Jeckelmann. Dynamical density-matrix renormalization-group method. *Phys. Rev. B*, 66:045114, Jul 2002.

[19] Eric Jeckelmann. Density-matrix renormalization group methods for momentum- and frequency-resolved dynamical correlation functions. *Progress of Theoretical Physics Supplement*, 176:143–164, 2008.

[20] Till D. Kühner and Steven R. White. Dynamical correlation functions using the density matrix renormalization group. *Phys. Rev. B*, 60:335–343, Jul 1999.

[21] Roman M. Lutchyn, Jay D. Sau, and S. Das Sarma. Majorana fermions and a topological phase transition in semiconductor-superconductor heterostructures. *Physical Review Letters*, 105(7):077001, August 2010.

[22] Tobias Meng, Lars Fritz, Dirk Schuricht, and Daniel Loss. Low-energy properties of fractional helical luttinger liquids. *Phys. Rev. B*, 89:045111, Jan 2014.

[23] S. Nishimoto, K. Sano, and Y. Ohta. Phase diagram of the one-dimensional hubbard model with next-nearest-neighbor hopping. *Physical Review B*, 77(8):085119, February 2008.

[24] Wolfgang Nolting. *Grundkurs Theoretische Physik 7:*. Grundkurs Theoretische Physik. Springer, 2005.

[25] Yuval Oreg, Gil Refael, and Felix von Oppen. Helical liquids and majorana bound states in quantum wires. *Physical Review Letters*, 105(17):177002, October 2010.

[26] Stellan Östlund and Stefan Rommer. Thermodynamic limit of density matrix renormalization. *Phys. Rev. Lett.*, 75:3537–3540, Nov 1995.

[27] R. G. Pereira. Charge dynamics in half-filled hubbard chains with finite on-site interaction. *Physical Review B*, 85(16), 2012.

[28] C. H. L. Quay, T. L. Hughes, J. A. Sulpizio, L. N. Pfeiffer, K. W. Baldwin, K. W. West, D. Goldhaber-Gordon, and R. de Picciotto. Observation of a one-dimensional spin-orbit gap in a quantum wire. *Nat Phys*, 6(5):336–339, May 2010.

[29] Emmanuel I. Rashba. Spin-orbit coupling and spin transport. *Physica E: Low-dimensional Systems and Nanostructures*, 34(12):31 – 35, 2006. Proceedings of the 16th International Conference on Electronic Properties of Two-Dimensional Systems (EP2DS-16).

[30] Koji Sato, Daniel Loss, and Yaroslav Tserkovnyak. Cooper-pair injection into quantum spin hall insulators. *Phys. Rev. Lett.*, 105:226401, Nov 2010.

[31] Jay D. Sau, Roman M. Lutchyn, Sumanta Tewari, and S. Das Sarma. Generic new platform for topological quantum computation using semiconductor heterostructures. *Physical Review Letters*, 104(4):040502, January 2010.

[32] Ulrich Schollwoeck. The density-matrix renormalization group in the age of matrix product states. *arXiv:1008.3477*, August 2010. Annals of Physics 326, 96 (2011).

[33] D. Schuricht, S. Andergassen, and V. Meden. Local spectral properties of luttinger liquids: scaling versus nonuniversal energy scales. *arXiv:1111.7174*, November 2011. J. Phys.: Condens. Matter 25, 014003 (2013).

[34] Dirk Schuricht. Spectral properties of one-dimensional spiral spin density wave states. arXiv e-print 1112.3045, December 2011. Phys. Rev. B 85, 121101(R) (2012).

[35] Luis Seabra and Frank Pollmann. Exotic ising dynamics in a bose-hubbard model. *Physical Review B*, 88(12), September 2013. arXiv:1303.2408 [cond-mat].

[36] E. M. Stoudenmire, Jason Alicea, Oleg A. Starykh, and Matthew P.A. Fisher. Interaction effects in topological superconducting wires supporting majorana fermions. *Physical Review B*, 84(1):014503, July 2011.

[37] P. Středa and P. Šeba. Antisymmetric spin filtering in one-dimensional electron systems with uniform spin-orbit coupling. *Physical Review Letters*, 90(25):256601, June 2003.

[38] Jarno van der Kolk. *Time evolution of matrix product operators in the Heisenberg picture*. PhD thesis, University of Munich, 2011.

[39] Guifré Vidal. Efficient classical simulation of slightly entangled quantum computations. *Phys. Rev. Lett.*, 91:147902, Oct 2003.

[40] Steven R. White. Density matrix formulation for quantum renormalization groups. *Phys. Rev. Lett.*, 69:2863–2866, Nov 1992.

[41] Steven R. White. Density-matrix algorithms for quantum renormalization groups. *Phys. Rev. B*, 48:10345–10356, Oct 1993.

[42] Steven R. White and Ian Affleck. Spectral function for the S=1 heisenberg antiferromagetic chain. *Physical Review B*, 77(13):134437, April 2008.

[43] Congjun Wu, B. Andrei Bernevig, and Shou-Cheng Zhang. Helical liquid and the edge of quantum spin hall systems. *Physical Review Letters*, 96(10):106401, March 2006.

[44] Cenke Xu and J. E. Moore. Stability of the quantum spin hall effect: Effects of interactions, disorder, and Z_2 topology. *Physical Review B*, 73(4):045322, January 2006.

[45] Valentin Zauner. Time evolution of a comoving window. Master's thesis, Graz University of Technology.

Acknowledgements

Writing a master thesis is usually not a lonely quest. Particularly, writing my own master thesis would not have been possible with the tremendous input I got from colleagues, friends and family. I want to thank these great people now in no particular order.

First of all, I would like to thank my family for always encouraging me to pursue my interests and I would also like to thank my girlfriend Alina for her support and patience with me. Then, I would like to thank my advisor Hans Gerd Evertz for his supervision and the many helpful discussions and hints I got from him. He always had time for my problems and helped me out on various occasions. Another person, which was indispensable for my master thesis and I would like to thank, is Sabine Andergassen from the University of Vienna. She helped me out on many theoretical and technical subjects and pointed out the right direction when I couldn't see it. During the many conversations and correspondence we had, some of the key elements of my master thesis arosed. Another person I am greatly indepted to is Martin Ganahl, who not only allowed me to use his source code, but also gave me endless support for it. Nearly all the numerical work done in my master thesis used Martin Ganahl's source code. The many interesting and helpful discussions we had, also contributed their fair amount to my master thesis. I would like to thank Dirk Schuricht for helpful discussions and for giving me his field theoretical calculations. Another thank you goes to Enrico Arrigoni, Markus Aichhorn and Martin Nuss, which helped me out on various subjects. Particularly, I want to thank also Andreas Hirczy for solving all of my frequent computer problems. Last but not least, I would like to thank all the other members of the institute for making my stay a pleasant and fun time.

Of course, there are a lot more names to mention here, but it would take too much space to name them all. Therefore, a collective thank you to all colleagues, friends and everyone who feels overlooked.